Coordination Chemistry Reviews 473 (2022) 214809

Contents lists available at ScienceDirect

Coordination Chemistry Reviews

journal homepage: www.elsevier.com/locate/ccr

Review

Manganese ferrite ($MnFe_2O_4$) nanostructures for cancer theranostics

Chandunika R. Kalaiselvan [a], Suvra S. Laha [b,c], Sandeep B. Somvanshi [d], Tanveer A. Tabish [e], Nanasaheb D. Thorat [f,g,*], Niroj Kumar Sahu [a,*]

[a] Centre for Nanotechnology Research, Vellore Institute of Technology, Vellore 632014, Tamil Nadu, India
[b] Department of Physics and Astronomy, Wayne State University, Detroit 48201, USA
[c] Centre for Nano Science and Engineering, Indian Institute of Science, Bangalore 560012, India
[d] Department of Materials Engineering, Purdue University, West Lafayette 47906, IN, USA
[e] Division of Cardiovascular Medicine, Radcliffe Department of Medicine, University of Oxford, Oxford OX3 7BN, United Kingdom
[f] Faculty of Engineering and Sciences, MIT Art, Design and Technology University, Pune 412201, Maharashtra, India
[g] Nuffield Department of Women's & Reproductive Health, Medical Science Division, John Radcliffe Hospital University of Oxford, United Kingdom

ARTICLE INFO

Article history:
Received 14 March 2022
Accepted 26 August 2022

Keywords:
Manganese ferrite
Superparamagnetism
Magnetic properties
Nanomedicine
In vivo studies
Cancer theranostics

ABSTRACT

Over the past decade, transition metal-based ferrite nanostructures, displaying MFe_2O_4 stoichiometry (M^{2+} cations, e.g., Mn, Co, Ni and Zn), have been devised and examined primarily owing to their promising applications in cancer nanomedicine. Among these multi-functional spinel ferrites, manganese ferrite ($MnFe_2O_4$) deserves special attention because it unveils exciting magnetic properties, high chemical stability, and excellent biocompatibility, which are crucial prerequisites for advanced biomedical applications in solving real-world clinical problems. This review addresses $MnFe_2O_4$ nanostructures, including their numerous synthesis approaches, detailed physicochemical properties, surface functionalization strategies, cytotoxicity kinetics, along with a particular emphasis on their potential applications in advanced cancer care. Herein, we discuss diverse features of $MnFe_2O_4$ nanostructures, demonstrating both spherical and anisotropic morphologies and networks as futuristic cancer theranostic agents for efficient employment in magnetic resonance imaging (MRI), magnetic hyperthermia and targeted drug delivery in a safe, targeted and cost-efficient manner. Finally, future research trends and applications of $MnFe_2O_4$ nanostructures are also recommended and examined.

Contents

* Corresponding authors at: Nuffield Department of Women's & Reproductive Health, Medical Science Division, John Radcliffe Hospital, University of Oxford, United Kingdom (N.D. Thorat) and Centre for Nanotechnology Research, Vellore Institute of Technology, Vellore, India (N. K. Sahu)
E-mail addresses: thoratnd@gmail.com (N.D. Thorat), nirojs@vit.ac.in (N.K. Sahu).

https://doi.org/10.1016/j.ccr.2022.214809
0010-8545/

1. Introduction

In the recent times, cancer has been considered as one of the leading causes of death worldwide, accounting to nearly 10 million deaths in 2020, according to a report published by World Health Organization (WHO) [1]. Therefore, it poses a severe threat to human health. It is a disease that can manifest in any part of the organ or tissue of the living system when there is an uncontrolled and abnormal cell growth with the rapid cell division [2]. Among currently available treatment interventions for the treatment of cancer, surgery is considered the most effective and widely used modality. Radiotherapy and chemotherapy are also used in combination with surgery, depending upon the type and stage of cancer. In recent years, several new strategies involving metallic, magnetic and semiconductor nanoparticles (NPs) of different sizes and shapes have been implemented to revolutionize cancer nanomedicine [3–9]. Cancer nanotechnology has played a pivotal role not only in restricting the growth of original tumor, however, it also holds the potential to eradicate malignant tissues developed elsewhere in the body *via* metastasis and are not responding to standard treatment procedures. These tiny particles, when appropriately functionalized with the most suitable biomolecules, carry the potential to migrate to specific cells and tissues in the cancer microenvironment. Because of the reduced size effect, these tiny particles display substantial surface area which primarily increases the nanoparticle-binding affinity with certain 'classic' chemotherapy drugs, ligands and antibodies, thus promoting targeted delivery and controlled release in a safe and targeted fashion [10]. Among the different classes of nanoparticles (NPs), magnetic NPs (MNPs) received considerable attention in the field of biomedical science and engineering. MNPs find extensive applications in magnetic resonance imaging (MRI) [11–15], targeted drug delivery [16–20], magnetic hyperthermia [21–23], bio magnetic separation [24–26], biosensors [27–30], and many more. As the particle size is reduced below a certain critical diameter (usually below 20–30 nm), the domain walls get shortened, and it eventually behaves as a single magnetic domain particle. When the anisotropy energy overcomes the thermal energy k_BT, superparamagnetism occurs in MNPs. Various forms of magnetic particles with different compositions have been devised and evaluated for biomedical applications to exploit their nanoscale magnetic phenomena. Changing the size, structure, composition, morphology, and surface chemistry improve the magnetic properties and significantly impact the behavior of NPs for *in vivo* applications [31].

Very recently, the transition-metal based ferrite NPs, exhibiting MFe_2O_4 (M^{2+} cations *eg.,* Mn, Co, Ni and Zn) stoichiometry, have been extensively explored for advanced biomedical applications [32]. Various ferrites materials are extensively used for chemothermal therapy of cancer and through reactive oxygen species (ROS) generation [33–37]. In this review, we will be discussing primarily about $MnFe_2O_4$ nanostructures as a potential tool for cancer theranostics. Among other cations, Mn received particular attention in the field of biomedicine due to its different oxidation states. The most common manganese valence states are Mn^{2+}, Mn^{3+} and Mn^{4+}. Among them Mn^{2+} ions show the best stability when compared with Mn^{3+} ions and Mn^{4+} ions due to its half-filled outer 3d electrons ($\sim 5\mu_B$) [38,39]. In addition, the magnetism of the NPs depends on the manganese valence states, therefore, Mn^{2+} ions with five unpaired electrons exhibit the strongest relaxivity, followed by Mn^{3+} and Mn^{4+} ions. Manganese ferrite ($MnFe_2O_4$) with Mn^{2+} valance state received significant interest in biomedical applications due to its remarkable magnetic properties and chemical stability. $MnFe_2O_4$ has been of primary interest among spinel ferrites due to its high saturation magnetization, minimal or near zero coercivity, and excellent biocompatibility, which qualifies them for biological applications (Fig. 1). $MnFe_2O_4$ exhibits a bulk saturation magnetization (M_S) of 80 emu g^{-1} close to the M_S of bulk Fe_3O_4 and γ-Fe_2O_3 ($\sim$90 emu g^{-1} and $\sim$ 80 emu g^{-1}) [40,41] and an anisotropy constant value of $K = 2.5x10^3$ J/m^3 at room temperature [42].

A spinel structure is generally denoted by the chemical formula AB_2O_4, where A and B represent the tetrahedral (surrounded by four oxygen atoms) and octahedral (surrounded by six oxygen atoms) sites. Depending upon the cationic distribution in the tetrahedral and octahedral sites, the spinel structure can be of two types: *normal* and *inverse*. $ZnFe_2O_4$ exhibits a normal spinel structure, with Zn^{2+} and Fe^{3+} occupying the tetrahedral A and octahedral B sites respectively. The classic example of a ferrite enjoying an inverse spinel geometry is Fe_3O_4. In this case, Fe^{3+} ions occupy the tetrahedral A sites, while Fe^{2+} and Fe^{3+} ions are placed in the octahedral B sites alternatively. Interestingly, $MnFe_2O_4$ exhibits a mixed spinel structure, where Mn^{2+} and Fe^{3+} ions can simultaneously occupy the A and B sites (Fig. 2) [43]. This uniqueness in the lattice geometry promotes exciting magnetic properties for advanced biomedical applications. The synthesis of $MnFe_2O_4$ NPs by different methods like coprecipitation, hydrothermal, and thermal decomposition, their structural and magnetic properties, surface functionalization strategies to improve colloidal stability, biocompatibility and biodegradability are explained in detail in the following sections. Additionally, *in vivo* studies concerning the biomedical applications of $MnFe_2O_4$ nanostructures are also carefully reviewed. A large number of reviews has already been

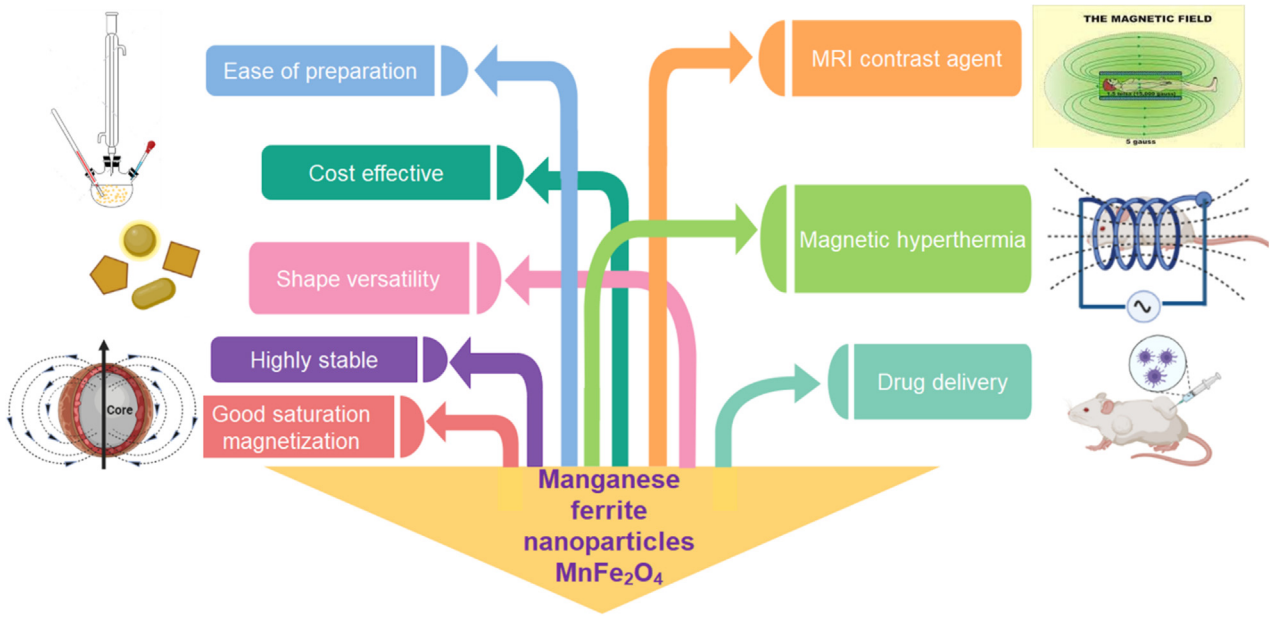

Fig. 1. Schematic illustration of the advantages of manganese ferrite nanoparticles and their potential uses in medicine.

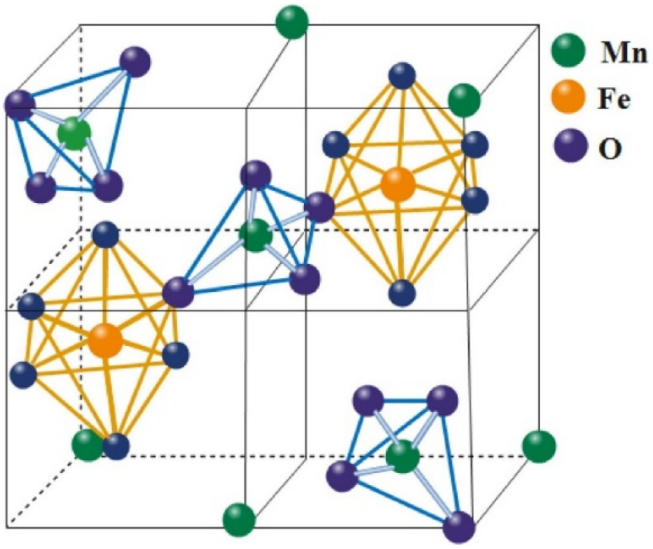

Fig. 2. Structure of manganese ferrite showing tetrahedral (Td) and octahedral (Oh) sites. Adapted and reprinted with permission from reference [52].

published on MNPs for applications in medical science and technology [16,17,44–51]. However, till date, to the best of our knowledge, there is not any detailed biomedical review available on $MnFe_2O_4$ nanostructures, which substantiates the need to review their recent findings and trends in the field of nanomedicine.

2. Synthesis of $MnFe_2O_4$ nanostructures

Over the past decades, several research papers have described the synthesis method of $MnFe_2O_4$. Different synthetic routes are capable of synthesizing $MnFe_2O_4$ NPs of various shapes, and sizes with varying stability. Such approaches used to obtain high quality $MnFe_2O_4$ for biomedical applications are co-precipitation, hydrothermal, thermal decomposition etc. Each of these synthesis methods with a reaction mechanism and a few examples is discussed in this section. The synthesis methods schematic is illustrated in (Fig. 3) and their advantages and limitation are given in Table 1.

2.1. Co-precipitation method

It is a classical method used for decades in lab-scale preparations to form precipitation from homogeneous solutions. Generally, a reducing or precipitating agent is added to the aqueous solution of the metal precursor to yield products during the reaction. It is a simple method carried out to produce a uniform-sized NP with precise control over the shape. The aqueous solution generally consists of $M_A(II)$ and $M_B(III)$ with a base at an ambient room temperature to a higher temperature. The composition, shape and size of MNPs can be modified by several factors such as the temperature of the reaction, type and ratio of precursors, volume of solution and pH of the medium [53]. The precursor salts used in general are chlorides, nitrates, perchlorates, and sulfates. The mechanism involved in the preparation of NPs by the co-precipitation method is given in Eqn. (1).

$$2M_A^{3+}(aq) + M_B^{2+}(aq) + 8OH^-(aq) \rightarrow M_AM_{B2}O_4(s) + 4\,H_2O \quad (1)$$

Recently, variable sizes of manganese iron oxide obtained by changing the pH of the solution through a co-precipitation method have been reported by Puspitasari et al. [54]. Here, the experiment was conducted by adjusting the amount of sodium hydroxide added to obtain three different pH levels of 8, 10 and 12. The morphological study of the synthesized particles showed a decrease in the particle size and magnetic properties, with an increase in the pH of the medium.

2.2. Polyol method

It is a liquid phase synthesis process carried out at high temperatures with multivalent alcohol as the solvent. It is a promising process for synthesizing NPs useful in biomedical applications as the solvent used is water-compatible, and chelation is easy. Polyols instantaneously form a coordination bond with the nucleus by providing excellent control over particle distributions and sizes [55].

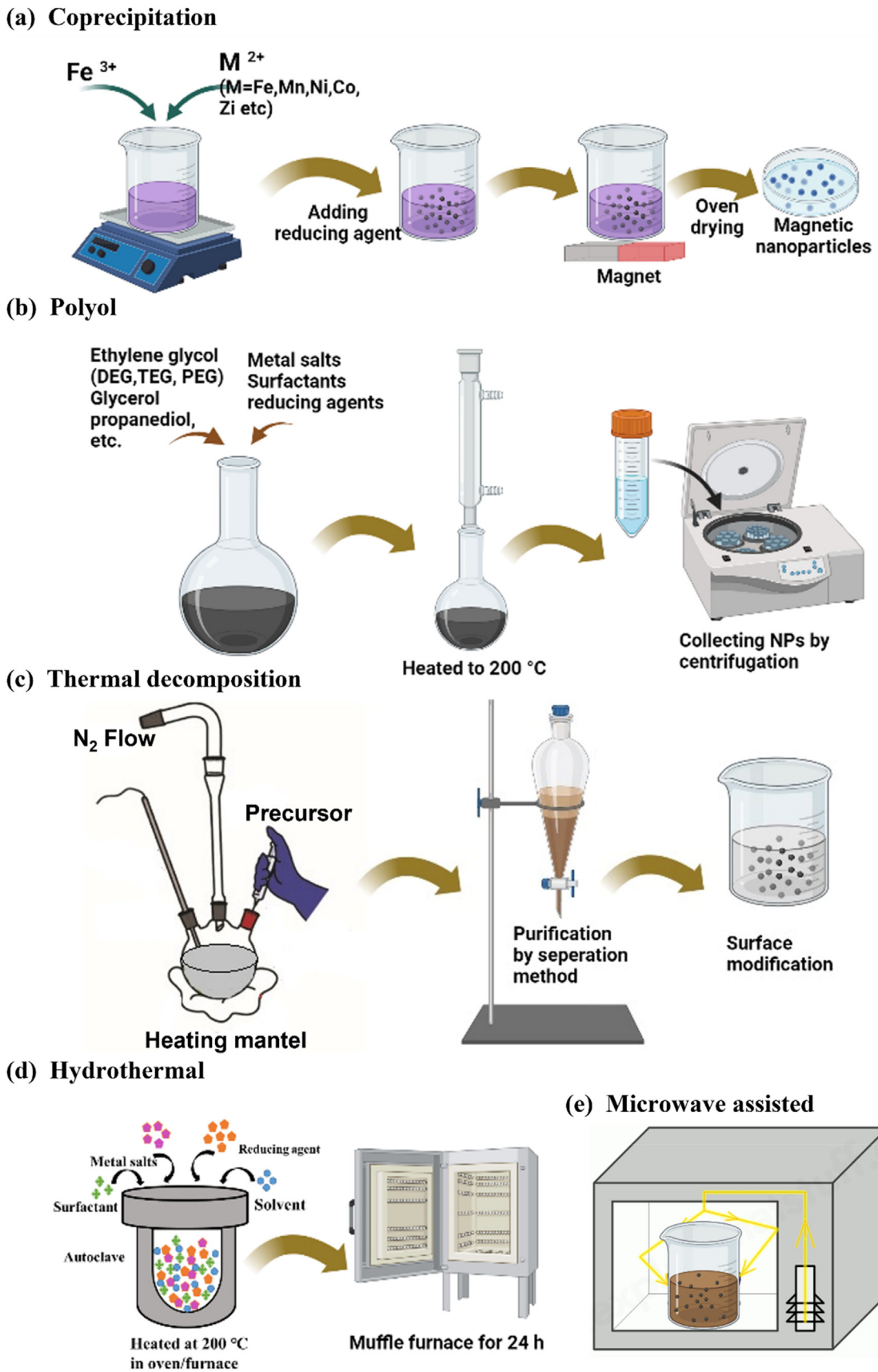

Fig. 3. Schematic representation of some of the commonly used chemical strategies to prepare NPs; a) co-precipitation, b) polyol method, c) thermal decomposition, d) hydrothermal and e) microwave assisted method.

Table 1
Advantages and limitations of aforementioned chemical synthesis methods.

Method	Advantages	Limitations
Coprecipitation	1) Preparation method is simple, facile and straightforward 2) Required processing time is in minutes and temperature is below 100 ℃ 3) High yield can be obtained	1) Prepared particles have irregular morphology 2) Broad size range (polydispersity) 3) No control over size and shape
Polyol	1) Relatively simple process 2) Process temperature is high and reaction time is in hours 3) 3) Good control over size and shape	1) Broad size distribution 2) Medium yield
Thermal decomposition	1) Very narrow size distribution of particles 2) Good control over size and shape 3) high yield and highly crystalline material can be obtained.	1) synthesis procedure is very complicated 2) Requires a high process temperature and time is from hours to days.
Hydrothermal	1) Relatively simple process 2) Process temperature is high and reaction time is in hours 3) High crystalline particles	1) Relatively broad size distribution with irregular spherical shape 2) Medium yield
Microwave	4) Ease method of synthesis 5) Fast reaction in minutes with pure product 6) High temperature within minutes and selective heating is possible	1) Expensive setup 2) Low yield

The removal of particles after the reaction is easy, which is carried out by simply washing with water several times. The main advantage of this method is the high crystallinity of the metal oxide NPs obtained which depends on the reaction temperature. Some of the polyols used are from the families of ethylene glycol (diethylene glycol, triethylene glycol up to polyethylene glycol), carbohydrates, glycerol, propanediol, butanediol and pentanediol [56]. Here, the morphology of NPs can be controlled by the concentration of precursors used and the reaction temperature. Particle size mainly depends on the solubility of the metal ions in the polyols. Chen et al. [57] synthesized spherical $MnFe_2O_4$ NPs at a large scale using the polyol method with ethylene glycol as a solvent. A wide range of particles varying in sizes from 40 to 45 nm was obtained with the influence on the reaction time, temperature and concentrations of the initial reagent. It was also shown that the magnetic properties varied with the size of the NPs. In another example, Aslibeiki et al. [58] fabricated the $MnFe_2O_4$ NPs by decomposing metal nitrates in different amounts of triethylene glycol. It was observed that by increasing the content of tri-ethylene glycol, the crystallite size decreased, and a more homogeneous size distribution was obtained.

2.3. Thermal decomposition

It is the most widely used preparation method for the large-scale synthesis of monodispersed MNPs. In general, organometallic reagents are decomposed in the presence of organic solvents with high boiling points and surfactants. Here, the metal oxide NPs are formed by a two-step process. Initially, the formation of metal hydroxide takes place, which is later oxidized to form the metal oxide. The size, shape and distribution of NPs are controlled by the reaction conditions such as the ratio of reagents used, temperature and reaction duration [59]. The most commonly used precursors are metal acetylacetonates [M(acac)n] (where M = Fe, Mn, Co, Ni etc. and 'acac' is acetylacetonate group), metal cupferronates [MxCupx] (where cup = *N*-nitrosophenylhydroxylamine), and carbonyls [60]. Zeng et al. [61] reported the synthesis of different sized cubic and polyhedron shaped $MnFe_2O_4$ NPs through this method in the presence of 1,2-hexadecanediol, oleic acid, and oleylamine. They showed that the size of the NPs could be controlled by varying the concentration of precursors, while the shape could be controlled by adjusting the amount of stabilizing agent used. Yang et al. [62] synthesized $MnFe_2O_4$ NPs by the decomposition of $Mn(acac)_2$ and $Fe(acac)_3$ to form highly crystalline NPs for MRI application.

2.4. Hydrothermal method

It is the most preferred method for synthesizing ultrafine powders of MNPs. It is one of the low-cost methods to produce MNPs at a large scale. In general, the synthesis process is carried out over higher temperatures of 125–250 °C and high pressures of 0.3–4 MPa. The NPs of appropriate size and shape can be obtained by choosing appropriate solvent, temperature, reaction time and pressure. The typical reaction will be carried out by dissolving the reagents in the solvent at the room temperature to form a clear solution. The solution will then be sealed and maintained at high temperature and pressure for several hours (8–72 h) in a Teflon lined stainless steel autoclave. Stoia et al. [63] synthesized $MnFe_2O_4$ nano powders by heating metal chlorides in an autoclave at 195 °C for 12 h. The nano powders were crystalline and superparamagnetic in nature, with a high M_S value of 51 emu g^{-1}. Recently Know et al. [64] synthesized cubic spinel $MnFe_2O_4$ NPs via a simple hydrothermal method. They also studied the morphological and crystalline properties of as-prepared NPs with respect to the reaction temperature.

Over the past decades, synthesising MNPs with controlled shape has been a major challenge. In addition, most of the anisotropic shaped NPs reported in the literature are limited to Fe_3O_4 (magnetite) particles. The primary research gap is to study $MnFe_2O_4$ NPs of different shapes to enhance their magnetic properties for biomedical applications. The NPs of different shapes are synthesized by various methods classified as physical, chemical and biological [65]. Physical methods include spray pyrolysis and laser ablation synthesis. The main advantage of physical processes is the ease in preparing particles of different structures and composition. These methods pose disadvantages in obtaining particles of controlled sizes and the requirement of expensive equipment which limit its high scale and cost-efficient production. As mentioned earlier, the chemical route encompasses various methods, with advantages of obtaining particles with controlled shape and size, monodisperse, green synthetic routes, low cost, and high phase purity. The drawbacks of chemical methods are the use of toxic and expensive chemicals, lack of precise phase control, low efficiency and reproducibility. Biosynthesis is a low-cost method with high yield and reproducibility but a very time-consuming process that includes microorganism and bacterial synthesis.

Typically, the crystal shape of NPs is thermodynamically or kinetically controlled. A thermodynamic process is related to the chemical potential of the reaction, such as temperature and supersaturation of the solution. The thermodynamic process reduces the reaction energy barrier either by reaction-limited or diffusion-

limited mechanisms. The diffusion-limited mechanism occurs at a high solution concentration in which the monomers are precipitated on the surface of the NPs only once, forming monodisperse particles. Whereas the reaction-limited mechanism occurs at low solution concentration wherein the surface reaction limits the growth and produces NPs with different shapes. The kinetic process reduces the reaction energy barrier in supersaturated regions when stable nucleation sites occur. Therefore, the final shape of the particles is affected by different parameters such as pH, solvent, temperature and the concentration of precursor.

2.5. Microwave assisted method

It has been widely used technique for its ease of preparation, high yield, enhanced reaction rates and eco-friendly reaction conditions compared to other methods. Over the years, nanomaterials were synthesised in a domestic microwave oven with no control over temperature or pressure. Research has shown this synthesis method is an attractive choice for developing nanomaterials in the last few decades, resulting in the development of microwave reactors exclusively for chemical synthesis. Microwave heating is nothing but a transfer of electromagnetic energy to thermal energy. This synthesis method enhances the quality of chemical synthesis by the microwave effect or non-thermal effect thereby resulting in the selective high heating efficiency. The microwave irradiation energy acts as internal heat source, which can heat the target compounds without heating the entire furnace or synthesis setup. This method's main advantage is that it can produce more uniform heating with less time and energy [66]. Lately, it has been postulated that the synthesis of NPs is highly sensitive to reaction conditions. This could benefit from microwave method since recent microwave ovens or reactors have enabled in situ measurement of temperature and pressure. The major problem of chemical synthesis is the poor solubility of organic reactants in aqueous media, which results in immiscible or biphasic reaction mixtures. This issue can be overcome by utilizing the microwave method [67]. The high dielectric constant solvents can absorb microwave radiation and produces heat during irradiation *via* dipole–dipole interactions with the alternating electric field generated by microwaves [68]. MNPs show well-defined magnetic properties when they are monodispersed in a size- and shape-dependent manner. The common synthesis methods are driven by properties of the solvent, viz. boiling point, and polarity rather than microwave method rely on the energy of microwaves. Hu et al. reported the synthesis of monodisperse spherical iron oxide nanoparticles with a polydispersity index of 3 % in ionic solvent using a microwave-assisted method [69].

2.6. Structural properties of $MnFe_2O_4$

Manganese ions in the iron oxide inverse spinel structure plays a significant role in modifying its structural properties. The Mn ions may occupy octahedral or tetrahedral interstitial sites of inverse spinel structure since Mn^{2+} ions radius (67 pm) is larger than iron ions (Fe^{2+} = 61 pm, Fe^{3+} = 55 pm). This results in the formation of mixed spinel structure. Yang et al. [70] synthesized $Mn_xFe_{3-x}O_4$ (x = 0 to 1.06) NP by thermal decomposition method. The XRD patterns of prepared $Mn_xFe_{3-x}O_4$ NP show peaks of inverse spinel structures (Fig. 4a). However, the left shifting in peaks were observed with the addition of Mn^{2+} ions. It is probably due to the change in structure with doping of larger radius of Mn^{2+} ions which may cause lattice distance bigger than that of pure iron oxide. High resolution transmission electron microscopy (HRTEM) analysis also confirmed this phenomenon. Fig. 4b shows the HRTEM micrographs of NPs with different Mn^{2+} doping levels. HRTEM images reveals spherical particles with good crystallinity. The measured lattice distances of NPs increased with different levels of doping. The lattice distance of $Mn_xFe_{3-x}O_4$ NPs are 0.29, 0.30 and 0.31 nm for × = 0, 0.47 and 1.06, respectively. This result indicates that the lattice distance gradually increases as manganese doping level is elevated. They also noticed the disturbance in the lattice fringes when × is larger than 0.47. This reveals that doping of Mn^{2+} in iron oxide structure significantly impacts the crystal structure and its lattice distances.

2.6.1. One-dimensional (1D) nanoparticles

1D NPs consist of nanorods, nanowires and nanotubes with at least one dimension in the nanometer range. Nanorods are few nanometers in diameter and are up to 100 nm in length. Nanotubes are nothing but hallow nanorods and nanowires with lengths larger than 100 nm. These elongated magnetic NPs have greatly interested biomedical applications due to their unique magnetic properties. Nanorods are commonly synthesized through hydrothermal reactions, which provide compositional and morphological control without requiring sophisticated processing. For example, Hou et al. [71] synthesized spinel $MnFe_2O_4$ nanorods by seed-mediated hydrothermal route for photocatalytic activity. Nanorods with 25–40 nm diameters and 300–400 nm lengths were

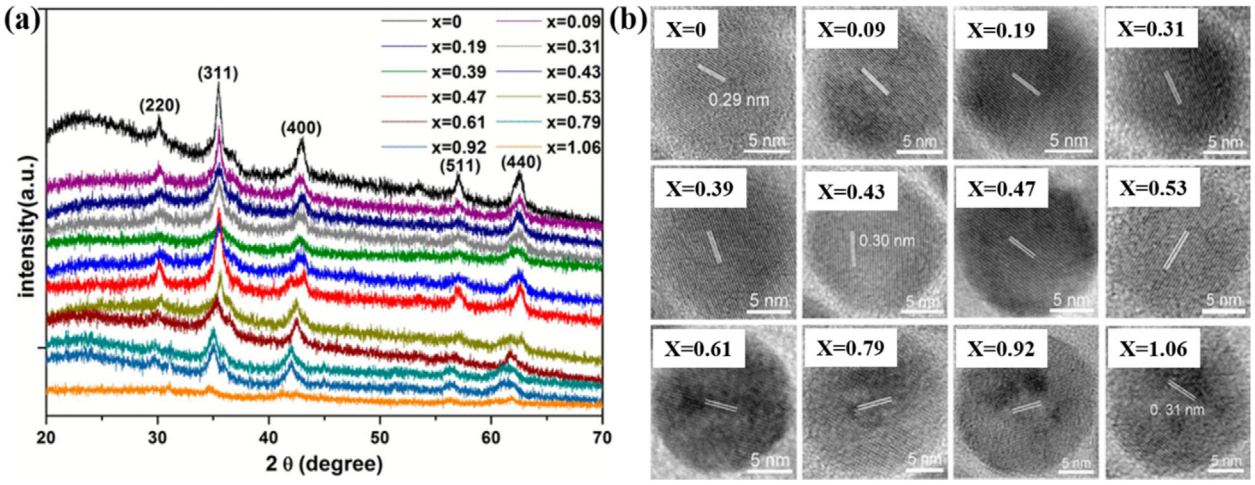

Fig. 4. (a) X-ray powder diffraction (XRD) patterns and (b) Crystal lattices in HRTEM images of $Mn_xFe_{3-x}O_4$ NPs with different Mn^{2+} doping levels. Adapted and reprinted with permission from reference [70].

obtained successfully. Initially, rod-like Mn_2O_3 was synthesized using a simple coprecipitation method, and $MnFe_2O_4$ nanorods were prepared later by the hydrothermal method with Mn_2O_3 seeds. In addition, a high saturation magnetization of 72.45 emu g^{-1} at room temperature was shown by the prepared nanorods. On the other hand, template-assisted strategies were used to synthesize nanowires and nanotubes. Cui et al. [72] fabricated $MnFe_2O_4$ and Mn-doped Fe_3O_4 porous magnetic material by thermal decomposition method. The resultant nanowires were superparamagnetic with magnetization values of greater than 45 emu g^{-1}. The prepared porous nanowires exhibited high specific surface areas and showed excellent ability to remove organic pollutants and heavy metal ions from wastewater. Different strategies have been developed recently to synthesise 1D iron oxide NPs for biomedical applications. However, research on various synthesis strategies and advantages of using ferrites like $MnFe_2O_4$ towards biomedical applications are lacking.

2.6.2. Two-dimensional (2D) nanoparticles

2D NPs consist of nano-film, plate, and sheet-like structures. In general, 2D NPs have a magnetization effect that lies parallel to the basal plane, which requires a strong magnetic field to align the magnetization out of the plane [73]. Song et al. [74] reported the synthesis of $Mn_xFe_{1-x}O$ iron-manganese nanoplates by the thermal decomposition method. They showed the relationship between magnetization and crystalline phases, which is achieved by controlling the annealing conditions. The prepared nanoplates reach a saturation magnetization of 30 emu g^{-1}. $Mn_xFe_{1-x}O$ nanoplates exhibit resistance to oxidation in the air when compared to FeO and MnO, making them suitable for biomedical applications. In another study by Vernekar et al. [75] studied the time-dependent evolution of the morphology of crystalline $MnFe_2O_4$ NPs. The nanocrystals were synthesized by a simple co-precipitation method, and the morphology evaluation was studied during the reaction at different time intervals. They showed the formation of nanowires with diameters of 30–40 nm at the first 15 min, which grew into 2D structured nanosheets with thickness of 30–40 nm over the next 30 min.

2.6.3. Three-dimensional (3D) nanoparticles

Other than spherical NPs, nanocubes and nanoflowers are some of the anisotropic 3D NPs. Oh et al. [76] synthesized thermally responsive chitosan coated $MnFe_2O_4$ nanocubes for MHT application. The nanocubes synthesized by the thermal decomposition method had a particle size of 18 nm, high M_S value, good colloidal stability, and low cytotoxicity. Ullrich and their group have recently synthesized iron-manganese-oxide core–shell nanocubes by the thermal decomposition method [77]. It was reported that the formation of cubic shape is due to the influence of surfactant on the growth of NPs in specific crystallographic directions. The core–shell structure was stable under ambient conditions against oxidation. Wang et al. [78] fabricated $MnFe_2O_4$ nanocubes through a simple chemical reaction. The synthesized nanocubes are in the size range of 500 nm with a large specific surface area of 90 m^2 g^{-1}. Despite the advancements in the synthesis of MNPs, research is still ongoing to control the shape of NPs by suitable synthesis protocol. Fig. 5 shows the various shapes of $MnFe_2O_4$ NPs obtained by different synthesis protocols.

3. Magnetic properties of $MnFe_2O_4$

3.1. Magnetic behavior of nanoparticles

MNPs are characterized into paramagnetic, diamagnetic, ferromagnetic, ferrimagnetic and antiferromagnetic particles by their response to an applied magnetic field. The materials that consist of atoms with unpaired electrons are called ferromagnetic materials. In this review, we focus on ferromagnetic materials. Upon applied magnetic field, ferromagnetic materials show spontaneous magnetization with large magnetic susceptibility. In addition to this, the magnetic moments aligned spontaneously in one direction over different regions of the material called a magnetic domain particle (Fig. 6a). When the material size is very small, the particle consisting of only one domain is called single-domain particles. In the case of ferromagnetic material, it is called a superparamagnetic particle. For detailed information on magnetic materials and magnetism types, we refer readers to the literature [81].

In general, on the magnetic field application, NPs magnetic moments align in the direction of the field, which increases the magnetization (M). The material gets magnetically saturated once all the moments are aligned with the field and exhibits saturation magnetization (M_S). When the direction of the applied magnetic

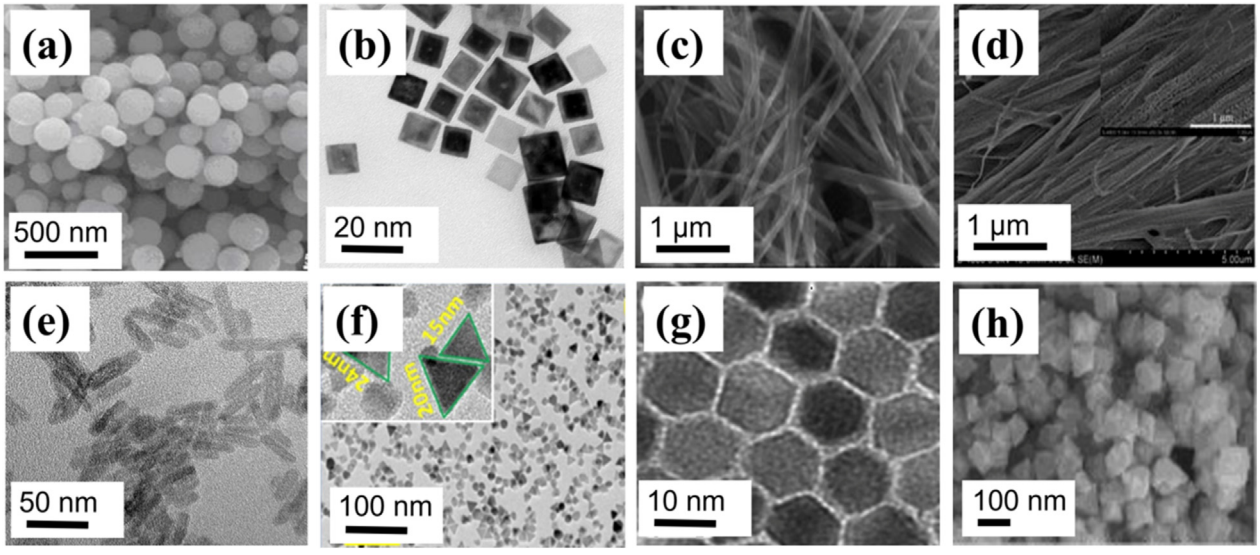

Fig. 5. FESEM and TEM images of different shapes of $MnFe_2O_4$ NP (a) nanospheres [57], (b) nanocubes [77], (c) nanorods [71], (d) nanowires [72], (e) nanorods [79], (f) triangular [80], (g) polyhedron [61] and (h) nanooctahedron [75]. Adapted and reprinted with permissions from mentioned references.

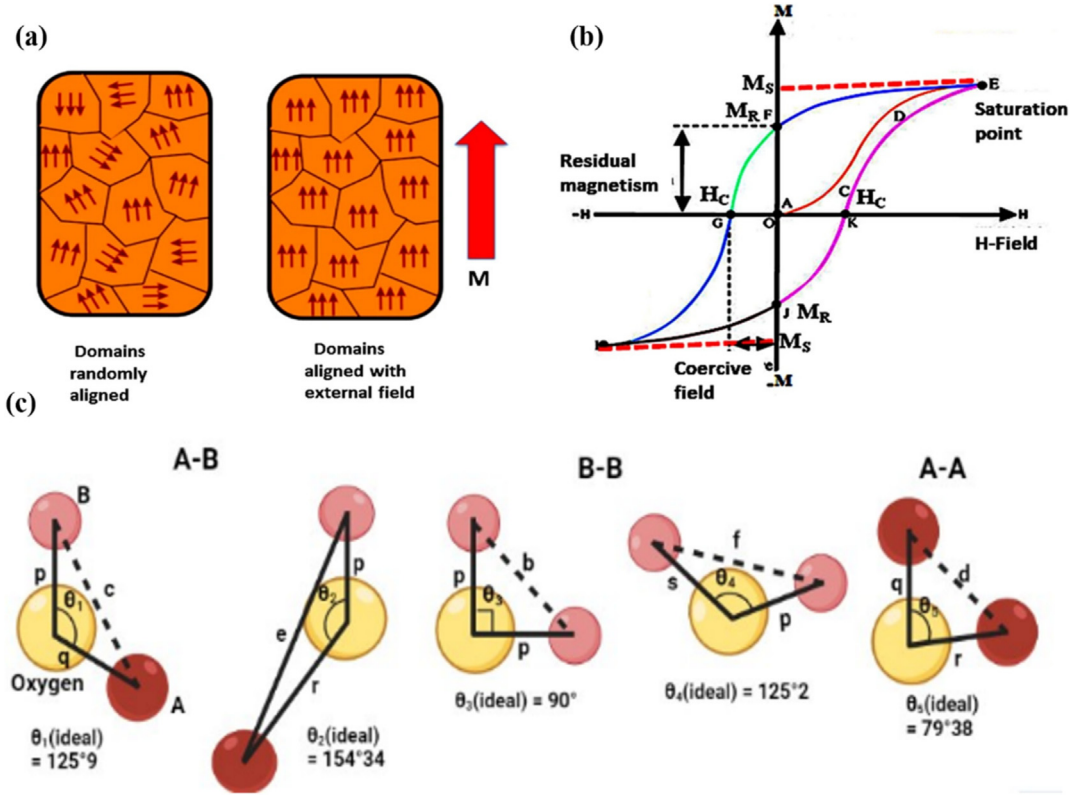

Fig. 6. (a) Magnetic domain alignment and (b) hysteresis loop of ferromagnetic material on the application of field. Adapted and reprinted with permission from reference [86], (c) magnetic interactions of the ion pairs in spinel ferrites. Figure modified and copyrighted from reference [87].

field is reversed, the magnetization starts decreasing. When the magnetic field decreases to zero, some magnetic moment alignment persists, resulting in minimal magnetization. This is referred to as the remanent magnetization (Mr). The reverse magnetic field is applied to make the M zero, and the required field is called the coercivity or coercive field (Hc) shown in Fig. 6b. With respect to coercivity, the magnetic materials are divided into soft-magnetic (low coercivity) example, spinel ferrites and hard-magnetic materials (high coercivity), typically permanent magnets. The materials basic magnetic properties are determined by the crystal structure and electronic structure of magnetic ions/atoms in the materials, which affects their M_S and magnetocrystalline anisotropy. The M_S depends on the magnitude of the magnetic moments and the distance and angle between ions. Where the magnetocrystalline anisotropy is due to the alignment of the magnetic moments along crystallographic directions. Typically, the magnetic moments in crystals align in one preferred order, the magnetic easy axis. The magnetic field required to realign the direction of magnetic moments is called the magnetocrystalline anisotropy field. Both the magnetocrystalline anisotropy field and saturation magnetization of the materials are intrinsic properties, while H_c and M_r are extrinsic properties that depend on the size and shape of the magnetic particles.

Magnetic properties like magnetization, magnetic moment and magnetocrystalline anisotropy of spinel ferrites are highly influenced by the particle's size and shape. For biomedical applications, magnetic moment m (product of magnetization and core volume V_m) is the most important factor for sensing and imaging application since the increase in m yields a more pronounced detection signal [11,82]. Magnetic properties on the surface of magnetic material differ from the interior core region due to the surface spin canting effect [83]. This effect is disturbed by the core size. In magnetic nanomaterials, increased anisotropy constant with decreased magnetization is observed compared to bulk material [84]. Kim et al. modelled saturation magnetization M_S for the spherical particle as in Eqn (2).

$$M_s = M_{sb}\left(1 - \frac{2\delta}{D}\right)^3 \quad (2)$$

Where M_{sb} is the saturation of bulk material, δ is the thickness of the spin canting layer, and D is the core diameter. The anisotropy value of the spherical particle is given by Eqn. (3) [85].

$$K_{eff} = K_b + \frac{6\Phi}{D}K_s \quad (3)$$

Where K_s and K_b are the surface and bulk anisotropy constants, $\Phi = 1$ for spherical particle. The shape anisotropy is negligible than surface anisotropy for spherical particles. And bulk magnetic material has a multi-domain state with different magnetization directions within each domain. The magnetic domains stabilize at critical diameter Dc and form a single-domain particle. The critical diameter varies between 10 and 100 nm, varying with different particle.

The magnetization will point in one direction for single-domain particle, thus having the largest possible magnetic moment $\mu = V_m$-M_S (where V_m is core volume) and the magnetization is equal to its saturation magnetization. The Stoner-Wohlfarth model well describes the hysteresis of the single-domain particle as under the influence of an external field, the magnetization rotates as one single giant magnetic moment. The magnetic moment has two orientations for single domain particle due to magnetic anisotropy. The moments are arranged antiparallel to each other along its 'easy axis' and are separated by an energy barrier of $E_b = K_{eff}$ V_m. For superparamagnetism, at a finite temperature T, Eb is comparable or smaller than k_BT (thermal fluctuation energy). The magnetic moment frequently rotates from one direction to the other,

resulting in net magnetization to zero. In the absence of an external field, superparamagnetic material shows zero magnetic moment due to the fast flipping of the moments. It shows positive magnetization in the presence of the external field. The mean time taken by the magnetic moment of superparamagnetic NPs to flips between two preferred directions is called zero-field Néel relaxation time τ_N, given by Eqn. (4).

$$\tau_N = \tau_0 \exp \frac{K_{eff} V_m}{k_b T} \tag{4}$$

Where τ_0 is attempt time 10^{-10}–10^{-9} s depending on the material, and k_B is Boltzmann constant. From the equation, the τ_N is an exponential function of the particle core size. It is the rotation of magnetic moment in stationary magnetic particles, and it can vary from nanoseconds for NPs to years for bulk materials. However, NPs, dispersed for biomedical applications, have both Néel and Brownian processes. The zero-field Brownian relaxation time is expressed as in Eqn. (5).

$$\tau_B = \frac{3\eta V_h}{k_b T} \tag{5}$$

Where V_h is the hydrodynamic volume of the MNP and η is the fluid viscosity. The effective relaxation time is given by Eqn. (6).

$$\tau = \frac{\tau_N \tau_B}{\tau_N + \tau_B} \tag{6}$$

In superparamagnetic NPs, above the blocking temperature T_B (temperature below which the magnetization relaxation is slower (Fig. 7a)), $\tau_m > \tau_N$, (where τ_m is the measured time) so the magnetic moment flips several times within the measurement period, thus, the measured magnetization M = 0 when the external field H = 0 Oe. When the external magnetic field is applied, the magnetic moments align with the field direction, resulting in a net magnetization similar to the paramagnetic behavior, which is explained by the Langevin model (Eqn. (7)).

$$M(H) = M_s L(\mu_0 \frac{\mu H}{k_b T}) \tag{7}$$

L(x) is the Langevin function, H is the applied magnetic field, and μ_0 is the magnetic permeability of a vacuum.

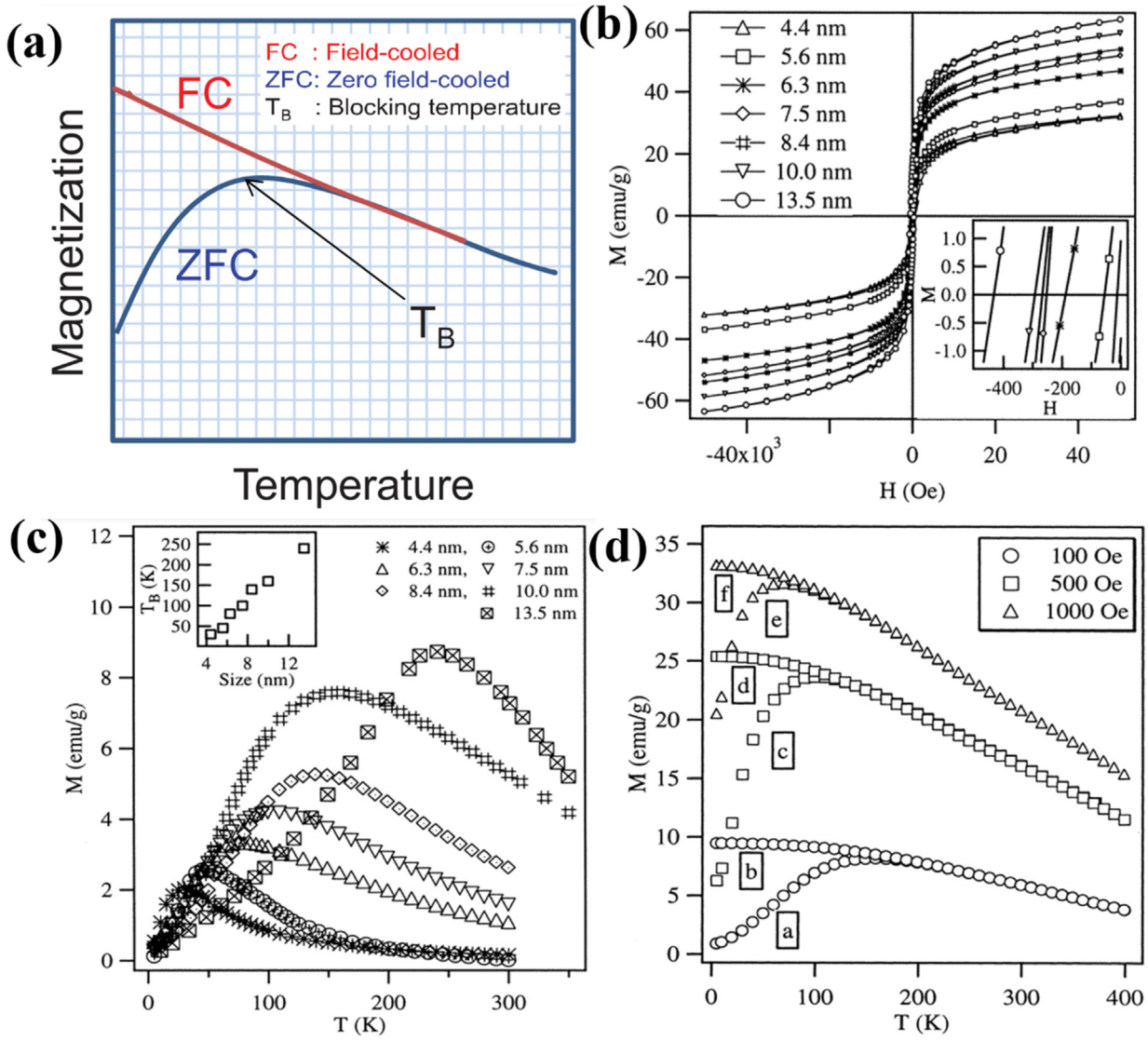

Fig. 7. (a) Schematic illustration for estimating the blocking temperature (T_B) of magnetic nanoparticles experimentally, Magnetization studies of $MnFe_2O_4$ NPs with various sizes (b) Field-dependent magnetization hysteresis and (c) Magnetization vs temperature, and (d) Temperature dependence of magnetization for zerofield- cooled (ZFC) and field-cooled (FC) 10 nm NPs under various magnetic fields. Adapted and reprinted with permission from reference [40].

3.1.1. Magnetization

The magnetization M_S in spinel ferrites is achieved by the interaction between the spins of the metallic cation in the A and B sites and oxygen ions which can be explained by the super exchange mechanism. There are three types of interactions, namely A-O-A (J_{AA}), B-O-B (J_{BB}), and A-O-B (J_{AB}), as shown in Fig. 6c [88,89]. These interactions vary with the magnitude of the anion parameter (u). The interaction strength varies from strongest to weakest in the order of $J_{AB} > J_{AA} > J_{BB}$. The dominant interaction J_{AB} between A and B sub-lattice is induced in the ferrimagnetic alignment. Table 2 shows the general formula for calculating bond distance and angle between cation and anion in the ferrite structure. In inverse spinel structures, the contribution of iron cations at A sites cancels that of at B sites, and the net moment is due to the divalent cations at B sites. In a normal spinel structure, the cation on B sites possesses the magnetic moments of an antiferromagnetic alignment. For example, $ZnFe_2O_4$, since Zn^{2+} at A sites are also non-magnetic, the net magnetization will be zero. Hence, $ZnFe_2O_4$ below the Neel temperature of 10 K acts as antiferromagnetic due to J_{BB} interaction and above 10 K acts as paramagnetic. The net magnetization of spinel ferrites is given by the average contribution of magnetic moments in the two sub-lattices. The magnetization at T = 0 can be given as in Eqn. (8). $MnFe_2O_4$ achieves the largest magnetization when compared to other materials, as shown in Table 3. This is due to the largest inversion degree and the existence of a mixed valance state of Mn ions in the $MnFe_2O_4$ NPs.

$$M_s = \frac{N.d}{M_M}\left[\sum n_{B,B} - \sum n_{B,A}\right]\mu_B = \frac{N.d}{M_M}\mu_{eff} \quad (8)$$

where N is Avogadro's number, d is density, M_M is the molar mass, $n_{B,i}$ is the number of Böhr magnetons, μ_B is associated with the i site of the unit cell.

The relationship between magnetization and size of NPs is inevitable. The size dependent saturation magnetization is the topic of interest in recent years. The magnetic property of spinel ferrite structures like $MnFe_2O_4$ several factors plays major role like cation distribution, oxidation state, chemical composition, and size of the particle. Liu and Zhang [40], studied the variation in magnetic properties of $MnFe_2O_4$ NPs in size range of 4 to 14 nm and have been prepared from reverse micelles. The magnetic studies from Fig. 7b show that magnetization increases with the size of the NPs. They also conducted temperature dependent magnetic study to find saturation magnetization of various sized NPs at the temperature range of 5 to 350 K. Initially, the NPs were cooled to 5 K and the magnetization was recorded as the temperature slowly rises (shown in Fig. 7c**).** Eventually, the magnetization reaches the maximum point at temperature, which is known as the blocking temperature T_B. We can notice the T_B temperature increases with the NPs size and $MnFe_2O_4$ NPs acts paramagnetic at the temperature above T_B. They have also recorded the magnetization of the NPs at different cooling process for 10 nm sized $MnFe_2O_4$ NP as shown in Fig. 7d**.** Initially, the NPs were cooled to the lowest measuring temperature (zero-field-cooling (ZFC)) for these measurements. After that, the magnetization is recorded under a 100 Oe field with rising temperature. At T_B temperature, the NPs reach maximum magnetization and then decrease. At the field cooling process (FC) under the same applied field of 100 Oe the magnetization is maximum at 5 K and decreases with rising temperature. They repeated the experiment with two more applied field of 500 and 1000 Oe and found the blocking temperature decreases from 170 K to 110 and 60 K, respectively. The correlation between the size of the $MnFe_2O_4$ NPs and the T_B temperature is similar to the size dependence of the magnetocrystalline anisotropy. According to the Stoner-Wohlfarth theory (Eqn. (9)),

$$E_A = KVSin^2\theta \quad (9)$$

Where E_A is the magnetocrystalline anisotropy of a single domain particle, K is the magnetocrystalline anisotropy constant, V is the volume of NPs, and θ is the angle between the magnetization direction and the easy axis.

3.1.2. Magnetocrystalline anisotropy

MNPs can exhibit different anisotropy in which the magnetocrystalline is the most common anisotropy and the only intrinsic anisotropy, while others are induced. It is the material's property for spontaneous alignment of magnetization in crystallographic direction (easy direction) [91]. For closed packed spinel ferrites except for $CoFe_2O_4$, the magnetization axis direction is (1 1 1). Magnetizing spinel ferrites in this direction is easy with the minimum magnetic anisotropy energy. The energy difference present between the easy and hard direction of alignment of domains is called magnetocrystalline anisotropy energy. It is the energy needed to rotate the moment from an easy to hard direction. The magnetocrystalline anisotropy depends on the crystal structure of the material. Generally, the anisotropy of spin-orbital coupling and the orbital angular momentum is due to the magnetic moment and crystal field [92]. In a crystal lattice, each atomic moment is under the influence of a crystal field. Crystal field is each ion in the crystalline material that produces an external field by surrounding spins. When this crystal field tries to reorient the spin of an electron, the orbit of that electron also reorients due to spin-orbital coupling. The crystal lattice resists the orbit's reorientation since the crystal lattice and orbit are strongly coupled. Thus the crystal field and the spin–orbit coupling together give rise to magnetocrystalline anisotropy [93]. Due to 3d electron arrangements, the anisotropy in spinel ferrite is due to both the spin-orbital coupling and angular momentum. A simple model can give the anisotropy energy density of spinel ferrites as Eqn. (10) indi-

Table 2
The general formula to calculate the bond distance between cations and anion and the bond angles between them [90].

Bond distance		Bond angle θ
M–O	M–M	
p = a (5/8 – u)	b = √2 (a/4)	$\theta_1 = Cos^{-1}\left(\frac{p^2+q^2-c^2}{2pq}\right)$
q = a√3 (u – ¼)	c = √11 (a/8)	$\theta_2 = Cos^{-1}\left(\frac{p^2+r^2-e^2}{2pr}\right)$
r = a√11 (u – ¼)	d = √3 (a/4)	$\theta_3 = Cos^{-1}\left(\frac{2p^2-b^2}{2p^2}\right)$
s = a√3 (u/3 + 1/8)	e = √3 (3a/8)	$\theta_4 = Cos^{-1}\left(\frac{p^2+s^2-f^2}{2ps}\right)$
	f = √6 (a/4)	$\theta_5 = Cos^{-1}\left(\frac{r^2+q^2-d^2}{2rq}\right)$

Table 3
Main structural and magnetic features of a few bulk ferrite materials [92].

Ferrite	a (nm)	x	d (g cm^{-3})	μ_{eff}	K	Ms at 0 K (kA m^{-1})
$MnFe_2O_4$	0.851	0.2	4.96	4.6	0.3	552
$CoFe_2O_4$	0.839	0.8	5.27	3.7	20	464
$NiFe_2O_4$	0.833	1	5.37	2.3	0.62	294
$ZnFe_2O_4$	0.844	0	5.32			

cates, where K is the anisotropy constant of Fe^{3+} and M^{2+} in A and B sites [94].

$$K = (1-j)K^{A}_{M^{2+}} + jK^{A}_{Fe^{3+}} + jK^{B}_{M^{2+}} + (2-j)K^{B}_{Fe^{3+}} \quad (10)$$

Where 'a' is the lattice parameter, x is the inversion degree, d is the density, μ_{eff} is the effective magnetic moment, K is the anisotropy constant, and M_S is magnetization.

3.1.3. Magnetic behavior of anisotropic nanoparticles

The magnetic behavior of anisotropic magnetic NPs is due to an interplay between the shape anisotropy and the magnetocrystalline anisotropy. For soft-magnetic materials, magnetic behavior shape anisotropy plays an important role. For example, spherical MNPs can be magnetized in any direction, while in anisotropic shaped NPs, it is easy to magnetize along its long axis than its short axis as the demagnetizing field (Hd) along the short axis is larger (Eqn. (11)) [95].

$$H_d = -N_d M \quad (11)$$

Where, Nd is a demagnetizing factor, which is direction and shape dependent. For spherical particle Nd is1/3 in all directions. Whereas for 1D particle demagnetizing factor along its diameter (a) is Na = 1/2 and along its length (c) is Nc = $[\ln(2z)-1]/z^2$, where z = c/a. For 2D particle like nanoplates, demagnetizing factor along diameter(c) is Nc = $\pi/4z$ and along thickness(a) is Na = $1-\pi/2z + 1/z^2$, where z = c/a [73].

The magnetic behavior of 1D particles is similar to the bar magnet, in which magnetization is parallel to the particle surface along its length[96,97]. The shape anisotropy of the MNPs determines the magnetization's direction along their long axis and the demagnetization factor. In this case, the demagnetization factor increases with shape anisotropy which depends on a size aspect ratio. For 1D NPs, a magnetic field is applied parallel to the long axis, square-like hysteresis loop with large H_c and $M_S = M_r$ is observed. When the field applied is perpendicular to the long axis, S-like response with $H_c = 0$ and $M_r \ll M_S$ is observed. However, shape anisotropy dominates the effective magnetization in 1D NPs. Magnetization in 1D NPs is also affected by magnetocrystalline anisotropy. In the case of 2D soft-magnetic material, the magnetization of the NPs lies within the basal plane. The magnetic moments can be realigned easily in the basal plane, while a strong magnetic field is required to realign the moments that are present out of the plane. 2D particles have a strong uniaxial magnetocrystalline anisotropy with an easy axis perpendicular to the basal plane. The 2D particles behave exactly opposite to the 1D NPs. They exhibit square-like hysteresis when the applied field is perpendicular to the basal plane. The hysteresis decreases to Hc and Mr = 0 when the magnetic field is in the direction of plane [98].

3.2. Factors influencing the magnetic properties of spinel ferrite

3.2.1. Size effect

The size and shape of the NPs greatly influence the magnetic properties such as M and H_c and the stability of the spinel ferrites. The M_S depends solely on the size of the NP, where T_B and coercivity rely on the shape and size of the NPs [99]. The critical size of various spinel ferrite NPs for the transition from multi-domain to single domain was provided in detail for different NPs in the review by Krishnan et al. [100]. Some spinel ferrite exhibits different superparamagnetic properties even at different size levels below the critical size. For example, $MnFe_2O_4$ NP of various sizes 6, 7.5 and 9 nm exhibit magnetization of 50, 60 and 72 emu g^{-1}, respectively [101]. NPs have an increased number of surface ions as the size decreases with higher surface energy. The surface energy decreases the coordination between surface ions and hinders the spin alignment, decreasing M_S and coercivity [11,102]. The differences in size also significantly impact magnetic anisotropy constant, toxicity, and other spinel ferrite properties, which are the major factors for biomedical applications [103,104].

3.2.2. Coating

For biomedical applications, the coating is necessary for certain reasons like avoiding agglomeration, improving stability, reducing degradation or leaching of metal ions and toxicity [105,106]. On the other hand, coating and hydrodynamic size can affect the magnetic moment and decreases the M_S value of NPs than their bare counterparts [107]. For example, different weight % of 0.3, 0.6, 09 and 1.2 chitosan-coated $MnFe_2O_4$ with the hydrodynamic sizes of 94.4, 98.2, 104.2 and 96.8 nm shows M_S value of 40.2, 39.8, 31.2 and 36.7 emu g^{-1}, respectively [108]. In another study, the bare $MnFe_2O_4$ and PEG-coated $MnFe_2O_4$ exhibited a M_S value of 68 and 60 emu g^{-1}, respectively [109]. In the study reported by Aslibeiki et al., different volumes of triethylene glycol coating such as 0, 5, 10, 15, 20 and 30 mL were used in the synthesis of $MnFe_2O_4$ NPs, which showed magnetization of 20, 62, 91, 76, 82 and 81 emu g^{-1}, respectively [58]. Due to the coating that is present on NPs, there is a decrease in magnetization and magnetic moment, which can be explained by spin pinning. Thus, the surface coating quenches the magnetic influence of the spins on the surface of magnetic NPs [110].

3.2.3. Chemical composition

The chemical compositions, distribution, and type of the cations in A and B sites determine the magnetic properties of spinel ferrites. As discussed earlier, MNPs are particularly suitable for biological applications because of their magnetic property and low toxicity, among other characteristics. These properties strongly depend on their physicochemical characteristics, but shape and size are the most influential factors [111]. In this regime, the magnetic behavior of MNPs is controlled by the type and ratio of the distribution of cations, which is of great interest in many of their potential applications. In this sense, replacing some iron elements in iron oxide structure with other metallic elements such as cobalt, manganese, nickel, or zinc leads to change in their magnetic behavior, particularly to the effective magnetic saturation and magnetic anisotropy of the NPs [112]. For example, in the study conducted by Lee et al. [113], 12 nm sized Fe_3O_4, $MnFe_2O_4$, $CoFe_2O_4$ and $NiFe_2O_4$ show the magnetization of 101, 110, 99 and 85 emu g^{-1} with the magnetic moment of 4, 5, 3 and 2 μ_B, respectively. Another study reported by Taboada et al. [114], reveals the synthesis of spherical shape ~ 9 nm diameter sized MNPs doped with Mn, Co, and Zn under different ratios, concentrations, and combinations. All the obtained MNPs show superparamagnetic behavior at room temperature with saturation values in the range of 68 to 109 emu g^{-1}. The level of doping also plays major role in NPs magnetic characters with the behavioral changes in their hysteresis loops. For instance, Xabier et al. [115] showed the influence of ratio of Mn doping on the iron oxide NP structure as a vital factor to tune many of its magnetic characters. The prepared NPs are in the size range of 9 to 15 nm, with the high magnetic saturation values in the range of 72 to 83 emu g^{-1}.

4. Functionalization and phase transfer strategies

The functionalization or phase transfer techniques are crucial for magnetic NPs to be utilized in biomedical applications. The stability of NPs at a high concentration of salts and proteins is the most vital factor in the biological environment. As discussed earlier, MNPs synthesized by different approaches will have different surface properties like hydrophobic or hydrophilic. In general, the

interactions of MNPs depend on the surrounding media and the presence or absence of the surface molecules. MNPs tend to form clusters due to van der Waals forces and magnetic attraction between the particles. MNPs are also highly reactive under acidic environment, thereby leading to leaching [116]. Another factor is surface to volume ratio; the reduction in particle size results in high surface energy, causing aggregation of particles. Moreover, the uncoated magnetic NPs in the suspension quickly get oxidized and lose their magnetic properties.

Functionalization is required for MNPs even if they are formed in the presence of a stabilizing agent to improve their stability and specific targeting. The functionalization strategies depend on the application and initial surface chemistry of the NPs. The main aim is to achieve hydrophilic NPs with high stability in the broad range of ionic strengths and pH. For biomedical applications, the main challenge is to maintain the particle size below 100 nm after functionalization to retain its magnetic property. A proper functionalization can stabilize the NPs by avoiding agglomeration and by providing improved specific interactions. The steric hindrance of coating affects the cellular uptake and circulation time, thereby preventing the release of core materials in the biological environment causing toxicity [117,118]. For coating, polymers with a functional group (R–COOH) or (R–NH2) are generally used. The most common coatings used are lipids, proteins, dextran, chitosan, polyethylene glycol (PEG), poly(vinylpyrrolidone) (PVP), poly (lactic-*co*-glycolic acid) (PLGA), or poly(vinylalcohol) (PVA), poly(acrylic acid) (PAA), carbon, silica, metals and metal oxides. The different approaches used for surface coating are encapsulation method or grafting by using organic and inorganic molecules during (in-situ) or after (ex-situ) the synthesis process [119]. This section briefly discusses the common surface coatings used in biomedical applications.

Over the past several years, polymers have gained much attention as coating materials due to their unique properties like biodegradability, biocompatibility and amphiphilicity. They are ideal for preventing oxidation which could also be relevant to biomedical applications [120]. The two major classifications are synthetic polymers such as PEG, PVP, PVA, PLGA, PAA etc., and biopolymers such as dextran, chitosan, polylactic/polyamine acids, polysaccharides, starch, proteins, albumin, liposomes, and nucleic acids. Moreover, the polymers have functional groups such as amines, carboxylic acid, thiols etc., for conjugation. The commonly used polymers in biomedical applications and their advantages are given in Table 4. Natural polymers (biopolymers) pose milder formulation, they are biocompatible and can be used in biomedical applications. Some of the commercially available drugs are coated with natural polymers; for example, commercial MRI agents like Ferrumoxtran-10 and Feraheme are coated with carbohydrate polymers [121]. To overcome magnetic dipole–dipole interaction and to improve stability, natural polymers like dextran and chitosan are used. Among the natural polymers, dextran is the most widely used due to its good aqueous dispersion, biocompatibility and biodegradability [122]. For the past decade, dextran-coated particles have been used as MRI contrast agents [123], and chitosan-coated iron oxides are used for targeted photodynamic therapy [124,125].

On the other hand, synthetic polymers provide long blood circulation as compared to natural polymers and give better control over drug release. The degradation of synthetic polymers depends on composition, chemical structure, molecular weight, physical characteristics (shape, size, defects) and administration route [127]. The degradation rate must be considered in *in vivo* application for controlled release. PEG is a widely used synthetic polymer in biomedical applications due to its biocompatibility and prolonged blood circulation time. Polymers bind to the surface of MNPs in many ways, as shown in Fig. 8. Fig. 8a shows the direct attachment of the polymer onto the surface of the particle during synthesis through its end group. Fig. 8b indicates polymer grafting onto the coating of synthesized NPs. The use of a di-block copolymer where one block consists of a grafting group which binds to the surface of the particle is depicted in Fig. 8c. Fig. 8d indicates the wrapping of a polymer containing grafting groups around the core. The electrostatic interactions between coatings with opposite charges, where either one or both of the electrostatic forces come from a polymer, is shown in Fig. 8e. Fig. 8f indicates a micelle approach using an amphiphilic polymer containing hydrophilic and hydrophobic sections, where multiple hydrophobic cores are stabilized through hydrophobic interactions, thus making them stable in water [126]. Properties of polymers such as charge, molecular weight, stability and branching highly impact the particle's properties and their possible applications.

5. Biomedical applications of $MnFe_2O_4$ nanostructures

A major drawback of using NPs in clinical settings is their difficulty in reaching intracranial positions. Such a challenge can be overcome by using an external magnetic field to deliver MNPs to the targeted region. The biomedical applications of $MnFe_2O_4$ rely on the biocompatibility and toxicity of the NPs. The final size of

Table 4
Different polymers used as a coating material and its advantages.

Polymer	Advantages	Ref
Dextran	Biocompatibility and biodegradability, Enhances blood circulation time, better polar interaction with surfaces.	[128]
Chitosan	High biocompatibility, Polycationic hydrophilic polymer has two hydroxyl and one amino functional group, antibacterial property, potential use in non-viral gene delivery system due to its enhanced ability to react with biomolecules such as DNA.	[129–131]
Starch	Biocompatible, good for targeted drug delivery and MRI due to the ability to be transported in the extracellular spaces and internalized in nerve cells.	[132]
Polyethylene glycol (PEG)	Hydrophilic and easy to functionalize, improves blood circulation time, biodegradability and biocompatible, protein repellent, increased internalization efficiency.	[109,133–136]
Polyvinylpyrrolidone (PVP)	Improves stability of the particle by preventing coagulation, Biocompatible and biodegradable, provides monodisperse particles	[137,138]
Polyacrylic acids (PAA)	Increase biocompatibility and stability of NPs, helps in bio adhesion, used for imaging and therapy studies *in vivo*.	[139,140]
Polyvinyl alcohol (PVA)	Used for controlling particle growth, highly stable and prevents agglomeration, excellent hydrophilic emulsifier, non-toxic.	[141]
Poly (lactic-*co*-glycolic acid) (PLGA)	Improves interaction with biological materials and increases blood circulation time, biocompatibility, and biodegradability, protects drug from degrading, approved by FDA and European Medicine Agency, used for drug delivery system.	[142]

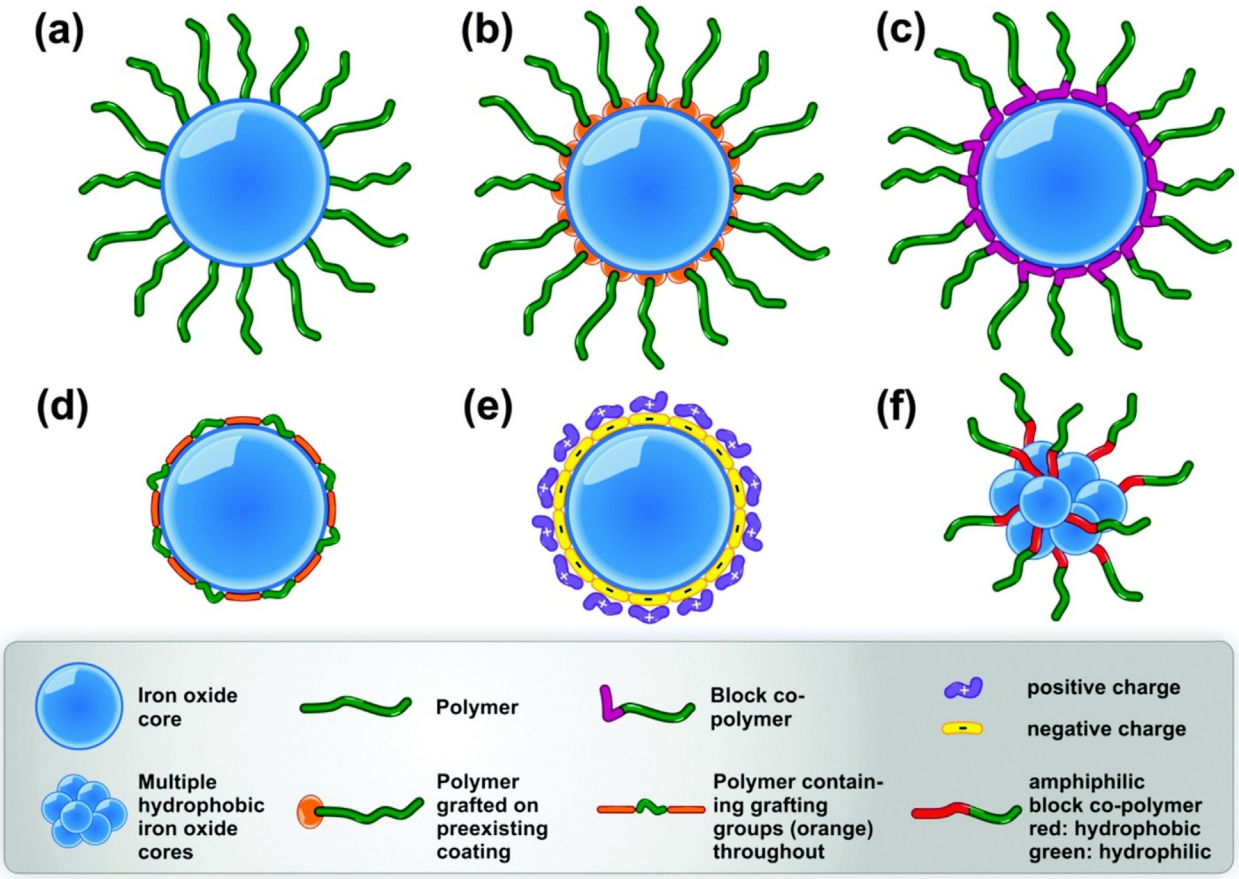

Fig. 8. Various polymer stabilization methods on MNPs. Adapted and reprinted with permission from reference [126].

the NPs, including the coating and magnetic response of the NPs, are the significant parameters that influence the biocompatibility and toxicity of the NPs. For biomedical applications in *in vivo* and *in vitro*, the $MnFe_2O_4$ NPs should have high magnetization, low toxicity, biodegradability, and long blood retention time.

5.1. Toxicity impacts

Before using magnetic particles in an *in vivo* study, toxicity evaluation in cell cultures/blood components must be investigated. Different types of cytotoxicity tests include MTT assay, Alamar Blue and Trypan blue exclusion assay. These assays lack standard protocols; hence, the higher the number of tests performed, the safer is the material for *in vivo* studies. The MTT (3-[4,5-dimethylthiazol-2-yl]-2,5 diphenyl tetrazolium bromide) colorimetric assay is the classical, inexpensive, and most used assay for cytotoxicity studies [143]. Other studies like Alamar Blue test, in which the cells are incubated with the blue non-fluorescent dye resazurin to find the number of viable cells [144]. The trypan blue dye assay is an exclusion test in which trypan solution is used to quantify dead cells. Another widely used assay is the reactive oxygen species (ROS) production test to evaluate the cytotoxicity of magnetic particles. This test is specifically designed to detect and quantify ROS generation as an indicator of cellular oxidative stress. When the cells are incubated with the material, free radicals and enzymes like superoxide dismutase and glutathione peroxidase are involved in the detoxification mechanism. This is the primary reason for induced toxicity. And the overproduction of ROS leads to DNA strand breakdown, lipid peroxidation, alteration in gene transcription and generation of protein radicals [145]. Different techniques are used to measure the number of apoptotic cells, like light microscopy (Trypan blue staining) and fluorescence microscopy (acridine orange/propidium iodide staining). Recently Lacovita et al. [146] investigated manganese ferrite and zinc ferrite nanoparticles for magnetic hyperthermia and studied their toxicity level in four different cell lines. They performed MTT assay in three different cancer cell lines a human melanoma cell line (MW35), a mouse melanoma cell line (B16F10), and a human lung adenocarcinoma (A549) cell line and one normal cell line human retinal pigment epithelial (D407) cells shown in Fig. 9a, b**.** The results show with the increase of the material concentration the viability of the cells decreases although $MnFe_2O_4$ NPs exhibited a negligible decrease with cell viability percentage of 98 to 91 % up to 0.1 mg mL^{-1} concentration and 79 % at 0.2 mg mL^{-1} concentration. Whereas $ZnFe_2O_4$ NPs show 91–73 % of the cellular viability up to 0.1 mg mL^{-1} and almost 50 % decrease at 0.2 mg mL^{-1} concentration. And also from another recent study by Islam et al. [147] it has been proven that positive surface charge also results in ROS generation. In this study chitosan coated $MnFe_2O_4$ NPs with sizes below 20 nm induces negligible toxicity effects of only less than 15 % decrease on cell viability on HeLa cells at 2 mg mL^{-1} concentration. The study by Zhang et al. [148] shows the cytotoxic evolution of manganese doped iron oxide NPs on RAW264.7 cells. The results show a decrease in cell viability percentage with an increase in NP concentration after 24 h of incubation. At 0.3 mg mL^{-1} the cell viability percentage is greater than 80 % and with the increase in concentration of 1.8 mg mL^{-1} the viability percentage is 60 % and by doubling the incubation time also show similar results.

In some of our previous studies [79,149], cytotoxicity studies of $MnFe_2O_4$ NPs were carried out using MTT assay on human breast

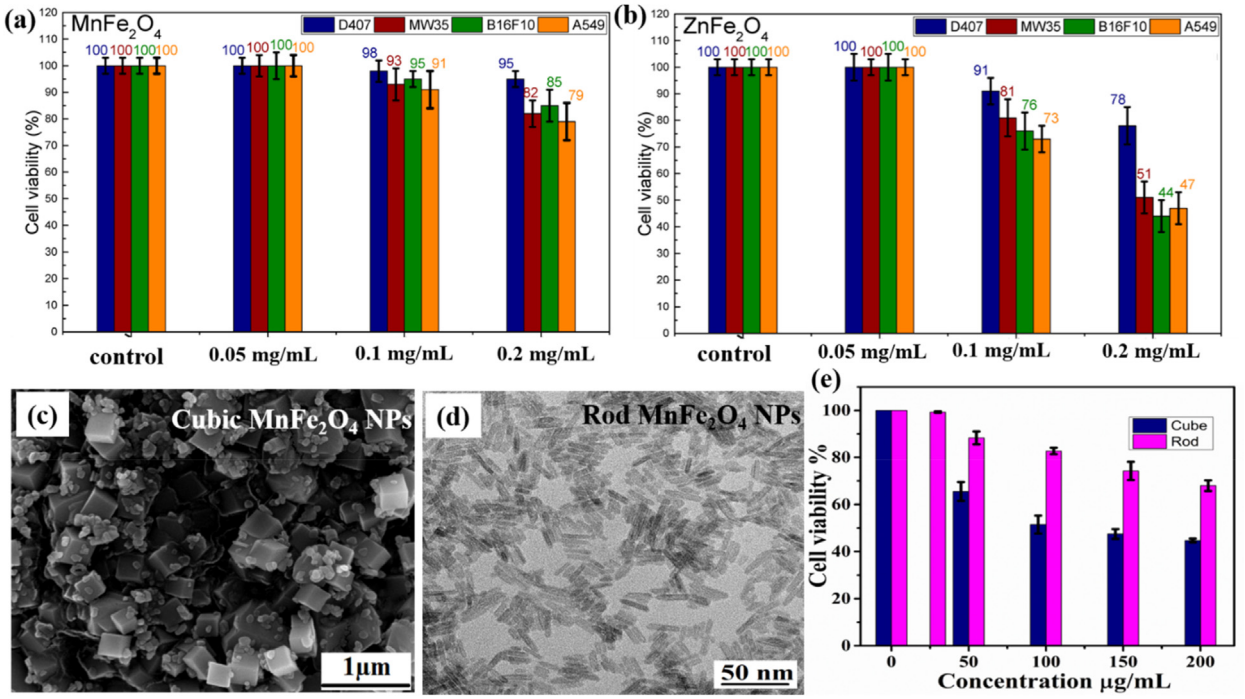

Fig. 9. Cell viability at four different cell lines at three different concentrations (a) $MnFe_2O_4$ and $ZnFe_2O_4$ NPs [146]. Cell viability profiles of cube and rod shaped $MnFe_2O_4$ NPs (c) FESEM of cubic particle, (d) TEM of rod shaped NPs and (e) cell viability percentage after treating with different concentrations NPs in MCF-7 cell lines [79,149]. Adapted and reprinted with permission.

cancer cell lines (MCF-7). The NPs showed a significant decrease in cell viability when treated with MCF-7. The cell death may be due to the reactive oxygen species (ROS) generation by $MnFe_2O_4$, which are very toxic to the cancer cells and can be explained as follows: in acidic cancer cell pH ($\sim 4-5$), $MnFe_2O_4$ may disintegrate into Mn^{2+}, Fe^{2+}, and Fe^{3+} ions. The resulting leached Mn^{2+} ions play a prime role in the generation of ROS by dissociating H_2O_2 present in the mitochondria into hydroperoxyl (HOO•) and hydroxyl (HO•) radicals through Fenton's reaction [79,150]. The possible mechanism is outlined below.

$$Mn^{2+} + H_2O_2 \rightarrow Mn^{3+} + HO^{\cdot} + OH^{-} \quad (12)$$

$$H_2O_2 + HO^{\cdot} \rightarrow H_2O + HOO^{\cdot} \quad (13)$$

$$Mn^{3+} + HOO^{\cdot} \rightarrow Mn^{2+} + H^{+} + O_2 \quad (14)$$

Similar behavior was found in earlier research as well [3,80,151]. Another reason can be due to ferroptosis which is iron depended cell death caused by lipid peroxidation. The Fe^{2+} or Fe^{3+} ion release from $MnFe_2O_4$ in the tumor site is more pronounced than at normal tissue. Released iron can participate in the Fenton reaction and induce ferroptosis of tumor cell. Cubic particles possess a relatively higher cytotoxicity effect than rod shape shown in Fig. 9d, c and e, which may be due to the irregular shape and sharp edges seen from the micrographs of the NPs.

5.2. Imaging and diagnostic applications

In the last decades, the use of MNPs in diagnosing the early stage of cancer set up a major improvement in cancer nanotheranostics. The MNPs have been selected for their high surface area, unique magnetic properties, and, most importantly, chemical modification to improve the imaging sensitivity [152]. The imaging of the tumor is the primary step in cancer therapy for locating the site and extent of its spread to decide the method of eradication or drug dosage. MRI is the most widely used technique for detecting the early stage of the tumor and tracking the drug's response. MRI works based on the principle of nuclear magnetic resonance (NMR) and can generate high-quality human body images. MNPs are widely used as a contrast agent in clinical oncological imaging due to their unique superparamagnetic properties. The contrast agent can cause significant susceptibility effects upon the application of an external magnetic field resulting in two types of relaxation processes viz., T_2 (spin–spin relaxation process), T_2* contrast and T_1 (spin–lattice relaxation process). The relaxation process is the interaction between the magnetic core of the NP and the surrounding water molecules. Hence, MRI contrast agents are divided into two types: positive and negative. Positive contrast agents provide brighter images due to T_1 shortening in the surrounding protons. Negative contrast agents provide darker images by shortening the T_2 relaxation of the surrounding protons. The magnetic property and the structural features of MNPs play a major role in the relaxation mechanism [153,154]. To interpret the interactions between the NPs and water molecules for the design of MRI contrast agents, the Solomon–Bloembergen–Morgan (SBM) and the outer-sphere diffusion theories were developed [155]. In the SBM theory, water proton and NP interaction are classified into an inner sphere and outer-sphere mechanism. The inner sphere mechanism involves the coordination of water protons with paramagnetic ions of NPs, whereas the outer-sphere mechanism involves the water protons that are not directly in contact with the NP centers as shown in Fig. 10. For the relaxation mechanism of weakly magnetized particles, the outer-sphere diffusion theory is used.

In general, $MnFe_2O_4$ NPs are used as T_1-positive agents or T_2-negative agents. Clinically Gd complexes are used as T_1 agents. Recently, Mn based agents similar to Gd molecular structures like

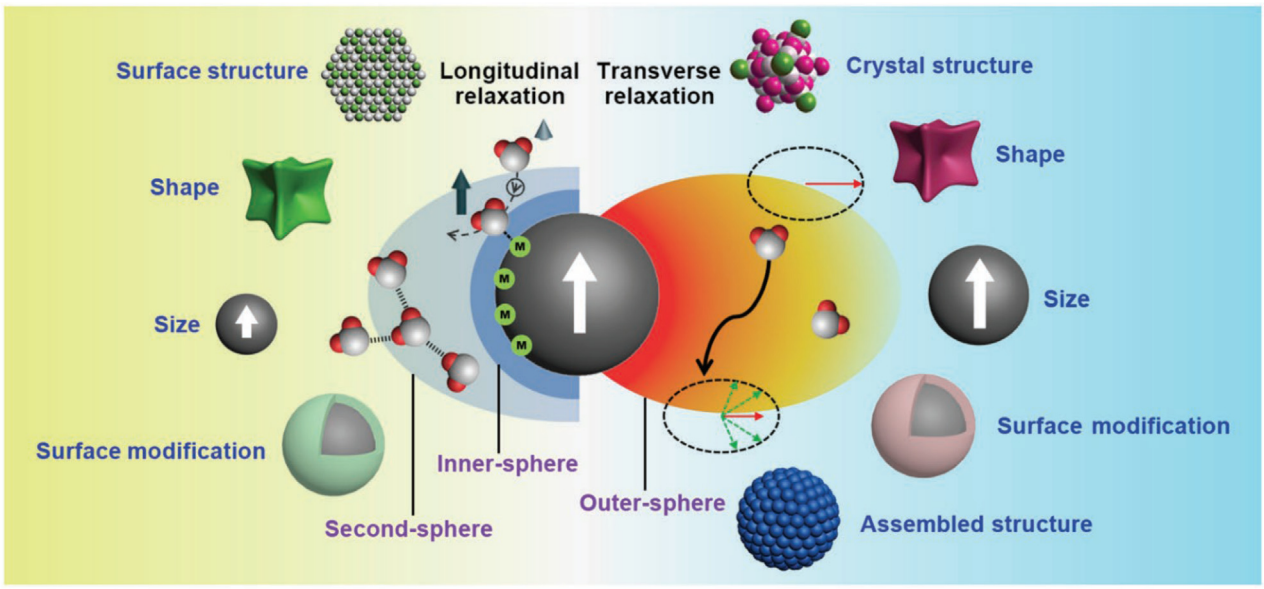

Fig. 10. Schematic of water molecule interaction with MNPs and the factor influencing the relaxation process. The inner-sphere and second-sphere mechanisms illustrate direct hydrogen bonding of water molecules with NPs, which mainly correlate with the longitudinal relaxation T_1. The outer-sphere mechanism describes diffusion and dephasing of water molecules, corresponding to the transverse relaxation T_2. Adapted and reprinted with permission from reference [155].

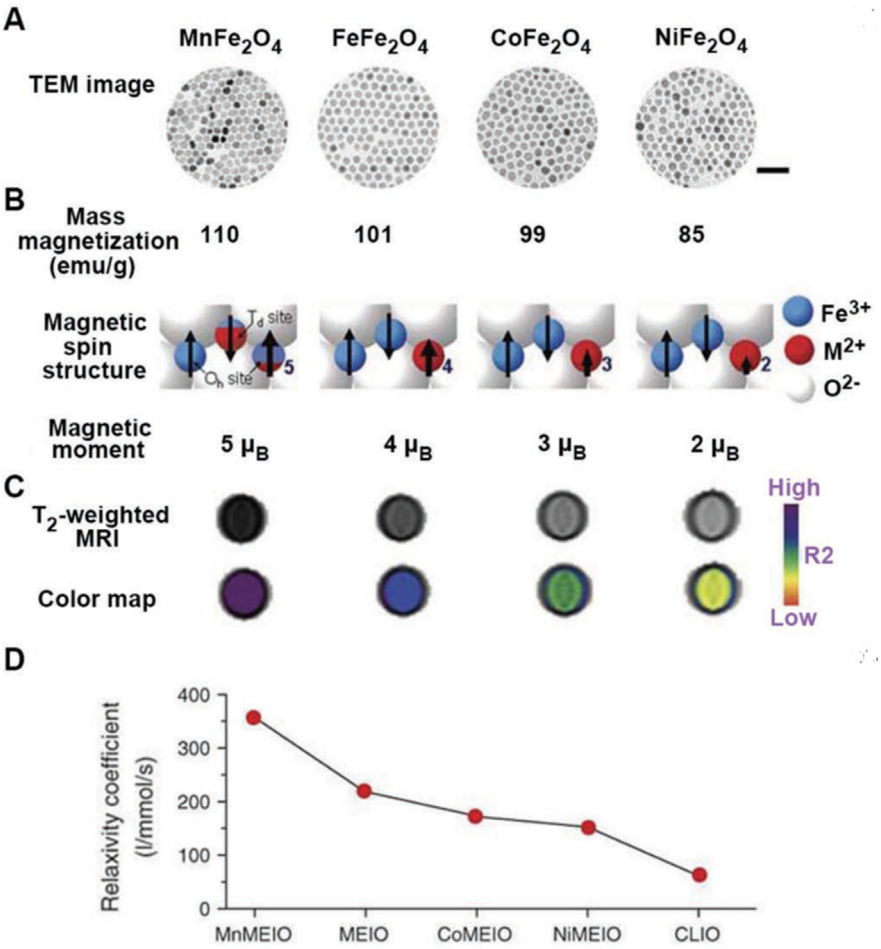

Fig. 11. A) TEM images of $MnFe_2O_4$, Fe_3O_4, $CoFe_2O_4$, and $NiFe_2O_4$, B) Magnetization values, schematic of the spin alignment in the spinel structures and magnetic moment of the NPs, C, D) MR phantoms and calculated T_2 relaxivity coefficient. Adapted and reprinted with permission from reference [113].

Manganese oxides are used as positive agents. The ferrite nanostructure like MFe_2O_4, M = Fe, Mn, Co is used as T_2 agents due to their strong magnetizations. It is familiar that particle degradation rate is inverse to particle size. Smaller particles exhibit high surface M^{2+} ions and higher release of M^{2+} than larger particles [105]. Thus, by reducing the NPs size can improve the longitudinal relaxivity, as demonstrated by a larger r_1 value. This strategy has been incorporated in ferrite-based NPs to improve longitudinal relaxivity. Decreasing of their particle size into the ultrasmall range leads to a small r_2 / r_1 ratio and a pronounced T_1 -enhanced effect observed. T_2 and dual-mode contrast agent concepts arise to eliminate the possible artifacts of the single-mode contrast images by combining strong T_1 and T_2 contrast effects in a single contrast agent. Zang et al. [156] studied ultra-small $MnFe_2O_4$ NPs of size 3 nm synthesized by the thermal decomposition method as a T_1 MRI nanoprobe. The MRI measurements were taken at 3 T for different concentrations of [Fe + Mn], and it was measured as r_1 relaxivity of 8.43 $mM^{-1}s^{-1}$. They have also conducted a study in pH 5, as the leaching of metal ions occurs in acidic pH, as reported in the literature. However, the results show no change in T_1, indicating the stability of $MnFe_2O_4$ NPs. For comparison, γ-Fe_2O_3 of similar size (3 nm) was synthesized by the same method and it exhibited a relaxivity longitudinal relaxivity(r_1) of 4.96 $mM^{-1}s^{-1}$. Thus, $MnFe_2O_4$ has a more considerable r_1 value which can be attributed to the doping of Mn^{2+}. Further, they conducted an *in vivo* study on Sprague – Dawley (SD) rats for imaging liver and blood vessels. The MR images of the blood vessels and liver showed notably brighter T_1 images after administering ultrasmall $MnFe_2O_4$, indicating shortening of spin – lattice relaxation time of water protons in the circulating system. Lee et al. [113] research group reported the successful synthesis of MFe_2O_4 NPs where M is + 2 cations like Fe, Mn, Co and Ni metal ions. The synthesized MNPs are 12 nm in size, with a high monodispersity of $\sigma < \sim 8$ %. The magnetic properties of these NPs have been studied using a superconducting quantum interference device (SQUID) magnetometer and spin–spin relaxation time (T_2)-weighted MR images taken at 1.5 T. $MnFe_2O_4$ NPs when compared to other types of NPs showed the highest magnetization value of 110 emu g^{-1}. This is due to the inverse spinel structure of $MnFe_2O_4$ where, $Mn^{2+}_{1-x}Fe^{3+}_x$ (0 < x less than 1) occupies tetrahedral sites, and $Mn^{2+}_xFe^{3+}_{2-x}$ occupies the octahedral sites. For other NPs, Fe^{3+} occupies tetrahedral, whereas Fe^{3+} and M^{2+} occupy the octahedral sites. When an external field was applied, the magnetic spins at the tetrahedral sites align in an antiparallel direction to the applied field, whereas spins in octahedral sites align in the parallel direction. Thus, $MnFe_2O_4$ had the magnetic spin in the order of 5 μB with the highest magnetic susceptibility, whereas other NPs exhibited approximately 4 μB to 3 μB to 2 μB in the order Fe_3O_4, $CoFe_2O_4$ and $NiFe_2O_4$, respectively as shown in Fig. 11. Thus, $MnFe_2O_4$ shows the strongest T_2 contrast with a transverse relaxivity (r_2) value of 358 $mM^{-1}s^{-1}$. The single contrast agent T_1 or T_2 usually results in susceptibility artifacts and MR signal loss. By using the same contrast agent as dual T_1/T_2 contrast for MRI, fault free images with improved detection accuracy can be obtained. Thus, Xiao et al. [157] worked on the dual contrast agent using $MnFe_2O_4$ NPs. They have successfully synthesized 3 nm PEG (polyethylene glycol) coated $MnFe_2O_4$ NPs with high monodispersity and good biocompatibility. The NPs were dispersed in TMAH solution, and MR images were taken at 3 T, which shows transversal

Table 5
Reported manganese ferrites as MRI contrast agent with the applied field in Tesla (T).

Manganese ferrite NP	Approximate Size nm	Shape	M_S (emu g^{-1})	Relaxivity ($mM^{-1}s^{-1}$)		Applied field T	Ref
				r_1	r_2		
$MnFe_2O_4$	2	Sphere		8.43		3	[156]
	3			8.23			
	3.9			6.98			
$MnFe_2O_4$	20	sphere	76.2		394	1.47	[158]
$MnFe_2O_4$	10	Sphere		14.3	82.94	3	[159]
Mn/Fe molar	88	Sphere	76	22.1	185.1	1.5	[160]
Ratio	85		65	17.2	183.9		
0	81		60	16.5	257.4		
0.036	66		72	16.5	245.4		
0.046	112		69	15.2	277.7		
0.066	101		62	17.2	275.9		
0.083	148		51	8.3	140.2		
0.111							
0.2							
Mn doped iron oxide	4.5	Sphere	14.9	8.24	17.95	0.5	[161]
PEG-$MnFe_2O_4$	50		60		347.5	1.5	[109]
$MnFe_2O_4$	20	cubes	59		296.11	1.5	[162]
$Mn_{0.43}Fe_{2.57}O_4$	19.97 ± 4.61	Sphere	89.5		506.6	0.5	[70]
					904.4	7	
$MnFe_2O_4$	34	cube	48		112.1	7	[163]
$MnFe_2O_4$	6	Sphere	50	0.8	63	9.4	[101]
	7.5		60	1.3	101.5		
	9		72	0.9	136.6		
	12		92	2.3	261.1		
	14		106	1.3	335.6		
Mn doped iron oxide		Sphere	62.4		236.6	1.5	[164]
(Mn^{2+}:Fe^{2+})	7.8		60.5		203.9		
1:3	7.4		71.13		202.1		
1:1	9.6						
3:1							
mPEG –$MnFe_2O_4$	6	sphere	41.5		75.7	3	[165]
mPEG-g-PEI-$MnFe_2O_4$			39.6		331.8		
$MnFe_2O_4$	18	octahedral	54.67	11.4	48	0.5	[166]
Gd labeled $MnFe_2O_4$	74		19.21	20.5	68.48		
$MnFe_2O_4$ – Fe_3O_4	12.5	Core shell	69.34		184.1		[167]

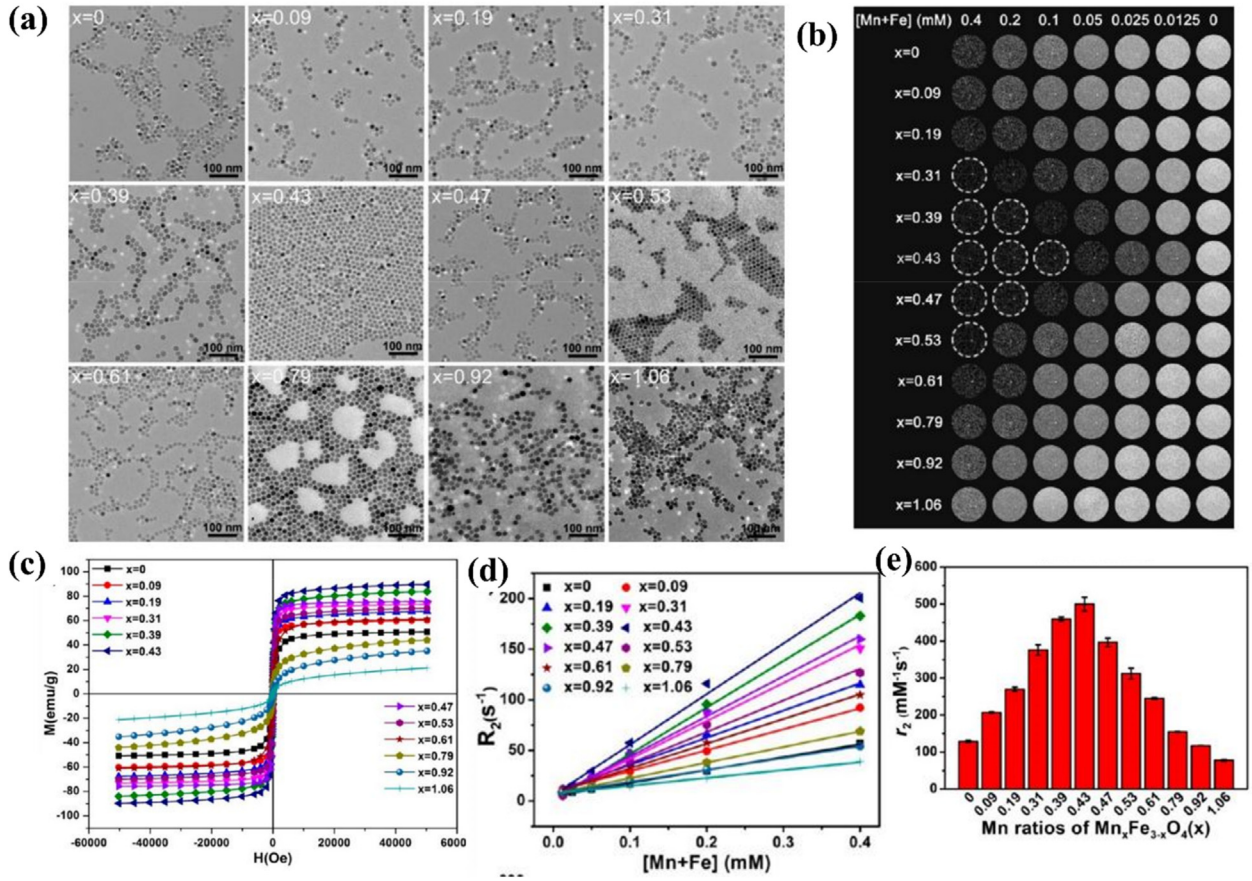

Fig. 12a. (i). Morphological and magnetic studies of different shape $MnFe_2O_4$ NPs. (a) TEM image of $Mn_xFe_{3-x}O_4$ NPs with different doping level (x = 0–1.06), (b) M−H curves of $Mn_xFe_{3-x}O_4$ NPs, (c) r_2 relaxivity graph and MR images of $Mn_xFe_{3-x}O_4$ NPs at different concentration. Adopted and reproduced with permission from reference [70],

relaxivity r_2 = 120.9 $mM^{-1}s^{-1}$ and longitudinal relaxivity r_1 = 7.1 $mM^{-1}s^{-1}$. In general, Mn^{2+} shows the highest paramagnetism with five unpaired electrons when compared with other transition metal ions. Based on the inner-sphere theory, the T_1 relaxivity of the NPs is influenced by the number of water molecules bound per metal ion and the residence lifetime (τ_M) of the bound water molecules. It is known that τ_M of Mn $(H_2O)_6^{2+}$ is 4.3 × 10^4 ns which is smaller than other transition metal ions. Thus, it accelerates spin–lattice relaxation and increases r_1. The outer-sphere mechanism dominates the T_2 relaxation depending on the proton gyromagnetic ratio, molar mass, surface coating thickness, density, and radius of NPs (a). Transversal relaxivity, r_2 is proportional to a^3 and inversely proportional to M_S. They had doped Mn^{2+} ion to increase the M_S since $MnFe_2O_4$ has a mixed spinel structure, resulting in the increase of r_2 value. Literatures reported on the use of $MnFe_2O_4$ NPs as MRI agents is summarized in Table 5..

The interest in manganese ferrite as an imaging agent has been steadily increasing in the past decade. The advancement in synthesis protocols has allowed the production of various shapes of NPs. Most of the investigations on $MnFe_2O_4$ NPs have been carried out in spherical shapes, although other shapes (e.g., rods, disks, cubes, octahedrons etc.) have also been synthesized. The study of other shapes of $MnFe_2O_4$ NPs is rather scarce. The imaging performance of the contrast agent are highly dependent on its magnetic properties, effects of shape and size on the behavior of magnetic particles have been known for more than half a century. For similar sized spherical and cubic particles, the saturation magnetization (M_S) was found to be higher for cubic particles owing to its shape anisotropy. Yang et al. [70] prepared spherical shaped manganese ferrite NPs and investigated the effects of manganese concentration on magnetic properties and its contrast abilities. They prepared Mn_x-$Fe_{3-x}O_4$ NPs with different Mn contents (x = 0–1.06). The HRTEM images show the change in lattice distance when Mn doping level is elevated, but the particle size is almost 10 nm and is similar for all the doping levels (Fig. 12i(a)). They measured the magnetic properties at a magnetic field of 5 T for all the doping levels. The $Mn_xFe_{3-x}O_4$ NPs exhibit superparamagnetic behaviors when × is below 0.61, when × is increased, it behaves partially paramagnetic (Fig. 12i**(b)**). They obtained the highest magnetization of 89.5 emu g^{-1} for x = 0.43. The relaxivity studies on 0.5 T MRI show r_2 values (Fig. 12i**(c,d,e)**) of 128.3 $mM^{-1}s^{-1}$ for Fe_3O_4 (i.e. for × = 0) and for × = 0.09 to × = 1.06 the r_2 value is 206.9 ± 1.9, 269.3 ± 6.0, 375.9 ± 14.1,459.5 ± 5.7, 506.6 ± 18.7, 396.7 ± 11.5, 312.1 ± 14.8, 244.4 ± 2.6, 154.4 ± 1.2, 117.3 ± 0.6, and 77.7 ± 2.4 $mM^{-1}s^{-1}$, respectively. The highest r_2 value is obtained for × = 0.43, due to its largest saturation magnetization, which is fourfold higher than that of Fe_3O_4 NP. Their work provides a knowledge that besides morphology, size, composition of NPs is also to be carefully considered for designing a contrast agent. In our previous study [149], we synthesized cubic shape manganese ferrite NPs by simple hydrothermal method and varied their morphology and size by changing the reaction solvent ratios. FESEM images show the variation in the average size of NPs, and it is in the range of 113 to 147 nm (Fig. 12**ii(a)**). The perfect cube particle size is 135 nm with saturation magnetization of 62.73 emu g^{-1} shown in Fig. 12**ii(b)**. In this study, the T_2-contrast ability of NPs was evaluated by 7 Tesla

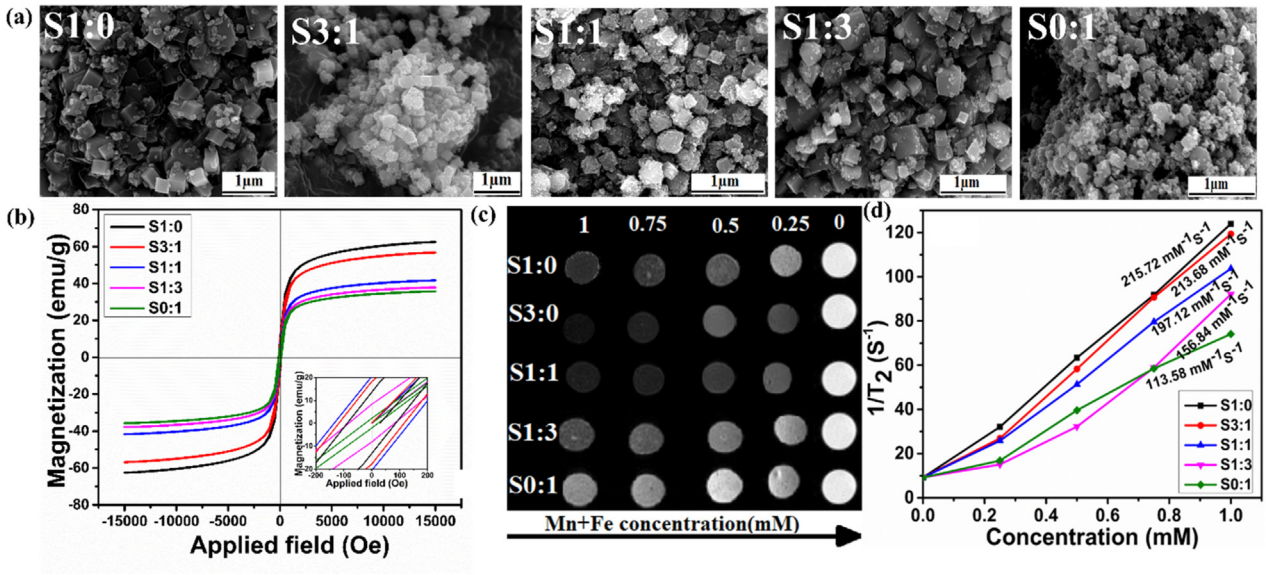

Fig. 12b. (ii). (a) FESEM images of cubic shape NPs, (b) Magnetization (M) versus applied magnetic field (H) plots for $MnFe_2O_4$ NPs and (c,d) MRI studies at different concentration levels. Adopted and reproduced with permission from reference [149].

Animal MRI and the r_2 values are found to be in the range of 215.72 to 113.58 $mM^{-1}s^{-1}$ (Fig. 12**ii(c,d)**). The cubic particle with highest magnetic saturation obtains high r_2 value of 215.72 $mM^{-1}s^{-1}$.

5.3. Hyperthermia

Cancer treatment modalities includes radiation therapy, chemotherapy, hyperthermia (HPT) and surgery. Clinical HPT has three categories viz., localized HPT, regional HPT, and whole-body HPT. HPT is heating specific tissue or tumors to 41 to 46 °C where the natural enzymatic processes are destroyed, keeping the tumor alive [168]. Inside the cancerous tissue, blood vessels are poorly developed and thus have low thermal resistance as compared to normal tissues. HPT is a promising therapy for cancer since tumor cells are more susceptible to heat due to their higher rate of metabolism and are currently used in clinical trials [169–172]. The main challenge in HPT is insufficient heat generation to the tumor location by lowering the exposure time and controlled heating. This can be accomplished using MNPs with high specific loss power (SLP) or specific absorption rate (SAR) at a lower concentration. The SLP or SAR value is the measurement of heat generated per unit mass. The SLP of NPs is dependent on particle size, distribution, shape, anisotropy constant, saturation magnetization and surface modification. In the MHT, induced local heating at the tumor site is achieved by controlling the AMF. The heat generated by the MNPs depends on the amplitude and frequency of the applied field and the type and size of the particle used [173]. In HPT, the AMF used is in the radiofrequency range between several kHz and 1 MHz, which can penetrate deep enough to access the inner organs/tissues in the body and is entirely harmless. The heat generation in MHT is due to several factors, as shown in Fig. 13(a).

(1) Hysteresis loss: The heat generated by superparamagnetic nanomaterials is theoretically zero, primarily because these particles exhibit zero remanence and coercivity when subjected to a dc magnetic field. However, in the presence of a high-frequency alternating magnetic field, typically in the range of 200–400 kHz, individual magnetic spins of these tiny nanomagnets fail to follow the

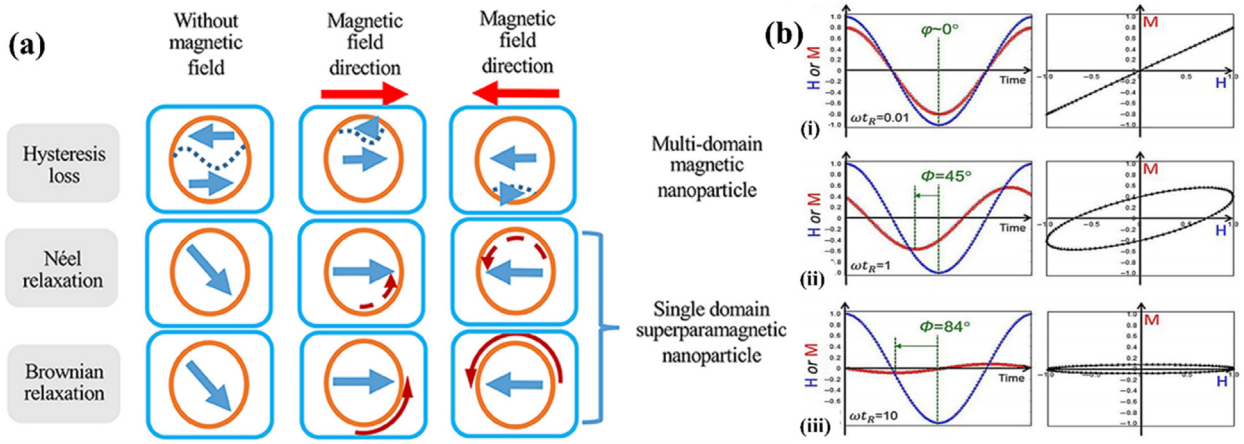

Fig. 13. (a) Heat generation mechanisms of magnetic NPs in an external AC magnetic field. Circles represent MNP; curved dashed arrows represent the change in magnetic moment direction, curved red arrow represents particle movement, and short straight arrows represent magnetic field direction. Adopted and reproduced with permission from reference [10], and (b) Schematic illustration showing how magnetization phase lag in the linear response regime leads to an elliptical hysteresis loop. Adopted and reproduced with permission from reference [174].

fast-flipping magnetic field. As a result, a phase shift arises between the magnetization (M) and the magnetic field (H) vectors, which is responsible for the emergence of an elliptical hysteresis loop (Fig. 13(b)). Hence, it is to be remembered that ac hysteresis contributes to heat generation during magnetic hyperthermia. At low frequencies, M could easily follow H, hence no loop formation is observed (**Figure 13(b)i**). As the frequency is increased, the phase lag between M and H emerges. At 450 phase shift, the hysteresis loop area is maximum (**Figure 13(b)ii**), however, the loop area begins to diminish as the phase difference angle moves beyond 450 (at 900, the area recorded is the least, **Figure 13(b) iii**) [174].

(2) Brownian relaxation: It is the heat generation due to the physical rotation of the particle. The Brownian mechanism depends on the viscosity of the surrounding fluid and the volume of the particle. When the magnetic anisotropy constant is high enough to overcome viscous resistance, the magnetic moment will be fixed while the particle will rotate. The Brownian relaxation mechanism was first given by Brownian [175] as in Eqn. (15):

$$\tau_N = \frac{3\eta V_H}{kT} \tag{15}$$

Where η is the viscosity of the solution and V_H is the hydrodynamic size of the particle.

(3) Néel relaxations: It is defined as the heat generated by rotating individual magnetic moments in the particle. When the particle is in the nanometer range with a single domain, each particle will have a magnetic moment. When the applied field displaces the magnetic moment and relaxes back to the preferred orientation, thermal energy is released, resulting in local heating. The time constant of the applied field in Neel relaxation is short enough to rotate the magnetic moment alone while physical orientation

Table 6
Summary of reported manganese ferrite NPs for hyperthermia with SAR values.

Nanoparticle	Size nm	Shape	M_S emu g^{-1}	SAR or SLP W g^{-1}	Frequency kHz	Applied field kA m^{-1}	Ref
$MnFe_2O_4$	11	Sphere	58.18	97	300	15	[179]
$MnFe_2O_4$	80	Cluster	76	1170	355	65	[146]
$MnFe_2O_4$ – Ag		Irregular shape			340	100 Oe	[180]
Mass ratio	23.6		66.5	~52			
1:0	25.4		~50	~25			
2:1	32.3		~40	~80			
1:1	28.5		~25	~70			
2:1	37		16.1	~60			
1:2.5							
$MnFe_2O_4$	6	Spherical	58.28	16	276	13.3	[181]
				32		20	
				54		26.7	
$Mn_{0.1}Fe_{2.9}O_4$	6 to 8	Sphere	66	70	829		[160]
$Mn_{0.29}Fe_{2.71}O_4$			62	71			
$Mn_{0.66}Fe_{2.34}O_4$			63	88			
$Mn_{0.74}Fe_{2.26}O_4$			67	111			
$MnFe_2O_4$	10	Sphere		145	300	15	[182]
$MnFe_2O_4$/ZnS	~45	Sphere	1.8182	27.03	336	Field amplitued 226 G	[183]
Chitosan- $MnFe_2O_4$	17.63	Cube	58.34	278.6		50	[76]
DMSA- $MnFe_2O_4$	12	Sphere	44.1	1.45	266	653 Oe	[108]
Chitosan- $MnFe_2O_4$ (0.3 %)	17.2	Sphere	40.2	1.20			
Chitosan- $MnFe_2O_4$ (0.6 %)	17.7	Sphere	39.8	1.17			
Chitosan- $MnFe_2O_4$ (0.6 %)	18.3	Sphere	31.2	1.08			
Chitosan- $MnFe_2O_4$ (1.2 %)	17.1	Sphere	36.7	1.15			
$MnFe_2O_4$	10–12			60	300	20	[184]
$Fe_{0.2}Mn_{0.8}Fe_2O_4$				35			
$Fe_{0.6}Mn_{0.4}Fe_2O_4$				92			
$MnFe_2O_4$	21	Sphere	75	295	195	50	[185]
$MnFe_2O_4$	15	Sphere	125	414	500	37.3	[186]
$CoFe_2O_4$ @ $MnFe_2O_4$	15	Core shell	110	2280			
$MnFe_2O_4$ @ $CoFe_2O_4$	15	Core shell	108	3034			
$MnFe_2O_4$	10	Sphere	14.5	42	765	28	[187]
$CoFe_2O_4$ @ $MnFe_2O_4$	26.5	Core shell	33.	73			
$MnFe_2O_4$ @ $CoFe_2O_4$	16.1	Core shell	26.4	160			
$MnFe_2O_4$	31	Sphere	69.5	455.3	768	300 Oe	[188]
$MnFe_2O_4$		Sphere		110	300	400	[189]
$MnFe_2O_4$- GO				160		600	
				150		800	
				100		400	
				180		600	
				300		800 Oe	
$Mn_{0.3}Fe_{2.7}O_4$	10	Sphere		164	380	7	[112]
$Co_{0.03}Mn_{0.27}Fe_{2.7}O_4$	18	sphere		1140			
	22	Polyhedral		2278			
	22	polyhedral		3417			
Fe_3O_4	96		71	61	183	17	[190]
$Mn_{0.3}Fe_{2.7}O_4$	110		62.7	37			
$Mn_{0.6}Fe_{2.4}O_4$	65		66	73			
$MnFe_2O_4$	4.5			42.22	231	60	[191]
MWCNT- $MnFe_2O_4$	6.9			53.14			
$MnFe_2O_4$	16	Sphere	61	92	276	9.8	[192]
$MnFe_2O_4$ (water)	83	Clusters	76	1170	355	20	[146]
$MnFe_2O_4$ (PEG)				1395		17	

remains the same. Neel first gave this relaxation mechanism, and it is given by the term τ_N in Eqn. (16).

$$\tau_N = \frac{\tau_o}{2}\sqrt{\pi\frac{kT}{KV}}e^{\frac{KT}{KV}} \quad (16)$$

Where V is the volume of the NP, and K is the anisotropy constant.

For example, in a study by Cruz et al. [176], $MnFe_2O_4$ and $CoFe_2O_4$ NPs were synthesized using the hydrothermal method in two different temperatures 175 and 230 °C and two different mediums such as normal and gelatinous. The SLP of $MnFe_2O_4$ at 175 °C in gelatinous medium showed the highest value among the reported values. The particle size of $CoFe_2O_4$ and $MnFe_2O_4$ at 175 °C in the gelatinous medium is 4.4 and 4.6 nm, respectively. At 175 °C in the gelatinous medium, the SLP value of $CoFe_2O_4$ and $MnFe_2O_4$ is 24 and 198 W g^{-1}, respectively, which shows the variation of energy released by the two particles. They explained that the variation in results though the particle size is almost the same, is due to the difference in the magnetic properties, most likely magnetic anisotropies (for bulk $CoFe_2O_4$ (K = 2.7 × 10^5 J m^{-3}) and $MnFe_2O_4$ (K = − 3.3 × 10^3 J m^{-3})). For very small MNPs, Neel relaxation will be dominant, and it depends on the magnetic anisotropy K. By simple calculation, assuming bulk values for the magnetic anisotropy constant (K), the Néel relaxation dominates over Brownian relaxation up to 6 nm diameter in the case of $CoFe_2O_4$, and up to 20 nm for $MnFe_2O_4$. Thus, the magnetic anisotropy constant is reduced by the different orientations, and Neel relaxation dominates in the case of $MnFe_2O_4$ NPs, providing high SLP. The particle size and the ratio of the distribution of cations in the spinel structure can also influence the hyperthermic behavior of NPs. In one of our previous studies [177], we synthesized $MnFe_2O_4$ NPs by thermal decomposition method with different solvents. The solvent used were phenyl ether, benzyl ether, and octadecene resulting in different sizes of NPs 10, 12 and 11 nm, respectively. All the samples have reached hyperthermia temperature in less than three minutes. We have conducted hyperthermia studies for all the samples at two different concentrations at the frequency of 314 kHz

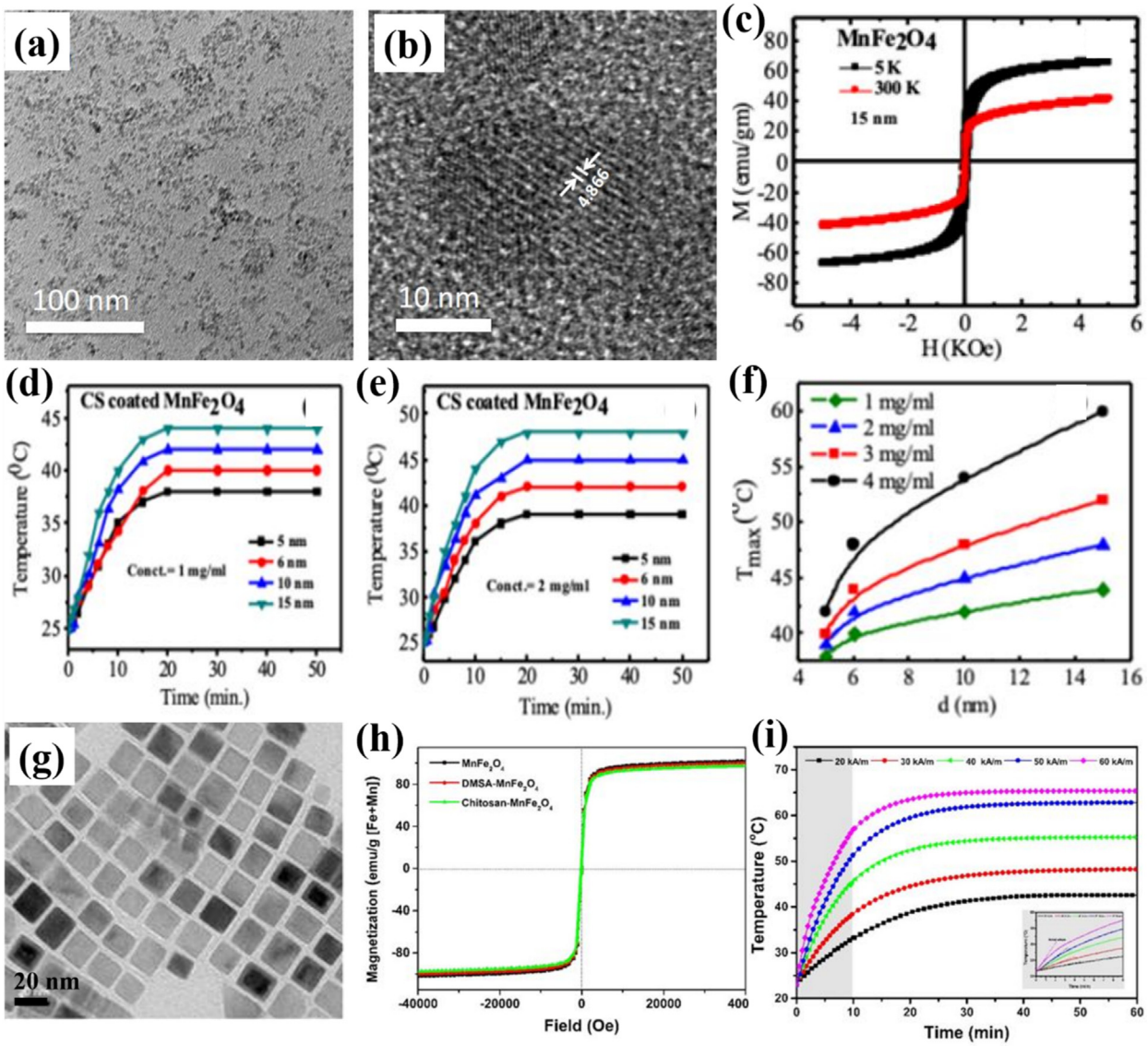

Fig. 14. Morphological, magnetic study and HPT behavior of spherical and cube shape $MnFe_2O_4$ NPs. (a),(b) TEM image of spherical shape $MnFe_2O_4$ NPs (c) Magnetization (M) versus applied magnetic field (H) plots of spherical shape chitosan coated $MnFe_2O_4$ NPs, (d,e) Temperature versus time curve of spherical shape $MnFe_2O_4$ NPs NPs at 1 and 2 mg mL^{-1} concentration, (f) maximum SLP values obtained by different size particles at different concentration [147], (g) TEM image of cubic shape NPs, (h) Magnetization (M) versus applied magnetic field (H) plots for cubic shape $MnFe_2O_4$ NPs and (f) HPT behavior of cubic particle at different applied field. Adopted and reproduced with permission from reference [76].

and field strengths of 375, 425, 475, 525 and 575 Oe. When the concentration and field strength increases, we have noted a substantial increase in the NPs SAR values. The SAR values of 10 nm size particles in the order of above mention field strength is 56.5, 57.73, 63.6, 74.75 and 97.69 W g^{-1}, for 12 nm particle 133.22, 185.3, 251.65, 284.95 and 329.36 W g^{-1} and for 11 nm size 162.8, 199.8, 274.1, 360 and 384.8 W g^{-1} respectively. The ratio of the distribution of cations in the spinel structure can also influence NPs hyperthermic behavior. Doaga et al. [178] studied the HPT behavior of different $Mn_xFe_{1-x}Fe_2O_4$ (x = 0 to 1) prepared by the co-precipitation method. The sample sizes were in the range of 10.5 to 19.0 nm, and they exhibited superparamagnetic behavior, which is ideal for HPT application. The magnetization of the NPs increases with the increase in the value of x; for × = 0, 0.2, 0.4, 0.6, 0.8 and 1, M_S values of 53.4, 56.3, 63.3, 68.2, 68.7 and 68.8 emu g^{-1} were obtained respectively. The SAR values measured at a frequency of 1.95 MHz and field strength of 4.5 kA m^{-1} increase with × value from 66.9 to 148.4 W g^{-1}. This is due to the replacement of Fe^{3+} by Mn^{2+} ions on the A-site; thus, the moment in A-site remains constant with a value of 5μB, but the magnetic moment increases in the B-site resulting in the increase of magnetization. At the higher magnetization, the heat generation is dominated by Neel relaxation and magnetocrystalline anisotropy played a major role. Another important factor here for achieving high SAR values is controlling the particle's size. One of the highest SAR value of manganese ferrite in the literature was 1661 W g^{-1} were reported by Mazario and her group [158]. To achieve this high SAR the prepared NPs of approximately 20 nm in size were subjected under a magnetic field of 30 mT at 717 kHz frequency. Table 6 show the literatures on manganese ferrite NPs as heating agent for magnetic fluid hyperthermia.

HPT behaviors are highly dependent on morphological and magnetic properties of the MNPs. The comparative analysis has been carried out in this review to better understand the influence of shape in HPT behaviour. First, for spherical particle we are considering the study conducted by Islam and his group [147]. In their study, they synthesized $MnFe_2O_4$ NPs by co-precipitation method and varied the NP's size by changing the reaction mixture's pH. The obtained chitosan coated $MnFe_2O_4$ NPs are in the size range of 5 to 15 nm (Fig. 14**(a,b)**). The magnetization versus applied field studies were done at 5 and 300 K and the magnetization values were 8, 12, 19 and 41 emu g^{-1} at 300 K for 5, 6, 10, and 15 nm, respectively. The maximum saturation magnetisation for 15 nm sized particle at room temperature is 41 emu g^{-1} (Fig. 14(c)). The HPT studies calculated with the applied radio frequency of 342 kHz for 1, 2, 3, and 4 mg mL^{-1} sample concentrations (Fig. 14**(d, e and f)**). From the experiment the calculated SLP value for 15 nm particle is 200 and 150 W g^{-1} for 1 and 2 mg mL^{-1} concentration. For cubic particle the study conducted by Oh and his group [76] was compared. They prepared chitosan coated $MnFe_2O_4$ nanocubes by thermal decomposition method. The obtained NPs are in the size of 17 nm with saturation magnetization of 58.34 emu g^{-1} for Chitosan-$MnFe_2O_4$ nanocubes (Fig. 14**(g and h)**). HPT studies of nanocubes with 1.5 mg mL^{-1} concentration were measured at AC magnetic field amplitudes from 20 to 60 kA m^{-1}. The measured SAR was 57.2, 97.5, 152.21, 209.41, and 278.69 W g^{-1}, which corresponded to the maximum temperatures of 44.10, 48.24, 55.25, 62.81, and 65.38 °C, respectively. In these two studies the particle size were almost similar. However, the magnetization of spherical particle is smaller than cubic particle, this can be explained by shape anisotropy factor influencing the magnetic properties. From these studies, we can understand the impact of shape of the particle is highly important for the magnetic property and HPT behavior.

5.4. Drug delivery

From 1854 to 1915, Paul Ehrlich was the first to propose the idea of selective drug delivery to a particular location by the term 'magic bullet'. In 1908, Paul Ehrlich received a Nobel prize for his magic bullet idea in the field of immunity. Since then, the drug delivery to the targeted site of action was carried out by various strategies like sensitivity to physical stimuli or recognition moieties on the drug. Before using MNPs in drug delivery, it was used only as a contrast agent for localized radiation therapy. In 1960 Freeman et al. [193] proposed that MNPs can be guided through the vascular system to a specific location by an external magnetic field. Magnetic NPs guided by an external magnetic field directly to a tumor location for controlled drug release as shown schematically in Fig. 15. The use of MNPs in chemotherapeutic delivery has evolved since the 1970 s. In 1978, Widder et al. [194] used a magnetic albumin microsphere in an animal model for delivering

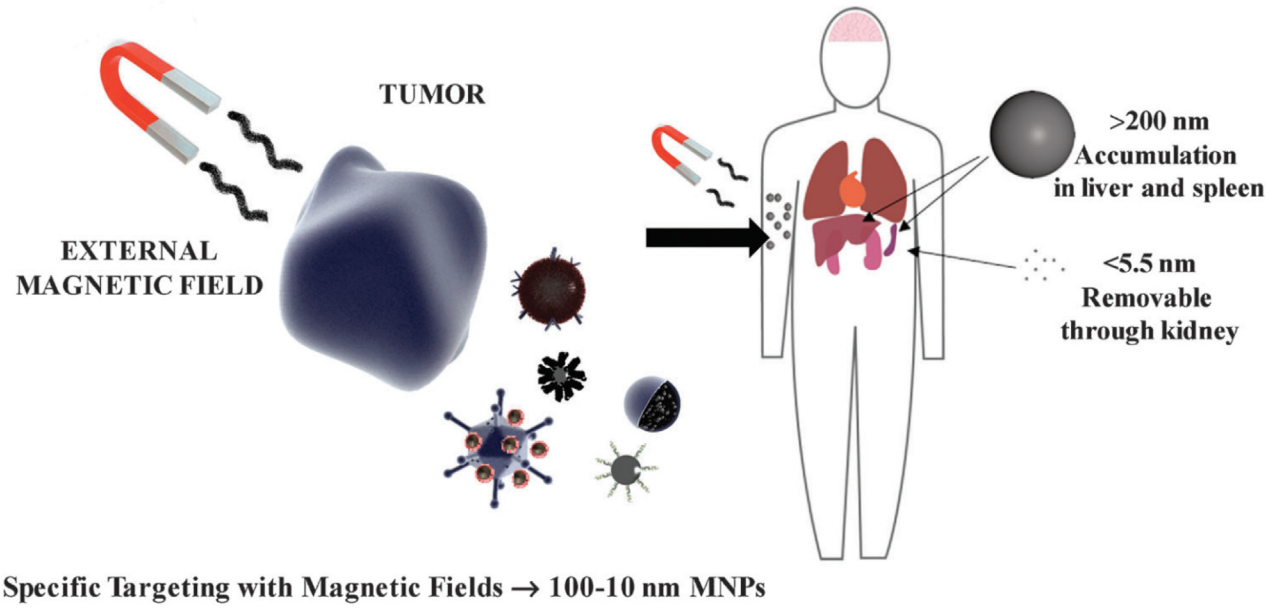

Fig. 15. Drug loaded magnetic nanovectors to a specific site guided by an external magnetic field. Adapted and reprinted with permission from reference [110].

doxorubicin. In the 1980 s, many authors proposed magnetic microspheres and microplates for delivering different drugs [195–197]. However, till 1996, all the magnetic delivery approaches were carried by micro sized particles. The first MNP for drug delivery in an animal model was proposed by Lübbe et al. [198]. Since then, several groups have shown the potential of magnetic vectors for drug delivery application. Some of the commercialized MNPs for delivery are TargetMAG-doxorubicin and FluidMAG by Chemicell and MagNaGel by Alnis Biosciences, Inc. [199]. MNPs in drug delivery have some main advantages: the particles can be held or guided through an external field to a particular place, visualizing through a diagnostic technique like MRI and triggered drug release or heat generation using MHT [200]. Drug loading is the most challenging and important factor for clinical delivery applications. The drugs can either be absorbed/entrapped into the pores of NPs or encapsulated within NPs or covalently bonded to the surface of NPs. The key parameters for drug loading are the size, shape, and surface chemistry of NPs. Drug loading is generally classified into two methods based on the physical and chemical interaction. (1) *Chemical attachment:* The covalent bond existing between the conjugated ligand and the function groups of MNPs like carboxyl, hydroxyl, amine, and thiol are strong and provide a stable linkage for drug loading. These groups can be anchored on the surface of NPs by polymer coating, and this technique is generally used for small molecule conjugation. These groups are found either at the end of the polymer chain, like that seen in polyethylene glycol or at the middle, like in dextran and chitosan. The covalent attachment takes place by linking the functional group and the similar group on the therapeutic agent. (2) *Physical attachment:* Hydrophobic/hydrophilic, electrostatic, and affinity interactions are the major types of physical attachment interactions. The main advantages of physical interactions are fast binding, no need for intermediate linkage, and high efficiency. However, it is not stable as chemical interactions [201]. Hydrophobic/hydrophilic interaction occurs when hydrophobic MNPs absorb a hydrophobic drug on the surface, making NPs hydrophilic. The drug release will occur by the degradation of coating in an intracellular environment [202]. Electrostatic interactions take place when

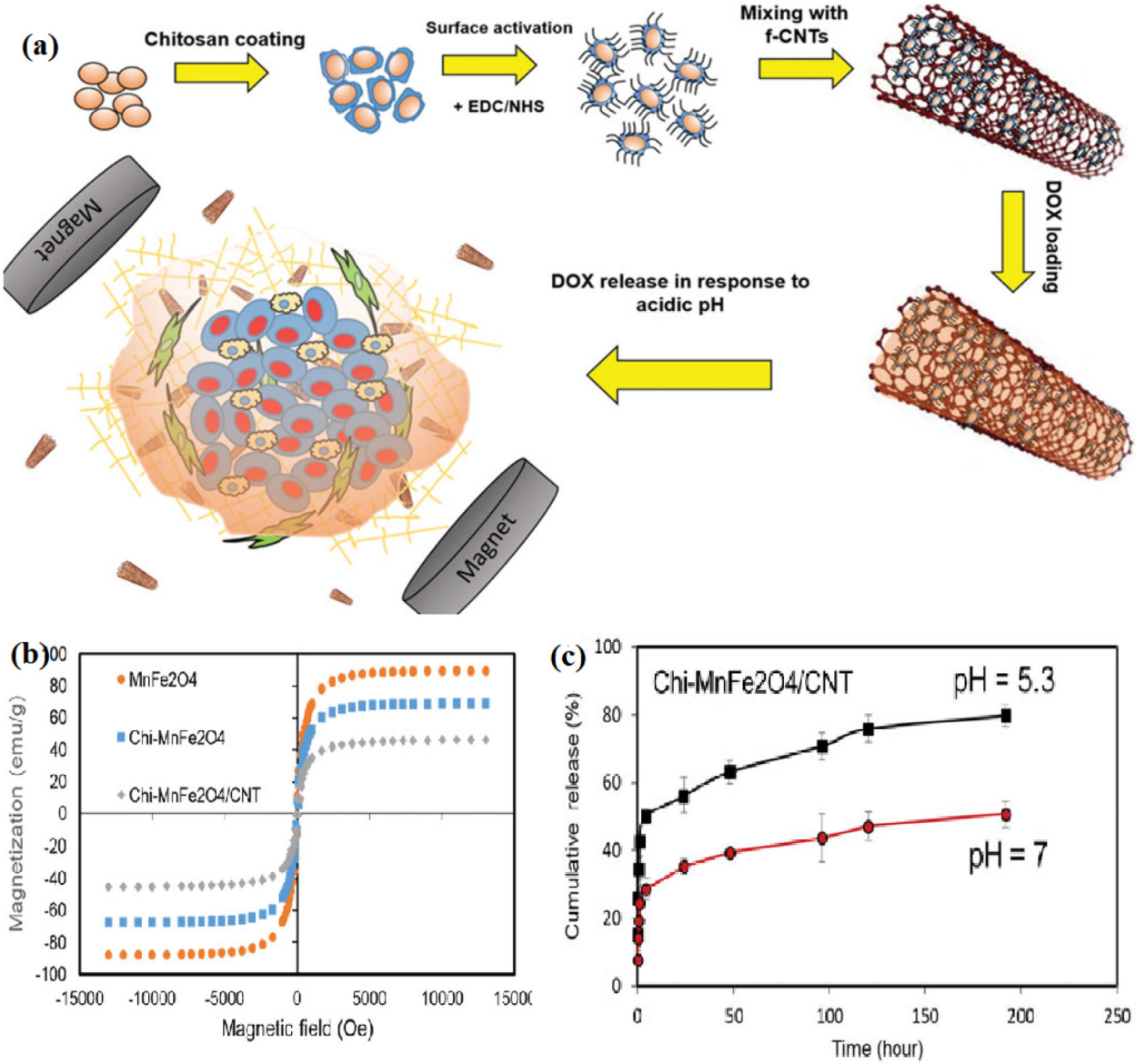

Fig. 16. (a) Schematic view drug loading and release of the MNP in the tumor microenvironment (b) VSM plot of the $MnFe_2O_4$, Chitosan coated $MnFe_2O_4$ and the hybrid Chi-$MnFe_2O_4$/CNT sample cumulative release profile of the (c) Chi- $MnFe_2O_4$/CNT. Adapted and reprinted with permission from reference [131].

cationic coated MNPs are complexed with the negatively charged drug. The key parameters for magnetic nanocarriers in drug delivery are size, hydrodynamic volume, distribution, surface chemistry and magnetic properties. The surface chemistry is an important factor in avoiding the reticuloendothelial system and increasing half lifetime (circulation time) in bloodstreams, achieved by coating NPs.

Ravichandran et al. [203] fabricated the core–shell structure of $MnFe_2O_4$ and gold NPs (Mnf@Au) for drug delivery application. They have used the surface modification technique by using folic acid as an intermediate ligand for effective docking of anti-cancer drugs. The main reason for choosing folic acid on the surface is that it acts as a steering molecule toward the folate receptor on the cancer cells and enters the cell through endocytosis. The magnetic nanocarrier obtained was of size ~ 25 nm with a magnetization of 61.1 emu g^{-1}. The highly stable DOX-FA-Mnf@Au was subjected to internalization studies to confirm the accumulation of NP inside the cell and not only with the cytoplasm. The research proved the passing of DOX-FA-Mnf@Au through the cell membrane by an endocytic mechanism. They showed 97.5 % of drug loading efficiency, and drug release studies were found to be 79.6 % at pH 5.4, 76.9 % at pH 6.8 and 37.6 % at pH 7.4. In another study by Kim et al. [108], investigations were carried out on chitosan encapsulated $MnFe_2O_4$ for HPT and magnetically triggered drug delivery. Chitosan was chosen because it is biocompatible, frequently used in drug delivery, and does not cause any allergic reaction to living tissues because of its positive charge. They chose theophylline as a model drug due to its ease to disperse easily throughout the coating with its small size. The synthesized chitosan- $MnFe_2O_4$ is of size 18 nm with a magnetization of 44.1 emu g^{-1}. They showed the most effective drug loading and release by chitosan- $MnFe_2O_4$. Seyfoori et al. [131] designed a multifunctional magneto/pH-responsive nano-hybrid system to deliver the anticancer drug doxorubicin. First, they fabricated $MnFe_2O_4$ nanogel by coprecipitation method with chitosan as the coating. The nanocomposite was then prepared by mixing functionalized multi-wall carbon nanotube (MWCNT) with $MnFe_2O_4$ nanogel by EDC and the NHS as crosslinkers, as shown schematically in Fig. 16. The M_S obtained from VSM shows a value of 48 emu g^{-1} after conjugation to the carbon nanotube. The drug loading and release efficiency was calculated for functionalized CNT (F-CNT) and nanohybrids, which showed the loading percentage of 71 and 92 %, respectively. The reason for high loading efficiency in nanohybrid is because of π-π interaction and electrostatic interaction of carbon atoms in chitosan and DOX molecules. The release profile was taken at two different pH 5.3 and 7, to imitate the cancerous and physiological environment, respectively. The release profile of F-CNT does not show any significant difference in different pH, whereas nanohybrid shows a release percentage of 83 and 48 % at pH 5.3 and 7, respectively. Some of the recently reported $MnFe_2O_4$ NPs for drug delivery systems with their loading and release efficiency are summarized in Table 7.

5.5. Catalytic therapies

Currently, a number of treatment modalities are being employed to increase the survival rates of the cancer patients which mainly includes radiotherapy, chemotherapy, magnetic hyperthermia therapy, photodynamic therapy and recently emerged catalytic therapy (CT). CT is a cancer treatment modality based on the generation of reactive oxygen species (ROS) such as the hydroxyl radical using a redox active mixture [210,211]. Even though ascorbic acid has an antioxidant function in the living system, it also acts as pro-oxidant, generating ROS in the presence of transition metal ion. The main concept behind the CT engages a pro-oxidant activity in the existence of transition metal ion [212,213]. As tumor cells have an altered anti-oxidant system they might be highly vulnerable to the oxidative species [214]. Investigations on ROS-based systems such as hypoxanthine oxidase have displayed that administration of ROS leads to cytotoxic effects which only harm the cancer cells and show minimal or non-toxic nature against the healthy cells [215]. The first effort to employ an analogous approach to the CT was reported by Kimoto et al. [216] in 1983, where they demonstrated improvement in the anti-tumor action of the ascorbate by a combination of glycyglycy and copper.

For the enhancement in the effect of ROS-mediated tumor specific therapeutics, different drugs and nanoscale materials such as doxorubicin, Cisplatin, iron oxide, gold NPs, spinel ferrite etc. have been investigated for targeted transportation to tumor cells and endocytosis by tumor tissues to enhance the generation of ROS with high toxicity and selectivity. Nanoscale spinel ferrites have been broadly utilized in the bio-applications such as magnetic hyperthermia, MRI, magnetic targeting, and separation etc. due to their extraordinary magnetic and other properties. In the tumor acidic micro-environment, spinel ferrites display intrinsic peroxidase like activity, which can catalyze the Fenton reaction of hydrogen peroxide (H_2O_2) to generate the hydroxyl-free radicals (ÛOH) with high toxicity, which causes the tumor cell death. Recent investigations in this area have shown that the enzymatic activities of the spinel ferrites can be made superior by translating the exterior magnetic field energy or near-infrared laser energy into as heat energy to generate more ÛOH, which enhances the killing effect of tumor cells. In another manner, with the combination of spinel ferrite with drugs, the generation of the ROS can also be increased to attain more effective cancer therapy. Yan et al. in 2007 investigated that iron oxide NPs possess intrinsic peroxidase-like activity, which catalyzes the disproportionate of H_2O_2 to generate •OH with

Table 7
Summary of reported manganese ferrite NP for drug delivery application.

Nanoparticle	Size nm	Coating	Anticancer or model drug	Drug loading (%)	Drug release (%)	Ref
Mnf@Au	25	Folic acid	Doxorubicin	97.5	76.9	[203]
$MnFe_2O_4$	18	Chitosan	Theophylline			[108]
CNT- $MnFe_2O_4$	200	Chitosan	Doxorubicin	92	83	[131]
pAcDED - $MnFe_2O_4$	8–11	Antimicrobial cationic polyacrylamide	usnic acid		90	[204]
$MnFe_2O_4$	15	Folic acid	Doxorubicin	95		[205]
$MnFe_2O_4$	22	Folic acid and PEG	Doxorubicin	48	59	[133]
PNIPAm-*co*-Am - OA - $MnFe_2O_4$	45	Poly(*N*-isopropylacrylamide-*co*-acrylamide)	Doxorubicin	52	70	[206]
NH_2 – SiO_2 – $MnFe_2O_4$	200	Folic acid	Doxorubicin	60.4	58	[207]
GO/ $MnFe_2O_4$	4–7	Triethylene glycol	Doxorubicin		20	[208]
$MnFe_2O_4$	30–40	Polyethylene glycol-grafted Chitosan	methotrexate	48	25	[209]
$MnFe_2O_4$	8	PVP	Doxorubicin	22.9	40.3	[137]

high toxicity [217]. Further, researchers have accomplished investigations on spinel ferrite NPs a nano-enzyme to mediate the production of ROS for tumor treatments [218]. The mechanism of the adequate ROS generation with high toxicity under the spinel ferrite based catalytic activity and can be summarized as follows: (i) The intrinsic Fenton reaction catalytic activity of spinel ferrites, (ii) Exterior magnetic field energy enhancing the Fenton reaction activity, (iii) The cascade reaction to produce adequate ROS.

Among the spinel ferrites, manganese ferrite ($MnFe_2O_4$) has shown great promise for bio-imaging and catalytic therapies due to their interesting features. Nanoscale $MnFe_2O_4$ has been recently employed in theranostics as a contrast enhancing agents in magnetic resonance imaging (MRI), and as catalase mimicking nanoenzymes for hypoxia mitigation. This capable employment encourages the design and development of novel fabrication approaches to improve the bio-imaging and catalytic properties of these nanomaterials simultaneously for efficient cancer therapy. Kim et al. [219] designed and developed bio-compatible $MnFe_2O_4$ NPs decorated mesoporous SiO_2 NPs (MFMSNs) to conquer hypoxia (Fig. 17), consequently improving the therapeutic efficacy of photodynamic therapy. The exploitation of the constant O^{2-} evolving property of $MnFe_2O_4$ NPs via Fenton reaction, MFMSNs relieved hypoxic conditions using a minimal dosage of NPs and improved the therapeutic outcome of photodynamic therapy for tumors *in vivo*. Their outcomes showed that the constant production of ROS by Fenton reaction under physiological conditions, improves the ROS production of photosensitizers under hypoxic conditions. It was observed that hypoxia drastically reduced after the MFMSNs treatment in both the *in vivo* and *in vitro* models. Systematic inclusion of Ce6 loaded MFMSNs was retained at the tumor region with high selectivity owing to the EPR effect and constantly produced oxygen, facilitating simultaneous reduction of hypoxia, and

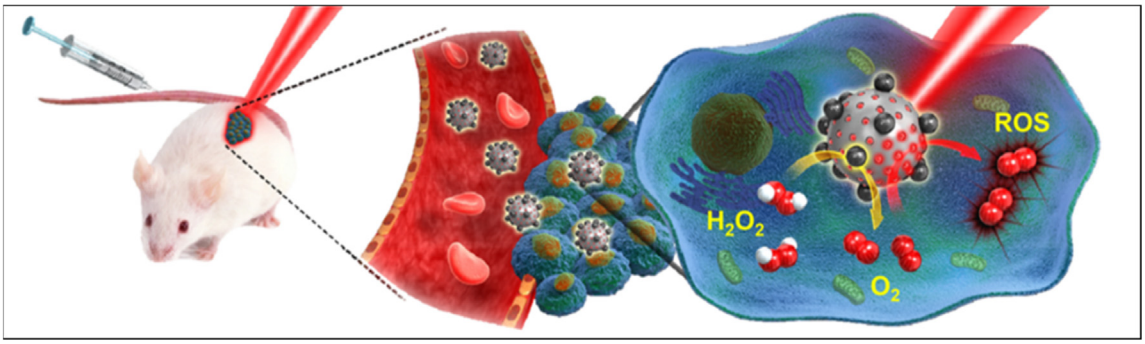

Fig. 17. Schematic illustration of catalytic therapy based on $MnFe_2O_4$ NPs decorated mesoporous SiO_2 NPs (MFMSNs). Adapted and reprinted with permission from reference [219].

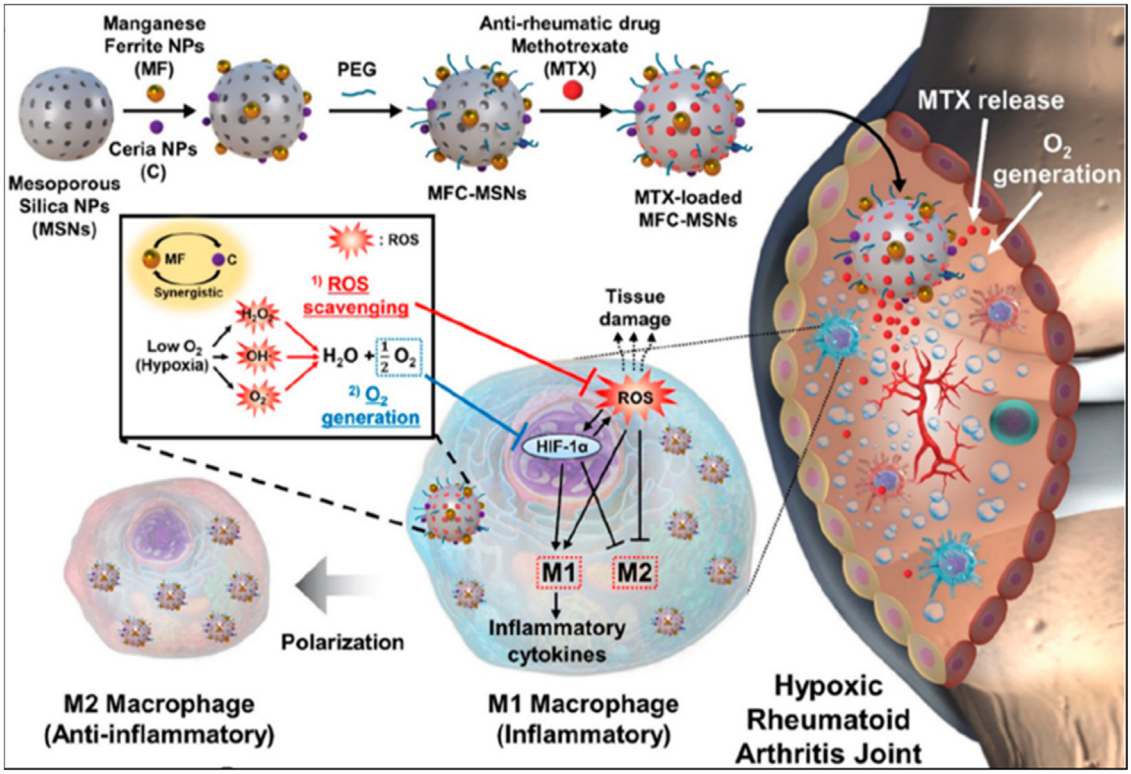

Fig. 18. Therapeutic mechanisms of $MnFe_2O_4$ and ceria nanoparticle-decorated mesoporous silica NPs (MFCMSNs). Adapted and reprinted with permission from reference [221].

improved photodynamic therapy. Their outcomes show a great potential of the MFMSNs for a theranostic candidate in cancer treatments.

Yin et al. [220] reported a novel approach for the continuous and simultaneous regulation of tumor hypoxia and reduction to attain the desired therapeutics. To achieve this approach, they have developed a $MnFe_2O_4$ NPs and metal organic framework (MOF) based biocompatible platform ($MnFe_2O_4$@MOF) by integrating porphyrin coating as a photosensitizer and $MnFe_2O_4$ as nano enzyme. The fabricated $MnFe_2O_4$@MOF platform exhibited catalase-like and peroxidase-like activity. After intervening inside the tumor, the $MnFe_2O_4$@MOF platform continuously catalyzed H_2O_2 to generate the O_2 and overcome tumor hypoxia by cyclic Fenton reaction. $MnFe_2O_4$@MOF platform, along with the Fenton reaction, is capable of determinedly consuming glutathione in the attendance of H_2O_2, which reduced the depletion of ROS upon laser irradiation during photodynamic therapy and attained better therapeutic efficiency *in vivo* and *in vitro*. In addition to this, the $MnFe_2O_4$@MOF platform integrated a treatment modality with MRI to uphold a more accurate and effectual treatment for future clinical applications. Kim et al. [221] in another report developed $MnFe_2O_4$ and ceria nanoparticle-decorated mesoporous silica NPs (MFCMSNs) (Fig. 18) that can considerably scavenge ROS and produces O_2 for improved inflammation via pro-inflammatory M1 macro-phages to anti-inflammatory M2 macro-phages. The synergistic influence of $MnFe_2O_4$ NPs and ceria NPs was analogous to the hydroxyl radicals scavenging effect of ceria NPs, whereas intermediately developed radicals produced by $MnFe_2O_4$ to O_2. MFCMSNs productively induced the M1 to M2 macro-phages under the hypoxia and inflammation condition both *in vivo* and *in vitro*. The outcomes of this study suggest the potentiality of MFCMSNs as an inflammatory reliever and M2 macro-phages stimulator for the efficient treatment of hypoxia associated inflammatory disorders.

6. Targeting strategies

Currently, chemotherapy and HPT have been increasingly used in treating cancers. However, the major side effects caused by those therapies are that they kill not only the cancer cells but also the health surrounding non-diseased cells/tissues. An improvement strategy to overcome this off-target toxic effect is to use a targeted delivery system. This can deliver therapeutic agents directly into the cancer site and reduce the dosage level. MNPs are used as a targeting agent because they can be guided to a specific location by the external AMF due to their superparamagnetic behavior. However, the major limitation is that MNPs tend to agglomerate in an aqueous solution. This could be solved by surface modification using some viral or non-viral vectors on the surface of MNPs. The use of viral vectors like adenoviruses is limited due to their viral recombination, immunogenicity and toxicity

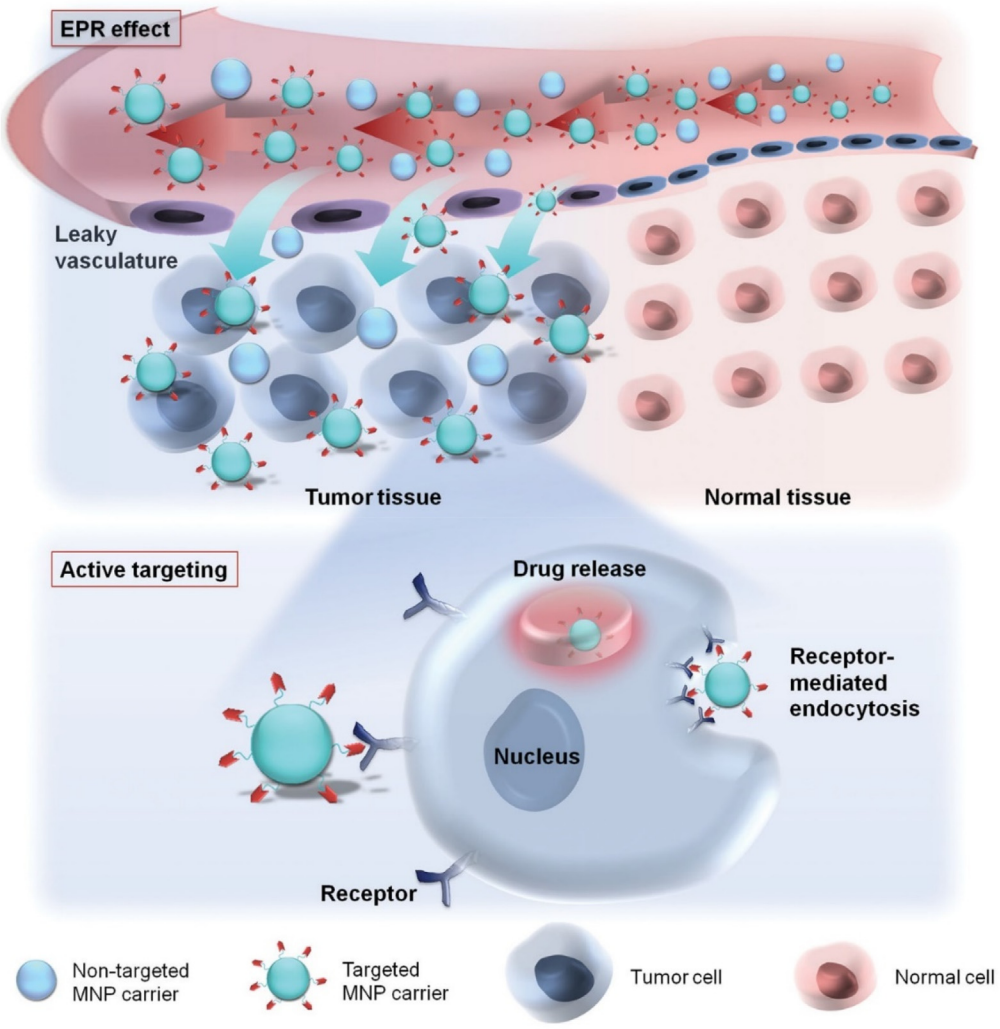

Fig. 19. Targeted NP delivery system to the tumor tissue via the EPR effect. Adapted and reprinted with permission from reference [223].

[222]. The commonly used surface modifications include non-viral vectors such as polymers, inorganic NPs, and liposomes. These materials should be non-toxic and biocompatible and should have sufficient hydrophilicity by maintaining homogeneous water suspension. Generally, the MNPs get accumulated at the tumor sites through active (by external magnetic field) or passive (enhanced permeability and retention (EPR) effect) targeting, as shown in Fig. 19 [223]. However, the surface coating on the MNPs and the magnetic field guided tumour-targeting alone is not always sufficient due to the significant variation between and within the tumor types [224]. An alternative action for improving the targeting performance is by conjugating the MNPs with targeting segments like antibodies, transferrin, hyaluronic acid, aptamers, peptides, and folates to recognize specific receptor/integrin on the tumor surface.

Antibodies are glycoproteins belonging to the immunoglobulin family. They have a higher affinity to several receptors or antigens on the surface of cancer cells, including vascular endothelial growth factor receptor (VEGF), PSMA (prostate-specific membrane antigen), hyaluronan receptor (CD44), epidermal growth factor receptor (EGFR) and human epidermal receptor-2 (HER-2) [225]. For selective targeting on tumor cells, these antibodies are attached with NPs. There are several antibodies used for cancer targeting, like anti-EGFR and anti-VEGF. anti-EGFR antibodies include HER1 (EGFR and ErbB 1), HER2 and HER3 (ErbB 3) and HER4 (ErbB 4) [226]. For example, HER2 is a tumor biomarker that correlates with 7–34 % of gastric cancers,16–29 % of breast cancers and approximately 30 % of salivary duct carcinomas that can be used for tumor targeting [227]. Yoon et al. [228] developed Fe@$MnFe_2O_4$ MNP with high magnetization and with increased core size. The particle was tested for transverse relaxivity at 7 T, and cellular detection were performed on human cancer cells (SkBr3) with HER2/neu antibodies conjugated NPs, and the results confirmed the superior detection of cancer cells. VEGF is a signaling protein for cancer vasculogenesis and angiogenesis [229]. anti-VEGF monoclonal antibodies such as bevacizumab, aflibercept and anti-VEGFR2 have been used as drug delivery systems to control the progression of vascular-related diseases. In addition to anti- EGFR and VEGF other antibodies such as anti-TAG-72, anti-CD 22, anti-CD133, anti-prostate-specific membrane antigen (PSMA), anti- αv β3, and monoclonal antibody A7 have also shown targeting properties while having less immunogenicity.

Aptamers are single-stranded oligonucleotides, which can readily combine with small molecules like oligonucleotide, DNA, or RNA to the tumor surface with high affinity. Aptamers show better performance than antibodies with high selective and specific target recognition. They are mainly used due to their advantageous properties like stability, flexible structure, low toxicity, rapid tissue penetration and their ability to mimic the natural properties of antibodies. Some of the aptamers used by scientists are MUC-1 (5TR1 aptamer targets mucin-1), PSMA, A10 RNA, and A10-3-J1 for diagnostic and therapeutic purposes [230–232]. Another tumor targeting conjugate is Transferrin (Tf), an important tumor-targeting ligand is a blood plasma glycoprotein, which helps in the transport of Fe ions and has low immunogenicity. It has a high affinity to the Tf receptor (TfR) found on diverse tumor cells, most notably breast cancer cells. Tf-conjugated delivery systems are successfully employed in phase I/II clinical trials of cancer therapy such as MBP-426 (TfR-targeted liposomal formulation of oxaliplatin designed by Mebiopharm), SGT-94 (RB94 gene encapsulated by a liposome targeting the TfR single-chain antibody fragment), and SGT-53 (an intravenous, tumor-targeted liposomal p53 deliv-

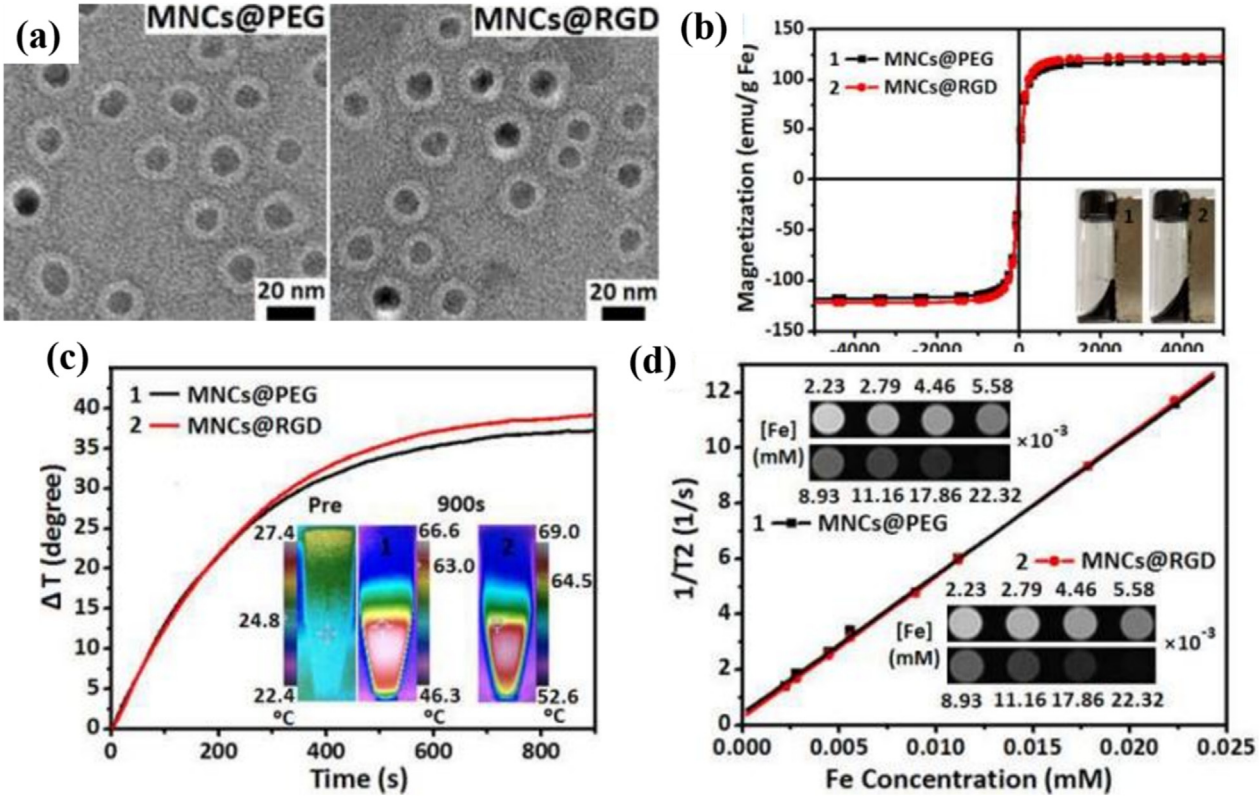

Fig. 20a. (i). (a) TEM images of MNP, (b) Hysteresis loops of MNPs, (c) Time – temperature curves of MNCs in aqueous phase (2 mg Fe/mL) and the corresponding *in vitro* thermal images under ACMF (390 kHz, 2.58 kA m^{-1}), (d) T_2-weighted MR images and relaxation time of MNPs by a 1.5 T MR scanner, (e) Magnetically induced cancer theranostics combining MRI and hyperthermia, (f) Fluorescence images of mice bearing breast cell carcinoma (4 T1) acquired after the intravenous injection and (g) Photographs of the mouse. Adapted and reprinted with permission from reference [238].

ery system) [233]. Tf is also used for selective transfer of therapeutic drugs (such as DOX, paclitaxel (PTX), and cisplatin) [234] or genes (such as CYP2B1, ETR, and LacZ) into the cancer cells [235].

7. Pre-clinical *in vivo* studies

For the potential clinical applications of the prepared manganese ferrites, a proper assessment of their toxicological properties must be studied. Extensive evaluation needs to be done to the dosage and the possible side effects. In general, ferrites are known to cause ROS production leading to cell death by DNA damage [236]. Thus, several *in vitro* and *in vivo* studies must be taken before the clinical trial to assess the material's biocompatibility. The commonly used *in vitro* techniques to evaluate the cytotoxicity of the material are MTT assays, TPB assay, measuring lactate dehydrogenase (LDH) and mitochondrial redox activity. These tests provide an initial impression of the prepared NP and their biocompatibility for future use in biomedical applications. The *in vivo* assessment is used to find the material's particle distribution, cellular accumulation, and organ deposition. In general, ferrites accumulate more in the liver and the spleen when administered intravenously as these tissues have high vascularization [237]. The mouse model for *in vivo* toxicity testing is extensively used as an intermediate model before the clinical trials. These provide relatively high throughput but are expensive and ethical permissions are needed. Nica et al. synthesized PEGlayted coated core–shell structure of cobalt ferrite and manganese ferrite ($CoFe_2O_4$@$MnFe_2O_4$) by thermal decomposition method as a potential theranostics agent for MRI and hyperthermia applications. Bimagnetic NPs had an average particle diameter of 14.4 ± 2.4 nm with saturation magnetization (M_S) of 64.2 emu g^{-1} and SAR values in the range of 210–320 W g^{-1}. The magnetic relaxivity (r_1 and r_2) measurements at 1.5 T and 9.4 T were calculated in PBS solution at different concentration; the transverse relaxivity (r_2) was 30.2 $mM^{-1}s^{-1}$ and 67.6 $mM^{-1}s^{-1}$ at 1.5 T and 9.4 T, respectively. Further, they had carried out an *in vivo* MRI study on the 9.4 T Bruker system in male Balb/c mice. They have administered NPs intravenously at a concentration of 10 mg/kg of the mice body weight. MRI showed a rapid increment of 50 % in the liver in the first 30 mins, and the slow increment of 20 % after 30 min and remained at the basal level. This proved that PEGylated coated NP has good stealth property with high circulating time. Similarly, the kidney showed a rapid increase of 40 % in the first 30 mins, then returned to the basal levels and remained the same for the entire study. T_1 and T_2 - weighted images were taken at different time intervals shows that $CoFe_2O_4$@$MnFe_2O_4$ can be used as a MRI contrast agent. In another study by Xie et al. [238], PEG-phospholipid and tripeptide arginine-glycine-aspartic acid (RGD) coated Mn–Zn ferrite with a core size of 14 nm was synthesized, which was used as a contrast agent for multimodal imaging and hyperthermia (Fig. 20i(**a**)). The NPs MNCs@PEG and MNCs@RGD show high magnetization M_S values at room-temperature of 112 and 115 emu g^{-1}, respectively (Fig. 20i(**b**)). The prepared particles were subjected to the applied AC magnetic field of 2.58 kA m^{-1}, 390 kHz. MNCs@PEG and MNCs@RGD NPs possess high SAR values of 498 and 532 W g^{-1} at 2 mg mL^{-1} concentration, respectively (Fig. 20i(**c**)). The *in vitro* studies carried out at 1.5 T MR shows

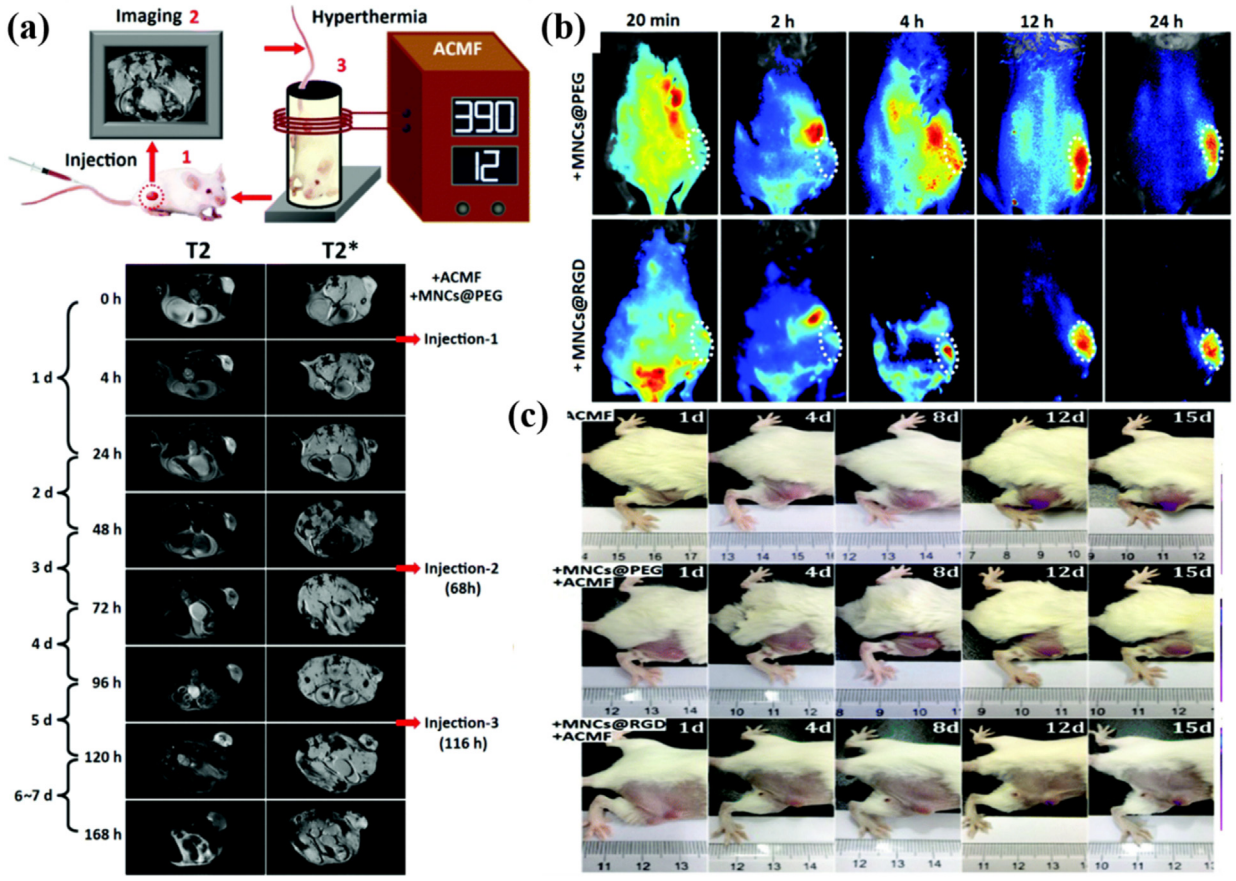

Fig. 20b. (ii). (a) Magnetically induced cancer theranostics combining MRI and hyperthermia, (b) Fluorescence images of mice bearing breast cell carcinoma (4 T1) acquired after the intravenous injection and (c) Photographs of the mouse. Adapted and reprinted with permission from reference [238].

concentration-dependent T_2 effect and the corresponding r_2 relaxivity values of MNCs@PEG and MNCs@RGD NPs are 485 and 501 $mM^{-1}s^{-1}$, respectively (Fig. 20i**(d)**). In this study, MNCs@RGD showed superior SAR and T_2 relaxivity due to the surface polypeptide's cross-linking effect. They had used a mouse model bearing breast carcinoma (4 T1) for fluorescence/magnetic resonance (MR) as diagnostics and magnetic hyperthermia as treatment under an alternating magnetic field of 2.58 kA m^{-1}, 390 kHz. They had used 30 mg Fe per kg body weight for studies, and for *in vivo* fluorescence imaging, they have incorporated indocyanine green (ICG) dye in the NP. They showed intense fluorescence over 0–2 h after the injection and signals gradually enhanced and maintained for 24 h. They had also taken T_2*-weighted MR images over time range of 0–96 h. The obvious dark contrast was seen in the tumor region after 4 h post-injection. After 24–48 h the tumor area was highlighted suggesting the accumulation of large number of particles. The contrast existing as long as 96 h in the tumor regions shows NPs possess the imaging ability of prolonged tumor targeting *in vivo*. Further, they had conducted magnetic hyperthermia studies with the dosage of 30 μg Fe per g body weight for three times. An alternating magnetic field of 2.58 kA m^{-1} at 390 kHz was applied for 30 min over seven days at the tumor site. MRI was used as a diagnostics technique to locate the tumor suppression, as shown in Fig. 20**ii**. To evaluate the ability of the prepared magnetic particle to escape the RES, specific targeting and therapeutic properties, several studies have been carried out [147,219,239–241].

8. Prospect of the clinical transformation of $MnFe_2O_4$ nanomaterials

Over the last two decades, nanomaterials played an important role in the commercialization of nanomedicines. Certainly, we might expect to generate new breakthroughs and prospects for the global economy from the advancements in nanotechnology based medicines. With the potentiality for widespread applications of $MnFe_2O_4$ nanomaterials in the upcoming years, it may broadly be employed in various areas, especially in cancer diagnostics and therapeutics. $MnFe_2O_4$ nanomaterials are promising for clinical cancer diagnosis and therapeutics based on their size, biocompatibility, surface chemistry, superior stability and tunable toxicity in biological systems. It is highly expected that $MnFe_2O_4$ nanomaterials used in cancer tumor therapy will significantly improve the existing cancer cell detection, imaging and therapy methods while reducing the side effects and toxicity compared with conventional tumor treatments. However, several issues need to be addressed, and there are still some controversies about the potential risk of anti-cancer therapies based on nanomaterials [242–244]. The most crucial issues are potential chronic and acute toxic effects which cannot be neglected in anti-cancer therapies [245,246]. It is essential to perform detailed toxicity studies to affirm the safety prior to clinical use in humans. Moreover, only a few types of magnetic materials based on iron oxide nanomaterials have been granted by the FDA and very few nanomaterials have been approved as anticancer agents to enter the Phase III clinical trials or for commercialization, which shows that $MnFe_2O_4$ nanomaterials need to be understood thoroughly before applying them in tumor therapies. Thus, the long-term toxicity of $MnFe_2O_4$ nanomaterials to living systems needs to be intensively investigated. Developing cancer tumor therapies is a multidisciplinary field. With more in detail investigations of tumor biology, tumor immunology, molecular biology and nanomaterials, an ideal therapy will eventually be produced for tumour treatment. The transformation of $MnFe_2O_4$ nanomaterials into a routine clinical practice will require a multi-disciplinary approach directed by clinical, ethical and social perceptions. Given the notable research studies being dedicated to the field, it might be expected that human beings will greatly be benefited from nanomaterials in the near future, especially for tumor therapies.

9. Concluding remarks and outlook

$MnFe_2O_4$ NPs possess wide-ranging unique and attractive properties, including improved magnetic behavior, high chemical stability, and excellent biocompatibility, explaining their extensive use in biomedical research in recent years. Mostly, the co-precipitation approach is adopted to synthesize nanospheres. At the same time, both thermal decomposition and solvothermal techniques are employed to grow spherical and anisotropic particles having a good degree of monodispersity. The precursors, including the manganese salts, solvent to surfactant ratio and reaction conditions such as temperature, reaction time, heating rate etc., firmly dictate the morphology, purity, and crystallinity of these nanomaterials. The choice of the synthesis technique and the corresponding parameters majorly affect the transverse relaxivity and specific absorption rate of $MnFe_2O_4$ NPs. Interestingly, $MnFe_2O_4$ NPs exhibit size-dependent saturation magnetization mostly in the range of $\sim$ 40–80 emu g^{-1} at room temperature, which is very close or sometimes higher than the M_S reported for superparamagnetic Fe_3O_4 nanoparticles ($\sim$65–70 emu g^{-1} for 12 nm sized particles)[41,247]. The higher magnetic saturation and superparamagnetism exhibited by these particles make them an efficient candidate for MRI and magnetic hyperthermia applications. The anisotropic $MnFe_2O_4$ nanostructures like cubes, rods etc. always exhibit a substantially higher magnitude of M_S due to the introduction of shape and surface anisotropies in the spinel system. Furthermore, the cell viability studies performed on both human and mouse cancer cell lines with $MnFe_2O_4$ suggest no significant toxicity of these particles, thus confirming their biocompatibility. $MnFe_2O_4$ NPs depending on the size and morphology, have been employed both as T_1 and T_2 contrast agents for MRI. While most studies have reported high values of r_2 relaxivity with $MnFe_2O_4$, as high as $\sim$ 350–400 $mM^{-1}s^{-1}$, ultrasmall manganese ferrite particles have diameter in the range of 2–3 nm have displayed much improved performance as T_1 contrast agents. Furthermore, depending upon the morphology of NPs, $MnFe_2O_4$ exhibits high heating efficiency, becoming an ideal candidate in magnetic hyperthermia-mediated cancer therapy. Individual NPs, core–shell structures and nanocomposites based on $MnFe_2O_4$ display considerable values of SAR and greatly improved hyperthermia performance in order to restrict and eliminate the growth of cancerous cells/tissues. The SAR is reported to be much pronounced in anisotropic structures, particularly in nanoclusters in the range of $\sim$ 1200 W g^{-1}. The performance of these nanostructures as novel drug carriers for targeted delivery and controlled release of anticancer drug molecules ($\sim$80 – 90 %) are also commendable. Combining magnetic hyperthermia simultaneously with chemotherapeutic strategies as a synergistic mode of treatment modality is a possible area of research that still requires much attention specifically involving $MnFe_2O_4$ based NPs and nanocomposites.

There are not many reports available on $MnFe_2O_4$ NPs-based pre-clinical studies. Consequently, much more intricate and systematic studies must be conducted for the practical realization of these NPs in medical sciences and technology. Also, from the point of fundamental physics, $MnFe_2O_4$ nanostructures are yet to be explored. The concepts like blocking temperature [248–250], interparticle interactions [251–253], spin relaxation dynamics [248,249,254], exchange bias effects [255–257], *ac* susceptibility

studies [248,249,258] etc., involving both spherical and anisotropic particles and composites of $MnFe_2O_4$ must be dealt in an organized way which may provide a deeper understanding in further exploring these materials for advanced biomedical applications. Moreover, the properties of these nanomaterials can be tailored accordingly by introducing suitable dopants in the spinel structure. The dopants, particularly rare earths, can strongly influence the morphological and magnetic properties which may ultimately impact hyperthermia heating, r_1-r_2 relaxivities and drug delivery efficiency of these nanostructures [259–261]. Furthermore, it is of utmost importance to design and develop engineered nanomaterials and nanocomposites based on $MnFe_2O_4$ to address major biomedical concerns. Typically, $MnFe_2O_4$ NPs after entering the cells *via* phagocytosis get trapped inside the vesicles, known as endosomes [262], and a very less percentage of these drug delivery vehicles can actively get involved in cell apoptosis [263]. Therefore, new functionalization strategies and morphological modifications involving $MnFe_2O_4$ must be employed to maximize their endosomal escape for efficient targeting and controlled release of drug molecules at the site of action in a safe manner. In summary, it is hoped that $MnFe_2O_4$ NPs, if rigorously studied and explored, can have a tremendous future ahead, particularly to modernize and advance the emerging field of cancer nanomedicine.

Data availability

No data was used for the research described in the article.

Declaration of Competing Interest

The authors declare that they have no known competing financial interests or personal relationships that could have appeared to influence the work reported in this paper.

References

[1] J. Ferlay, M. Colombet, I. Soerjomataram, D. M. Parkin, M. Piñeros, A. Znaor and F. Bray, Int. J. Cancer (2021).
[2] G.M. Cooper, R.E. Hausman, The Cell: A Molecular Approach, ASM Press, 2004.
[3] V.K. Chaturvedi, A. Singh, V.K. Singh, M.P. Singh, Curr. Drug Metab. 20 (6) (2019) 416–429.
[4] M. Cordani, Á. Somoza, Cell. Mol. Life Sci. 76 (7) (2019) 1215–1242.
[5] E.R. Evans, P. Bugga, V. Asthana, R. Drezek, Mater. Today 21 (6) (2018) 673–685.
[6] S.S. Laha, A.R. Naik, E.R. Kuhn, M. Alvarez, A. Sujkowski, R.J. Wessells, B.P. Jena, Nano Lett. 17 (2) (2017) 1262–1268.
[7] J. Panyam, V. Labhasetwar, Adv. Drug Deliv. Rev. 55 (3) (2003) 329–347.
[8] Y. Song, D. Li, Y. Lu, K. Jiang, Y. Yang, Y. Xu, L. Dong, X. Yan, D. Ling, X. Yang, Natl. Sci. Rev. 7 (4) (2020) 723–736.
[9] M.M. Yallapu, S.F. Othman, E.T. Curtis, B.K. Gupta, M. Jaggi, S.C. Chauhan, Biomaterials 32 (7) (2011) 1890–1905.
[10] Y. Yao, Y. Zhou, L. Liu, Y. Xu, Q. Chen, Y. Wang, S. Wu, Y. Deng, J. Zhang, A. Shao, Frontiers in Molecular Biosciences 7 (2020).
[11] H. Lee, T.-H. Shin, J. Cheon, R. Weissleder, Chem. Rev. 115 (19) (2015) 10690–10724.
[12] M. Yang, L. Gao, K. Liu, C. Luo, Y. Wang, L. Yu, H. Peng, W. Zhang, Talanta 131 (2015) 661–665.
[13] C.-H. Sohn, S.P. Park, S.H. Choi, S.-H. Park, S. Kim, L. Xu, S.-H. Kim, J.A. Hur, J. Choi, T.H. Choi, Nanomed.: Nanotechnol. Biol. Med. 11 (1) (2015) 127–135.
[14] S. Kumar, A. Daverey, V. Khalilzad-Sharghi, N.K. Sahu, S. Kidambi, S.F. Othman, D. Bahadur, RSC Adv. 5 (2015) 53180–53188.
[15] A. Avasthi, C. Caro, E. Pozo-Torres, M.P. Leal, M.L. García-Martín, Top. Curr. Chem. 378 (3) (2020) 40.
[16] L.H. Reddy, J.L. Arias, J. Nicolas, P. Couvreur, Chem. Rev. 112 (11) (2012) 5818–5878.
[17] V.V. Mody, A. Cox, S. Shah, A. Singh, W. Bevins, H. Parihar, Applied Nanoscience 4 (4) (2014) 385–392.
[18] B. Halamoda Kenzaoui, S. Angeloni, T. Overstolz, P. Niedermann, C. Chapuis Bernasconi, M. Liley, L. Juillerat-Jeanneret, ACS Appl. Mater. Interfaces 5 (9) (2013) 3581–3586.
[19] E. kianfar,, J. Supercond. Novel Magn. 34 (7) (2021) 1709–1735.
[20] M.P. Arachchige, S.S. Laha, A.R. Naik, K.T. Lewis, R. Naik, B.P. Jena, Micron 92 (2017) 25–31.
[21] S.V. Spirou, M. Basini, A. Lascialfari, C. Sangregorio, C. Innocenti, Nanomaterials (Basel) 8 (6) (2018) 401.
[22] A. Rajan S, M. Sharma and N. Sahu,, J. Supercond. Novel Magn. (2019).
[23] H. Fatima, T. Charinpanitkul, K.-S. Kim, Nanomaterials 11 (5) (2021) 1203.
[24] B.D. Plouffe, S.K. Murthy, L.H. Lewis, Rep. Prog. Phys. 78 (1) (2014) 016601.
[25] H. Fatima, K.-S. Kim, Korean J. Chem. Eng. 34 (3) (2017) 589–599.
[26] S.P. Schwaminger, P. Fraga-García, M. Eigenfeld, T.M. Becker, S. Berensmeier, Front. Bioeng. Biotechnol. 7 (2019) 233.
[27] Y. Xu, E. Wang, Electrochim. Acta 84 (2012) 62–73.
[28] J.-H. Lee, J.-W. Kim, M. Levy, A. Kao, S.-H. Noh, D. Bozovic, J. Cheon, ACS Nano 8 (7) (2014) 6590–6598.
[29] M. Iranifam, TrAC, Trends Anal. Chem. 51 (2013) 51–70.
[30] A. Ali, T. Shah, R. Ullah, P. Zhou, M. Guo, M. Ovais, Z. Tan, Y. Rui, Front. Chem. 9 (2021) 548.
[31] A.K. Gupta, M. Gupta, Biomaterials 26 (18) (2005) 3995–4021.
[32] M. Irfan Hussain, M. Xia, Xiao-NaRen, K. Akhtar, A. Nawaz, S. K. Sharma and Y. Javed, in *Magnetic Nanoheterostructures: Diagnostic, Imaging and Treatment*, edited by S. K. Sharma and Y. Javed (Springer International Publishing, Cham, 2020), pp. 243-265.
[33] S. Kumar, A. Daverey, N.K. Sahu, D. Bahadur, J. Mater. Chem. B 1 (30) (2013) 3652–3660.
[34] N.K. Sahu, J. Gupta, D. Bahadur, Dalton Trans. 44 (19) (2015) 9103–9113.
[35] A. Khan and N. Kumar Sahu, (1751-875X (Electronic)).
[36] A. Rajan, M. Sharma, N.K. Sahu, Sci. Rep. 10 (1) (2020) 15045.
[37] A. Rajan, N.K. Sahu, ACS Applied Nano Materials 4 (5) (2021) 4642–4653.
[38] B. Ding, S. Shao, F. Jiang, P. Dang, C. Sun, S. Huang, P. a. Ma, D. Jin, A. A. A. Kheraif and J. Lin,, Chem. Mater. 31 (7) (2019) 2651–2660.
[39] L.S. Lin, J. Song, L. Song, K. Ke, Y. Liu, Z. Zhou, Z. Shen, J. Li, Z. Yang, W. Tang, G. Niu, H.H. Yang, X. Chen, Angew. Chem. Int. Ed. Engl. 57 (18) (2018) 4902–4906.
[40] S.S. Laha, R.J. Tackett, G. Lawes, Physica B 448 (2014) 69–72.
[41] S. Laha, R. Regmi, G. Lawes, J. Phys. D Appl. Phys. 46 (32) (2013) 325004.
[42] J.M.D. Coey, Magnetism and Magnetic Materials, Cambridge University Press, Cambridge, 2010.
[43] D.S. Mathew, R.-S. Juang, Chem. Eng. J. 129 (1) (2007) 51–65.
[44] A. V. Samrot, C. S. Sahithya, J. Selvarani A, S. K. Purayil and P. Ponnaiah, Current Research in Green and Sustainable, Chemistry 4 (2021) 100042.
[45] Y. Xiao, J. Du, J. Mater. Chem. B 8 (3) (2020) 354–367.
[46] S.D. Anderson, V.V. Gwenin, C.D. Gwenin, Nanoscale Res. Lett. 14 (1) (2019) 188.
[47] N.V.S. Vallabani, S. Singh, 3,, Biotech 8 (6) (2018) 279.
[48] G.S. Demirer, A.C. Okur, S. Kizilel, J. Mater. Chem. B 3 (40) (2015) 7831–7849.
[49] W. Wu, Z. Wu, T. Yu, C. Jiang, W.-S. Kim, Sci. Technol. Adv. Mater. 16 (2) (2015) 023501.
[50] N.D. Thorat, H. Townely, G. Brennan, A.K. Parchur, C. Silien, J. Bauer, S.A. Tofail, ACS Biomater. Sci. Eng. 5 (6) (2019) 2669–2687.
[51] N.D. Thorat, S.A. Tofail, B. von Rechenberg, H. Townley, G. Brennan, C. Silien, H.M. Yadav, T. Steffen, J. Bauer, Appl. Phys. Rev. 6 (4) (2019) 041306.
[52] N. Akhlaghi, G. Najafpour-Darzi, J. Ind. Eng. Chem. 103 (2021) 292–304.
[53] Z. Surowiec, M. Budzyński, K. Durak, G. Czernel, Nukleonika 62 (2) (2017) 73.
[54] P. Puspitasari, H. Suryanto, A. Doko, High Temperature Material Processes: An International Quarterly of High-Technology Plasma Processes 22 (2018).
[55] J. Watt, G.C. Bleier, M.J. Austin, S.A. Ivanov, D.L. Huber, Nanoscale 9 (20) (2017) 6632–6637.
[56] R. Deshmukh, M. Niederberger, Chemistry – A,, European Journal 23 (36) (2017) 8542–8570.
[57] G. Chen, J. Wang, L. Zhou, W. Ma, D. Zhang, F. Ren, H. Yan, G. Qiu, X. Liu, J. Am. Ceram. Soc. 95 (11) (2012) 3569–3576.
[58] B. Aslibeiki, P. Kameli, M. Ehsani, H. Salamati, G. Muscas, E. Agostinelli, V. Foglietti, S. Casciardi, D. Peddis, J. Magn. Magn. Mater. 399 (2016) 236–244.
[59] V. Patsula, L. Kosinová, M. Lovrić, L. Ferhatovic Hamzić, M. Rabyk, R. Konefal, A. Paruzel, M. Šlouf, V. Herynek, S. Gajović, D. Horák, ACS Appl. Mater. Interfaces 8 (11) (2016) 7238–7247.
[60] F.X. Redl, C.T. Black, G.C. Papaefthymiou, R.L. Sandstrom, M. Yin, H. Zeng, C.B. Murray, S.P. O'Brien, J. Am. Chem. Soc. 126 (44) (2004) 14583–14599.
[61] H. Zeng, P.M. Rice, S.X. Wang, S. Sun, J. Am. Chem. Soc. 126 (37) (2004) 11458–11459.
[62] H. Yang, C. Zhang, X. Shi, H. Hu, X. Du, Y. Fang, Y. Ma, H. Wu, S. Yang, Biomaterials 31 (13) (2010) 3667–3673.
[63] M. Stoia, C. Păcurariu, E.-C. Muntean, J. Therm. Anal. Calorim. 127 (1) (2017) 155–162.
[64] J. Kwon, J.-H. Kim, S.-H. Kang, C.-J. Choi, J.A. Rajesh, K.-S. Ahn, Appl. Surf. Sci. 413 (2017) 83–91.
[65] M.L. Bruschi, L. d. A. S. de Toledo,, Magnetochemistry 5 (3) (2019) 50.
[66] A. Kumar, Y. Kuang, Z. Liang, X. Sun, Materials Today Nano 11 (2020) 100076.
[67] M.B. Gawande, S.N. Shelke, R. Zboril, R.S. Varma, Acc. Chem. Res. 47 (4) (2014) 1338–1348.
[68] A.V. Nikam, B.L.V. Prasad, A.A. Kulkarni, CrystEngComm 20 (35) (2018) 5091–5107.
[69] H. Hu, H. Yang, P. Huang, D. Cui, Y. Peng, J. Zhang, F. Lu, J. Lian, D. Shi, Chem. Commun. 46 (22) (2010) 3866–3868.
[70] L. Yang, L. Ma, J. Xin, A. Li, C. Sun, R. Wei, B.W. Ren, Z. Chen, H. Lin, J. Gao, Chem. Mater. 29 (7) (2017) 3038–3047.
[71] X. Hou, J. Feng, X. Xu, M. Zhang, J. Alloy. Compd. 491 (1) (2010) 258–263.

[72] H.-J. Cui, J.-W. Shi, B. Yuan, M.-L. Fu, J. Mater. Chem. A 1 (19) (2013) 5902–5907.
[73] D. Lisjak, A. Mertelj, Prog. Mater Sci. 95 (2018) 286–328.
[74] H.-M. Song, J.I. Zink, N.M. Khashab, The Journal of Physical Chemistry C 119 (19) (2015) 10740–10748.
[75] A. Vernekar, T. Das, S. Ghosh, G. Mugesh, Chem. Asian J. 11 (2015).
[76] Y. Oh, N. Lee, H.W. Kang, J. Oh, Nanotechnology 27 (11) (2016) 115101.
[77] A. Ullrich, M.M. Rahman, P. Longo, S. Horn, Sci. Rep. 9 (1) (2019) 19264.
[78] K.-W. Wang, W.-J. Shen, Mater. Lett. 277 (2020) 128284.
[79] K. Chandunika R, V. Rajagopalan and N. K. Sahu,, IET Nanobiotechnol. 14 (9) (2020) 823–829.
[80] Z. Chen, X. Sun, Z. Ding, Y. Ma, J. Mater. Sci. Technol. 34 (5) (2018) 842–847.
[81] B.D. Cullity, C.D. Graham, Introduction to Magnetic Materials, (Wiley-IEEE Press, 2008.
[82] G. Goya and V. Raffa, (2018), pp. 395.
[83] K. Wu, L. Tu, D. Su, J.-P. Wang, J. Phys. D Appl. Phys. 50 (2017) 085005.
[84] M. Darbandi, F. Stromberg, J. Landers, N. Reckers, B. Sanyal, W. Keune, H. Wende, J. Phys. D Appl. Phys. 45 (19) (2012) 195001.
[85] A. Demortière, P. Panissod, B.P. Pichon, G. Pourroy, D. Guillon, B. Donnio, S. Bégin-Colin, Nanoscale 3 (1) (2011) 225–232.
[86] I.H. Lone, J. Aslam, N.R.E. Radwan, A.H. Bashal, A.F.A. Ajlouni, A. Akhter, Nanoscale Res. Lett. 14 (1) (2019) 142.
[87] R.A. Pawar, S.M. Patange, A.R. Shitre, S.K. Gore, S.S. Jadhav, S.E. Shirsath, RSC Adv. 8 (44) (2018) 25258–25267.
[88] S. Kane, M. Satalkar, J. Mater. Sci. 52 (2017).
[89] H. T. Diep, *Theory of Magnetism*.
[90] T. Tatarchuk, M. Bououdina, J. Vijaya and L. Kennedy (2017) 305–325.
[91] S. Chikazumi, C. D. Graham and S. Chikazumi, (Oxford University Press, Oxford; New York, 1997).
[92] F.G.D. Silva, J. Depeyrot, A.F.C. Campos, R. Aquino, D. Fiorani, D. Peddis, J. Nanosci. Nanotechnol. 19 (8) (2019) 4888–4902.
[93] C.-G. Stefanita, Magnetism: Basics and Applications, 1 ed., Springer, Berlin, Heidelberg, 2012.
[94] R.S. de Biasi, L.H.G. Cardoso, Physica B 407 (18) (2012) 3893–3896.
[95] A. Kumar, S. Fähler, H. Schlörb, K. Leistner, L. Schultz, Physical Review B 73 (6) (2006) 064421.
[96] M.K. Gupta, D.D. Kulkarni, R. Geryak, S. Naik, V.V. Tsukruk, Nano Lett. 13 (1) (2013) 36–42.
[97] H. Schlörb, V. Haehnel, M.S. Khatri, A. Srivastav, A. Kumar, L. Schultz, S. Fähler, physica status solidi (b) 247 (2010) 2364–2379.
[98] . (International Bank for Reconstruction and Development / The World Bank., Washington DC, 2015).
[99] M. Amiri, M. Salavati-Niasari, A. Akbari, Adv. Colloid Interface Sci. 265 (2019) 29–44.
[100] K.M. Krishnan, IEEE Trans. Magn. 46 (7) (2010) 2523–2558.
[101] M. Pernia Leal, S. Rivera-Fernández, J.M. Franco, D. Pozo, J.M. de la Fuente, M. L. García-Martín, Nanoscale 7 (5) (2015) 2050–2059.
[102] M. Hjiri, S. Alshammari, H. Besbes, O.M. Lemine, A. Hammad, M. s. Aida,, Mater. Res. Express (2019).
[103] I. M. Obaidat, B. Issa and Y. Haik, Nanomaterials (Basel) 5 (1), 63-89 (2015).
[104] Y.W. Jun, J.W. Seo, J. Cheon, Acc. Chem. Res. 41 (2) (2008) 179–189.
[105] Z. Li, S. Wang, Q. Sun, H. Zhao, H. Lei, M. Lan, Z. Cheng, X. Wang, S. Dou, M. Lu, Adv. Healthcare Mater. 2 (2013).
[106] A. Banerjee, B. Blasiak, E. Pasquier, B. Tomanek, S. Trudel, RSC Adv. 7 (61) (2017) 38125–38134.
[107] J. Klostergaard, C.E. Seeney, Nanomedicine: Nanotechnology, Biology and Medicine 8 (2012) S37–S50.
[108] D.-H. Kim, D.E. Nikles, C.S. Brazel, Materials (Basel) 3 (7) (2010) 4051–4065.
[109] S. Faraji, G. Dini, M. Zahraei, J. Magn. Magn. Mater. 475 (2019) 137–145.
[110] M. Colombo, S. Carregal-Romero, M.F. Casula, L. Gutiérrez, M.P. Morales, I.B. Böhm, J.T. Heverhagen, D. Prosperi, W.J. Parak, Chem. Soc. Rev. 41 (11) (2012) 4306–4334.
[111] S. Ali, S.A. Khan, Z.H. Yamani, M.T. Qamar, M.A. Morsy, S. Sarfraz, Applied Nanoscience 9 (4) (2019) 479–489.
[112] S. He, H. Zhang, Y. Liu, F. Sun, X. Yu, X. Li, L. Zhang, L. Wang, K. Mao, G. Wang, Y. Lin, Z. Han, R. Sabirianov, H. Zeng, Small 14 (29) (2018) 1800135.
[113] J.-H. Lee, Y.-M. Huh, Y.-W. Jun, J.-W. Seo, J.-T. Jang, H.-T. Song, S. Kim, E.-J. Cho, H.-G. Yoon, J.-S. Suh, J. Cheon, Nat. Med. 13 (1) (2007) 95–99.
[114] A. Pardo, B. Pelaz, J. Gallo, M. Bañobre-López, W.J. Parak, S. Barbosa, P. del Pino, P. Taboada, Chem. Mater. 32 (6) (2020) 2220–2231.
[115] X. Lasheras, M. Insausti, J.M. de la Fuente, I. Gil de Muro, I. Castellanos-Rubio, L. Marcano, M.L. Fernández-Gubieda, A. Serrano, R. Martín-Rodríguez, E. Garaio, J.A. García, L. Lezama, Dalton Trans. 48 (30) (2019) 11480–11491.
[116] S. Dutta, S. Parida, C. Maiti, R. Banerjee, M. Mandal, D. Dhara, J. Colloid Interface Sci. 467 (2016) 70–80.
[117] L. Chen, F.S. Razavi, A. Mumin, X. Guo, T.-K. Sham, J. Zhang, RSC Adv. 3 (7) (2013) 2390–2397.
[118] A. Louie, Chem. Rev. 110 (5) (2010) 3146–3195.
[119] S.O. Aisida, P.A. Akpa, I. Ahmad, T.-K. Zhao, M. Maaza, F.I. Ezema, Eur. Polym. J. 122 (2020) 109371.
[120] M.K. Lima-Tenório, E.A. Gómez Pineda, N.M. Ahmad, H. Fessi, A. Elaissari, Int. J. Pharm. 493 (1) (2015) 313–327.
[121] H. Cho, D. Alcantara, H. Yuan, R.A. Sheth, H.H. Chen, P. Huang, S.B. Andersson, D.E. Sosnovik, U. Mahmood, L. Josephson, ACS Nano 7 (3) (2013) 2032–2041.
[122] T.-H. Chung, C.-C. Hsieh, J.-K. Hsiao, S.-C. Hsu, M. Yao, D.-M. Huang, RSC Adv. 6 (51) (2016) 45553–45561.
[123] P.C. Naha, A.A. Zaki, E. Hecht, M. Chorny, P. Chhour, E. Blankemeyer, D.M. Yates, W.R. Witschey, H.I. Litt, A. Tsourkas, D.P. Cormode, J. Mater. Chem. B 2 (46) (2014) 8239–8248.
[124] Y. Sun, Z.L. Chen, X.X. Yang, P. Huang, X.P. Zhou, X.X. Du, Nanotechnology 20 (13) (2009) 135102.
[125] D. Zhang, X. Zuo, P. Wang, W. Gao, L. Pan, Applied Nanoscience (Switzerland) 11 (1) (2021) 21–27.
[126] M. Barrow, A. Taylor, P. Murray, M.J. Rosseinsky, D.J. Adams, Chem. Soc. Rev. 44 (19) (2015) 6733–6748.
[127] H. Tian, Z. Tang, X. Zhuang, X. Chen, X. Jing, Prog. Polym. Sci. 37 (2) (2012) 237–280.
[128] C. Tassa, S.Y. Shaw, R. Weissleder, Acc. Chem. Res. 44 (10) (2011) 842–852.
[129] W.B. Mdlalose, S.R. Mokhosi, S. Dlamini, T. Moyo, M. Singh, AIP Adv. 8 (5) (2018) 056726.
[130] O. Yunok, N. Lee, H.W. Kang, J. Oh, Nanotechnology 27 (2016) 115101.
[131] A. Seyfoori, S. Sarfarazijami, S.A. Seyyed Ebrahimi, Artif. Cells Nanomed. Biotechnol. 47 (1) (2019) 1437–1443.
[132] B. Bateer, C. Tian, Y. Qu, S. Du, Y. Yang, Z. Ren, K. Pan, H. Fu, Dalton Trans. 43 (26) (2014) 9885–9891.
[133] S.A. Shah, A. Majeed, K. Rashid, S.-U. Awan, Mater. Chem. Phys. 138 (2) (2013) 703–708.
[134] B. Ding, S. Shao, H. Xiao, C. Sun, X. Cai, F. Jiang, X. Zhao, P. a., Ma and J. Lin, Nanoscale 11 (31) (2019) 14654–14667.
[135] U.I. Tromsdorf, N.C. Bigall, M.G. Kaul, O.T. Bruns, M.S. Nikolic, B. Mollwitz, R.A. Sperling, R. Reimer, H. Hohenberg, W.J. Parak, S. Förster, U. Beisiegel, G. Adam, H. Weller, Nano Lett. 7 (8) (2007) 2422–2427.
[136] K. Kaaki, K. Hervé-Aubert, M. Chiper, A. Shkilnyy, M. Soucé, R. Benoit, A. Paillard, P. Dubois, M.-L. Saboungi, I. Chourpa, Langmuir 28 (2) (2012) 1496–1505.
[137] G. Wang, D. Zhao, Y. Ma, Z. Zhang, H. Che, J. Mu, X. Zhang, Z. Zhang, Appl. Surf. Sci. 428 (2018) 258–263.
[138] T.R. Bastami, M.H. Entezari, Q.H. Hu, S.B. Hartono, S.Z. Qiao, Chem. Eng. J. 210 (2012) 157–165.
[139] W. Wang, Z. Ding, M. Cai, H. Jian, Z. Zeng, F. Li, J.P. Liu, Appl. Surf. Sci. 346 (2015).
[140] M.A. González-Gómez, S. Belderbos, S. Yañez-Vilar, Y. Piñeiro, F. Cleeren, G. Bormans, C.M. Deroose, W. Gsell, U. Himmelreich, J. Rivas, Nanomaterials (Basel) 9 (11) (2019) 1626.
[141] S. Shafiu, R. Topkaya, A. Baykal, M. Toprak, Mater. Res. Bull. 48 (2013) 4066–4071.
[142] F. Danhier, E. Ansorena, J.M. Silva, R. Coco, A. Le Breton, V. Préat, Journal of controlled release : official journal of the Controlled Release Society 161 (2) (2012) 505–522.
[143] P.W. Sylvester, Methods in molecular biology (Clifton, N.J.) 716 (2011) 157–168.
[144] S. Rampersad, Sensors (Basel, Switzerland) 12, 12347-12360 (2012).
[145] U.S. Patil, S. Adireddy, A. Jaiswal, S. Mandava, B.R. Lee, D.B. Chrisey, Int. J. Mol. Sci. 16 (10) (2015) 24417–24450.
[146] C. Iacovita, A. Florea, L. Scorus, E. Pall, R. Dudric, A.I. Moldovan, R. Stiufiuc, R. Tetean, C.M. Lucaciu, Nanomaterials 9 (10) (2019) 1489.
[147] K. Islam, M. Haque, A. Kumar, A. Hoq, F. Hyder, S.M. Hoque, Nanomaterials 10 (11) (2020) 2297.
[148] L. Zhang, S. Xiao, X. Kang, T. Sun, C. Zhou, Z. Xu, M. Du, Y. Zhang, G. Wang, Y. Liu, D. Zhang, M. Gong, Int J Nanomedicine 16 (2021) 1709–1724.
[149] C.R. Kalaiselvan, N.D. Thorat, N.K. Sahu, ACS Omega 6 (8) (2021) 5266–5275.
[150] Z. Li, S.X. Wang, Q. Sun, H.L. Zhao, H. Lei, M.B. Lan, Z.X. Cheng, X.L. Wang, S.X. Dou, G.Q. Max Lu, Adv Healthc Mater 2 (7) (2013) 958–964.
[151] C.M. Siamof, S. Goel, W. Cai, Front. Chem. 8 (2020).
[152] L. Cui, J. Rao, Wiley interdisciplinary reviews, Nanomedicine and nanobiotechnology 9 (2) (2017).
[153] A. Roch, R.N. Muller, P. Gillis, J. Chem. Phys. 110 (11) (1999) 5403–5411.
[154] V. Sreeja, K.N. Jayaprabha, P.A. Joy, Applied Nanoscience (Switzerland) 5 (4) (2015) 435–441.
[155] Z. Zhou, L. Yang, J. Gao, X. Chen, Adv. Mater. 31 (8) (2019) 1804567.
[156] H. Zhang, L. Li, X.L. Liu, J. Jiao, C.T. Ng, J.B. Yi, Y.E. Luo, B.H. Bay, L.Y. Zhao, M.L. Peng, N. Gu, H.M. Fan, ACS Nano 11 (4) (2017) 3614–3631.
[157] S. Xiao, X. Yu, L. Zhang, Y. Zhang, W. Fan, T. Sun, C. Zhou, Y. Liu, Y. Liu, M. Gong, D. Zhang, Int J Nanomedicine 14 (2019) 8499–8507.
[158] E. Mazarío, J. Sánchez-Marcos, N. Menéndez, M. Cañete, A. Mayoral, S. Rivera-Fernández, J.M. de la Fuente, P. Herrasti, The Journal of Physical Chemistry C 119 (12) (2015) 6828–6834.
[159] Z. He, H. Yan, W. Zeng, K. Yang, P. Rong, J. Mater. Chem. B 9 (6) (2021) 1625–1637.
[160] D. García-Soriano, R. Amaro, N. Lafuente-Gómez, P. Milán-Rois, Á. Somoza, C. Navío, F. Herranz, L. Gutiérrez, G. Salas, J. Colloid Interface Sci. 578 (2020) 510–521.
[161] M. Zhang, Y. Cao, L. Wang, Y. Ma, X. Tu, Z. Zhang, ACS Appl. Mater. Interfaces 7 (8) (2015) 4650–4658.
[162] M. Ravichandran, V. s,, Materials Research Express 7 (2019).
[163] X. Zhou, X. Lv, W. Zhao, T. Zhou, S. Zhang, Z. Shi, S. Ye, L. Ren, Z. Chen, RSC Adv. 8 (33) (2018) 18647–18655.
[164] A. Ereath Beeran, S.S. Nazeer, F.B. Fernandez, K.S. Muvvala, W. Wunderlich, S. Anil, S. Vellappally, M.S. Ramachandra Rao, A. John, R.S. Jayasree, P.R. Harikrishna Varma, PCCP 17 (6) (2015) 4609–4619.
[165] X.L. Liu, Y.T. Wang, C.T. Ng, R. Wang, G.Y. Jing, J.B. Yi, J. Yang, B.H. Bay, L.-Y.-L. Yung, D.D. Fan, J. Ding, H.M. Fan, Adv. Mater. Interfaces 1 (2) (2014) 1300069.

[166] Z. Wang, J. Liu, T. Li, J. Liu, B. Wang, J. Mater. Chem. B 2 (29) (2014) 4748–4753.
[167] N. Venkatesha, S.M. Pudakalakatti, Y. Qurishi, H.S. Atreya, C. Srivastava, RSC Adv. 5 (118) (2015) 97807–97815.
[168] M. Apel, U. Heinlein, S. Miltenyi, J. Schmitz and J. Campbell (2007) 571–595.
[169] N. Tran, T.J. Webster, J. Mater. Chem. 20 (40) (2010) 8760–8767.
[170] M. Bañobre-López, A. Teijeiro, J. Rivas, Rep Pract Oncol Radiother 18 (6) (2013) 397–400.
[171] A.E. Deatsch, B.A. Evans, J. Magn. Magn. Mater. 354 (2014) 163–172.
[172] R.R. Shah, T.P. Davis, A.L. Glover, D.E. Nikles, C.S. Brazel, J. Magn. Magn. Mater. 387 (2015) 96–106.
[173] D. Psimadas, G. Baldi, C. Ravagli, M. Comes Franchini, E. Locatelli, C. Innocenti, C. Sangregorio, G. Loudos, Nanotechnology 25 (2) (2014) 025101.
[174] N. Telling, in: Nanomaterials for Magnetic and Optical Hyperthermia Applications, 2019, pp. 173–197.
[175] W.F. Brown, Phys. Rev. 130 (5) (1963) 1677–1686.
[176] M.M. Cruz, L.P. Ferreira, J. Ramos, S.G. Mendo, A.F. Alves, M. Godinho, M.D. Carvalho, J. Alloy. Compd. 703 (2017) 370–380.
[177] R.K. Chandunika, R. Vijayaraghavan, N.K. Sahu, Mater. Res. Express 7 (6) (2020) 064002.
[178] A. Doaga, A.M. Cojocariu, W. Amin, F. Heib, P. Bender, R. Hempelmann, O.F. Caltun, Mater. Chem. Phys. 143 (1) (2013) 305–310.
[179] P. Pradhan, J. Giri, G. Samanta, H.D. Sarma, K.P. Mishra, J. Bellare, R. Banerjee, D. Bahadur, Journal of Biomedical Materials Research Part B: Applied, Biomaterials 81B (1) (2007) 12–22.
[180] T.T.N. Nha, P.H. Nam, N.X. Phuc, V.Q. Nguyen, N.H. Nam, D.H. Manh, L.T. Tam, N.T.N. Linh, B.T.V. Khanh, L.T. Lu, L.H. Nguyen, P.T. Phong, RSC Adv. 11 (48) (2021) 30054–30068.
[181] A. Salokhe, A. Koli, V. Jadhav, S. Mane-Gavade, A. Supale, R. Dhabbe, X.-Y. Yu, S. Sabale, SN Applied Sciences 2 (12) (2020) 2017.
[182] P. Pradhan, J. Giri, R. Banerjee, J. Bellare, D. Bahadur, J. Magn. Magn. Mater. 311 (1) (2007) 208–215.
[183] D.K. Mondal, S. Jonak, N. Paul, J.P. Borah, RSC Adv. 11 (21) (2021) 12507–12519.
[184] J. Giri, P. Pradhan, T. Sriharsha, D. Bahadur, J. Appl. Phys. 97 (10) (2005) 10Q916.
[185] Ç.E. Demirci Dönmez, P.K. Manna, R. Nickel, S. Aktürk, J. van Lierop, ACS Appl. Mater. Interfaces 11 (7) (2019) 6858–6866.
[186] J.-H. Lee, J.-T. Jang, J.-S. Choi, S.H. Moon, S.-H. Noh, J.-W. Kim, J.-G. Kim, I.-S. Kim, K.I. Park, J. Cheon, Nat. Nanotechnol. 6 (7) (2011) 418–422.
[187] M. Angelakeris, Z.-A. Li, M. Hilgendorff, K. Simeonidis, D. Sakellari, M. Filippousi, H. Tian, G. Van Tendeloo, M. Spasova, M. Acet, M. Farle, J. Magn. Magn. Mater. 381 (2015) 179–187.
[188] A. Makridis, K. Topouridou, M. Tziomaki, D. Sakellari, K. Simeonidis, M. Angelakeris, M.P. Yavropoulou, J.G. Yovos, O. Kalogirou, J. Mater. Chem. B 2 (47) (2014) 8390–8398.
[189] A.-T. Le, C. Giang, L. Tam, T. Ta, V. Phan, J. Alonso Masa, J. Devkota, E. Garaio, J. García, R. Martín-Rodríguez, M.L. Fdez-Gubieda, H. Srikanth, M.-H. Phan, Nanotechnology 27 (2016) 155707.
[190] R. Otero-Lorenzo, E. Fantechi, C. Sangregorio, V. Salgueiriño, Chemistry – A„ European Journal 22 (19) (2016) 6666–6675.
[191] P. Seal, M. Hazarika, N. Paul, J.P. Borah, AIP Conf. Proc. 1942 (1) (2018) 050083.
[192] S.G. Mendo, A.F. Alves, L.P. Ferreira, M.M. Cruz, M.H. Mendonça, M. Godinho, M.D. Carvalho, New J. Chem. 39 (9) (2015) 7182–7193.
[193] M.W. Freeman, A. Arrott, J.H.L. Watson, J. Appl. Phys. 31 (5) (1960) S404–S405.
[194] K.J. Widder, A.E. Senyei, D.G. Scarpelli, Proceedings of the Society for Experimental Biology and Medicine 158 2 (1978) 141–146.
[195] Y. Morimoto, K. Sugibayashi, M. Okumura, Y. Kato, J. Pharmacobiodyn. 3 (5) (1980) 264–267.
[196] K.J. Widder, R.M. Morris, G. Poore, D.P. Howard, A.E. Senyei, Proc. Natl. Acad. Sci. 78 (1) (1981) 579–581.
[197] P.K. Gupta, C.-T. Hung, N.S. Rao, J. Pharm. Sci. 78 (4) (1989) 290–294.
[198] A.S. Lübbe, C. Bergemann, W. Huhnt, T. Fricke, H. Riess, J.W. Brock, D. Huhn, Cancer Res. 56 (20) (1996) 4694–4701.
[199] C.J. Sunderland, M. Steiert, J.E. Talmadge, A.M. Derfus, S.E. Barry, Drug Dev. Res. 67 (1) (2006) 70–93.
[200] M.R. Farani, P. Khadiv-Parsi, G.H. Riazi, M.S. Ardestani, H.S. Rad, Applied Nanoscience (Switzerland) 10 (5) (2020) 1707.
[201] O. Veiseh, J.W. Gunn, M. Zhang, Adv. Drug Deliv. Rev. 62 (3) (2010) 284–304.
[202] Y. Ding, S.Z. Shen, H. Sun, K. Sun, F. Liu, Y. Qi, J. Yan, Mater. Sci. Eng., C 48 (2015) 487–498.
[203] R. M, V. S, J. T. Ramirez, V. A and L. L„ Artif. Cells Nanomed. Biotechnol. 46 (sup3) (2018) S993–S1003.
[204] V. Taresco, I. Francolini, F. Padella, M. Bellusci, A. Boni, C. Innocenti, A. Martinelli, L. D'Ilario, A. Piozzi, Mater. Sci. Eng., C 52 (2015) 72–81.
[205] H. Safdar, H. Hasan, M. Anees, Z. Hussain, Int. J. Pharm. Pharm. Sci. 9 (2017).
[206] S.A. Shah, M.H. Asdi, M.U. Hashmi, M.F. Umar, S.-U. Awan, Mater. Chem. Phys. 137 (1) (2012) 365–371.
[207] B. Sahoo, K.S.P. Devi, S. Dutta, T.K. Maiti, P. Pramanik, D. Dhara, J. Colloid Interface Sci. 431 (2014) 31–41.
[208] Y. Yang, H. Shi, Y. Wang, B. Shi, L. Guo, D. Wu, S. Yang, H. Wu, J. Biomater. Appl. 30 (6) (2016) 810–822.
[209] Z. Karimi, S. Abbasi, H. Shokrollahi, G. Yousefi, M. Fahham, L. Karimi, O. Firuzi, Mater. Sci. Eng., C 71 (2017) 504–511.
[210] N. Rozanova, J.Z. Zhang, D.E. Heck, Cancer Lett. 252 (2) (2007) 216–224.
[211] S.I. Dikalov, M.P. Vitek, R.P. Mason, Free Radical Biol. Med. 36 (3) (2004) 340–347.
[212] A.S. Azmi, S.H. Bhat, S.M. Hadi, FEBS Lett. 579 (14) (2005) 3131–3135.
[213] H. R. Podmore Id Fau - Griffiths, K. E. Griffiths Hr Fau - Herbert, N. Herbert Ke Fau - Mistry, P. Mistry N Fau - Mistry, J. Mistry P Fau - Lunec and J. Lunec, Nature 392 (6676) (1998).
[214] P.T. Schumacker, Cancer Cell 10 (3) (2006) 6.
[215] S.M. Hadi, M.F. Ullah, U. Shamim, S.H. Bhatt, A.S. Azmi, Chemotherapy 56 (4) (2010) 280–284.
[216] H. Kimoto E Fau - Tanaka, J. Tanaka H Fau - Gyotoku, F. Gyotoku J Fau - Morishige, L. Morishige F Fau - Pauling and L. Pauling, Cancer research 43 (2), 4 (1983).
[217] L. Gao, J. Zhuang, L. Nie, J. Zhang, Y. Zhang, N. Gu, T. Wang, J. Feng, D. Yang, S. Perrett, X. Yan, Nat. Nanotechnol. 2 (9) (2007) 577–583.
[218] T. Mai, J.Z. Hilt, J. Nanopart. Res. 19 (7) (2017) 253.
[219] J. Kim, H.R. Cho, H. Jeon, D. Kim, C. Song, N. Lee, S.H. Choi, T. Hyeon, J. Am. Chem. Soc. 139 (32) (2017) 10992–10995.
[220] S.-Y. Yin, G. Song, Y. Yang, Y. Zhao, P. Wang, L.-M. Zhu, X. Yin, X.-B. Zhang, Adv. Funct. Mater. 29 (25) (2019) 1901417.
[221] J. Kim, H.Y. Kim, S.Y. Song, S.-H. Go, H.S. Sohn, S. Baik, M. Soh, K. Kim, D. Kim, H.-C. Kim, N. Lee, B.-S. Kim, T. Hyeon, ACS Nano 13 (3) (2019) 3206–3217.
[222] C. Sapet, C. Pellegrino, N. Laurent, F. Sicard, O. Zelphati, Pharm. Res. 29 (5) (2012) 1203–1218.
[223] J. Huang, Y. Li, A. Orza, Q. Lu, P. Guo, L. Wang, L. Yang, H. Mao, Adv. Funct. Mater. 26 (22) (2016) 3818–3836.
[224] S.M. Dadfar, K. Roemhild, N.I. Drude, S. von Stillfried, R. Knüchel, F. Kiessling, T. Lammers, Adv. Drug Deliv. Rev. 138 (2019) 302–325.
[225] T. Carter, P. Mulholland, K. Chester, Immunotherapy 8 (8) (2016) 941–958.
[226] J.S. Aaron, J. Oh, T.A. Larson, S. Kumar, T.E. Milner, K.V. Sokolov, Opt. Express 14 (26) (2006) 12930–12943.
[227] D. Zhi, T. Yang, J. Yang, S. Fu, S. Zhang, Acta Biomater. 102 (2020) 13–34.
[228] T.-J. Yoon, H. Lee, H. Shao, R. Weissleder, Angew. Chem. Int. Ed. 50 (20) (2011) 4663–4666.
[229] D. Shweiki, A. Itin, D. Soffer, E. Keshet, Nature 359 (6398) (1992) 843–845.
[230] K. Zhang, M. Liu, X. Tong, N. Sun, L. Zhou, Y. Cao, J. Wang, H. Zhang, R. Pei, Biomacromolecules 16 (9) (2015) 2618–2623.
[231] D. Kim, Y.Y. Jeong, S. Jon, ACS Nano 4 (7) (2010) 3689–3696.
[232] W. Wang, M. Xi, X. Duan, Y. Wang, F. Kong, Int J Nanomedicine 10 (2015) 3737–3750.
[233] R. van der Meel, L.J.C. Vehmeijer, R.J. Kok, G. Storm, E.V.B. van Gaal, Adv. Drug Deliv. Rev. 65 (10) (2013) 1284–1298.
[234] Z.M. Qian, H. Li, H. Sun, K. Ho, Pharmacol. Rev. 54 (4) (2002) 561–587.
[235] T. Ichikawa, D. Högemann, Y. Saeki, E. Tyminski, K. Terada, R. Weissleder, E.A. Chiocca, J.P. Basilion, Neoplasia 4 (6) (2002) 523–530.
[236] G.O. Latunde-Dada, Biochim. Biophys. Acta, Gen. Subj. 1861 (8) (2017) 1893–1900.
[237] R. Weissleder, M. Nahrendorf, M.J. Pittet, Nat. Mater. 13 (2) (2014) 125–138.
[238] J. Xie, C. Yan, Y. Yan, L. Chen, L. Song, F. Zang, Y. An, G. Teng, N. Gu, Y. Zhang, Nanoscale 8 (38) (2016) 16902–16915.
[239] J. Xie, Y. Zhang, C. Yan, L. Song, S. Wen, F. Zang, G. Chen, Q. Ding, C. Yan, N. Gu, Biomaterials 35 (33) (2014) 9126–9136.
[240] R. Sun, Y. Ge, H. Liu, P. He, W. Song, X. Zhang, ACS Applied Bio Materials 4 (1) (2021) 701–710.
[241] V. Nica, C. Caro, J.M. Páez-Muñoz, M.P. Leal, M.L. Garcia-Martin, Nanomaterials 10 (5) (2020) 907.
[242] A.C. Anselmo, S. Mitragotri, Bioeng. Transl. Med. 1 (1) (2016) 10–29.
[243] D.-A.-O. Mundekkad, W.-A.-O. Cho, Int. J. Mol. Sci. 23 (3) (2022) 1685.
[244] V. Agrahari, V. Agrahari, Drug Discovery Today 23 (5) (2018) 974–991.
[245] H. He, L. Liu, E.E. Morin, M. Liu, A.-A.-O. Schwendeman, Acc. Chem. Res. 52 (9) (2019) 2445–2461.
[246] S. Gavas, S. Quazi, T.M. Karpiński, Nanoscale Res. Lett. 16 (1) (2021) 173.
[247] S.S. Laha, E. Abdelhamid, M.P. Arachchige, A. Kumar, A. Dixit, J. Am. Ceram. Soc. 100 (4) (2017) 1534–1541.
[248] K. Nadeem, H. Krenn, T. Traussing, I. Letofsky-Papst, J. Appl. Phys. 109 (1) (2011) 013912.
[249] B. Aslibeiki, P. Kameli, H. Salamati, M. Eshraghi, T. Tahmasebi, J. Magn. Magn. Mater. 322 (19) (2010) 2929–2934.
[250] B. Pimentel, R. Caraballo-Vivas, N. Checca, V. Zverev, R. Salakhova, L. Makarova, A. Pyatakov, N. Perov, A. Tishin, A. Shtil, J. Solid State Chem. 260 (2018) 34–38.
[251] C.J. Bae, S. Angappane, J.-G. Park, Y. Lee, J. Lee, K. An, T. Hyeon, Appl. Phys. Lett. 91 (10) (2007) 102502.
[252] S. Laha, R. Mukherjee, G. Lawes, Mater. Res. Express 1 (2) (2014) 025032.
[253] A. Anupama, V. Kumaran, B. Sahoo, New J. Chem. 43 (25) (2019) 9969–9979.
[254] A. Singh, S. Pathak, P. Kumar, P. Sharma, A. Rathi, G. Basheed, K. Maurya, R.P. Pant, J. Magn. Magn. Mater. 493 (2020) 165737.
[255] F. G. d. Silva, J. Depeyrot, Y. L. Raikher, V. Stepanov, I. Poperechny, R. Aquino, G. Ballon, J. Geshev, E. Dubois and R. Perzynski„ Sci. Rep. 11 (1) (2021) 1–10.
[256] E. Abdelhamid, S.S. Laha, A. Dixit, G.A. Nazri, O.D. Jayakumar, B. Nadgorny, J. Electron. Mater. 48 (2019) 5.

[257] R. Mohan, M.P. Ghosh, S. Mukherjee, J. Magn. Magn. Mater. 458 (2018) 193–199.
[258] Y.P. Desai, S. Jamwal, S. Modiyil, S. Chodankar, R. Sathe and M. M. Kothawale 2265 (1) (2020) 030511.
[259] S.S. Laha, N.D. Thorat, G. Singh, C. Sathish, J. Yi, A. Dixit, A. Vinu, Small 18 (11) (2022) 2104855.
[260] N.D. Thorat, R.A. Bohara, H.M. Yadav, S.A. Tofail, RSC Adv. 6 (97) (2016) 94967–94975.
[261] N. D. Thorat, R. A. Bohara, S. A. Tofail, Z. A. Alothman, M. J. Shiddiky, M. S. A Hossain, Y. Yamauchi and K. C. W. Wu*, European Journal of Inorganic Chemistry 2016 (28), 4586-4597 (2016).
[262] X.L. Liu, Y.T. Wang, C.T. Ng, R. Wang, G.Y. Jing, J.B. Yi, J. Yang, B.H. Bay, L.Y.L. Yung, D.D. Fan, Adv. Mater. Interfaces 1 (2) (2014) 1300069.
[263] B.P. Kumar, N. Puvvada, S. Rajput, S. Sarkar, S.K. Das, L. Emdad, D. Sarkar, P. Venkatesan, I. Pal, G. Dey, J. Mater. Chem. B 3 (1) (2015) 90–101.